Multifunctional Gadolinium bearing Iron Oxide-Gold Nanoparticles for theranostic application

Vital Cruvinel Ferreira Filho

Thesis to obtain the Master of Science Degree in

Materials Engineering

Supervisor: Dra. Laura Cristina de Jesus Pereira Waerenborgh

Co – Supervisor: Dr. Luiz Carlos Casteletti

Examination Committee

Chairperson: Dr. José Paulo Farinha

Supervisor: Dra. Laura Cristina de Jesus Pereira Waerenborgh

Members of Committee: Dra. Maria João Pedroso Carmezim

December 2022

I declare that this document is an original work of my own authorship and that it fulfils all the requirements of the Code of Conduct and Good Practices of the *Universidade de Lisboa*.

To my parents, family, friends, teachers, and all those who support me in my journey.

Acknowledgements

To Escola de Engenharia de São Carlos from Universidade de São Paulo and C^2TN/Instituto Superior Técnico from Universidade de Lisboa where I had the opportunity to be in a Double-Degree program, learn, grow and enrich myself during my academic life.

I would like to thank my supervisor, Prof. Laura Pereira Waerenborgh who accepted me to be her master's student and who during this work has always been with the major patient, dedicated to me, always been by my side in good and difficult moments, for her teachings and for her empathy. Her guidance inspires me to be a better researcher.

I would like to thank Prof. Maria Paula Cabral Campello who took my hand and led me to the chemistry laboratories, who was by my side most of the time during this master's program. Despite the amount of work within her hands, she always had a time to support me and teach me with the patience and commitment, who gave me hearty laughs and made me more relaxed. She also introduced me to the cats on the campus, which I am very grateful for this. I can certainly say that she was crucial for the success of this work. I would always have to thank her and Prof. Laura for all the incredible technical and human support that they gave me all the time.

I am also very grateful to Prof. João Carlos Waerenborgh and Dr. Bruno Vieira who performed the Mössbauer spectroscopy measurements, Doctor Fernanda Marques for helping me with the cytotoxicity assays and my co-supervisor Prof. Luiz Casteletti for the support and for accepting to be part of this work.

I also would like to acknowledge Dra. Maria João Carmezin for the help with the C01 SPIONs synthesis and for welcoming me so well, Mr. Luís Belot for the powder X-ray diffraction measurements, Dr. Eugénio Soares, from Laboratório Central de Análises (LCA) of University of Aveiro for the ICP-MS analysis, Dr. Erin Tranfield and Ms. Beatriz Tomaz, from Instituto Gulbenkian de Ciência (IGC) for the high-resolution TEM analysis, and Doctor Paula Soares, from CENIMAT/I3N, FCT/UNL, for the hyperthermia assays.

I would like to thank immensely my friends and cousins who gave me support and made me smile in this journey: Raphael Novelli, Matheus Kalil, Paola Cristina Barbosa, Lorenzo Andreotti, José Ney Ghelfi, Pedro Mendes, Leonardo Camargo de Santi, Lucca Bonetti, Gonçalo Damas, Daniel Barcelos, Vinicius Cruvinel Ferreira Vieira e João Pedro Cruvinel Ferreira.

These two years would not have been possible without the unconditional support from a person who has always been by my side, my “Valentine”, Ana Helena Vidal. I would like to thank you for the love, all the good times we had, good laughs, trips, your inexhaustible patience, for believing in me, encouraging my growth, for so many moments that in the midst of despair and agony, I found in your voice comfort and a safe place to cry. For understanding my weaknesses and accepting my faults.

At last, but not least, the major thanks to my parents, Vital Cruvinel Ferreira and Adriana Carla da Silva Ferreira, for making me who I am, for the opportunities and for all the care, support, and love. To my grandparents Antonio Custódio Ferreira e Maria Cecília Cruvinel Ferreira. To my aunts that was the base in my childhood “Tia Arlete”, “Tia Bebete” e “Dida” (*in memorian*).

Abstract

Superparamagnetic iron oxide nanoparticles (SPIONs) have been progressively studied due to their excellent magnetic behavior, favoring their application in medicine, both in diagnosis and therapy. For example, in the diagnosis and follow up of cancer diseases by magnetic resonance imaging and in their therapy by hyperthermia. Moreover, coating these nanoparticles with an organic material, with long-chain surfactants, or by an inorganic material, such as gold, can improve their stability and make them more versatile.

The present work aimed to explore a new and original approach in the systematic preparation of multifunctional magnetic nanoparticles, based on SPIONs cores, coated with a polymer, dextran, and gold nanoparticles functionalized with a chelating agent, TDOTA, for the complexation of Gd^{3+} to enhance theranostic applications. In order to optimize the method for obtaining these nanomaterials, three synthesis routes for the SPIONs were designed: the first (method A) by co-precipitation with iron reduction using sodium sulfite ($NaSO_3$); the second (method B) by regular co-precipitation using iron ions (II and III), followed by hydrothermal treatment. A third synthesis method (method C) was also used, although according to this only the naked SPIONs were obtained, without any coating. In this method, co-precipitation with different ratios of iron ions (II and III) was used, compared to method B. Additionally, precipitation step was controlled at pH 9.6.

The nanoparticle samples obtained by the 3 methods and the samples with the subsequent coating were characterized structurally and morphologically by powder X-ray diffraction (PXRD), Mössbauer spectroscopy, transmission electron microscopy (TEM), zeta potential (ζ), dynamic light scattering (DLS), and inductively coupled plasma – mass spectrometry (ICP-MS). Their magnetic behavior was also studied using a magnetometer (SQUID), revealing the presence of superparamagnetic behavior in all of them, essential for further studies.

Viability tests of the samples obtained according to methods A and B were performed on prostate cancer cells (PC3) in order to have insight into their biomedical viability. These preliminary studies revealed that in-vitro studies on PC3 cells can be performed with dilutions of these nanoparticles containing up to 50 µg/mL of iron.

At the end of this work it was concluded that the synthesized nanoparticles provide morphological and magnetic qualities that could be used in *in vitro* and *in vivo* tests for future MRI and magnetic hyperthermia assays in a cell line.

Keywords: SPIONs, Magnetic nanoparticles, Multifunctional nanoplatforms, Gold plating, Gadolinium functionalization, Cancer theranostics, Hyperthermia, Magnetic resonance imaging.

Resumo

As nanopartículas de óxido de ferro superparamagnéticas (SPIONs) têm vindo a ser estudadas progressivamente devido ao seu excelente comportamento magnético, favorecendo, a sua aplicação em medicina, tanto no diagnóstico como na terapêutica. Por exemplo, no diagnóstico de doenças cancerígenas, por ressonância magnética, e na sua terapia por hipertermia. Além disso, o revestimento destas nanopartículas com um material orgânico, seja com surfactantes de cadeia longa, ou por um material inorgânico, como o ouro, pode melhorar a sua estabilidade e torná-las mais versáteis.

O presente trabalho visou explorar uma nova e original bordagem na preparação sistemática de nanopartículas magnéticas multifuncionais, baseadas em núcleos de SPIONs revestidos com um polímero, dextrano, e nanopartículas de ouro funcionalizado com um agente quelante, TDOTA, para a complexação do Gd^{3+} para potenciar aplicações teranósticas. De modo a optimizar o método de obtenção destes nanomateriais foram desenhadas três vias de síntese dos SPIONs: a primeira (método A) por co-precipitação com redução do ferro através do sulfito de sódio ($NaSO_3$); a segunda (método B) por co-precipitação regular, utilizando-se iões de ferro (II e III), seguido de um tratamento hidrotermal. Foi ainda utilizado um terceiro método de síntese (método C) baseado na co-precipitação com diferentes proporções de iões de ferro (II e III) em relação ao método B, com controlo do pH, para o valor ótimo pH= 9.6. Segundo este método obtiveram-se apenas os SPIONs sem qualquer revestimento.

As amostras das nanopartículas obtidas pelos 3 métodos e as amostras com os revestimentos subsequentes foram caracterizadas estrutural e morfologicamente por difracção de raios X em pó (PXRD), espectroscopia de Mössbauer, microscopia electrónica de transmissão (TEM), potencial zeta (ζ), dispersão dinâmica da luz (DLS) e espectroscopia de massa com plasma indutivamente acoplado (ICP-MS). O seu comportamento magnético foi também estudado através de um magnetómetro (SQUID). tendo revelado a presença em todas elas das características superparamagnéticas, essenciais para o prosseguimento dos estudos.

Com vista a estimar as possíveis aplicações biomédicas foram realizados testes de viabilidade das amostras obtidas segundo os métodos A e B em células cancerígenas da próstata (PC3). Estes estudos preliminares revelaram que os estudos in-vitro em células PC3 podem ser realizados em soluções destas nanopartículas diluídas num máximo de 50 µg/mL em ferro.

No final deste trabalho concluiu-se que as nanopartículas sintetizadas possuem qualidades morfológicas e magnéticas que poderão ser usadas em testes *in vitro* e *in vivo* para futuros ensaios de MRI e hipertermia magnética numa linha celular.

Palavras-chave: SPIONs, nanopartículas magnéticas, nanoplataformas multifuncionais, revestimento de ouro, funcionalização de gadolínio, teranóstica do cancro, hipertermia, Imagem por ressonância Magnética.

Table of Contents

List of Figures

List of Tables

List of Abbreviations and Symbols

AC - Alternated Current
B - Magnetic Flux Density
CA - Contrast Agents
D_c - Critical Diameter
D_H - Hydrodynamic Size
DLS - Dynamic Light Scattering
D_{MAG} - Magnetic Diameter
DMSO - Dimethyl sulfoxide
D_{TEM} - Particle Size
DTS - Dispersion Technology Software
Dx - Dextran
Dx - NH_2 - Amino Dextran
D_{XRD} - Crystallite Size
FBS - Fetal Bovine Serum
FC - Field Cooling
FCC - Face-Centered cubic
Fe_3O_4 - Magnetite
FWHM - Full Width at Half Maximum
GBCAs - Gadolinium (III) Based Contrast Agents
GRPR - Gastrin Releasing Peptide Receptor
H - Magnetic Field
H_c - Coercive Field
ICP-MS - Inductively Coupled Plasma – Mass Spectrometry
JCPDS- Joint Committee on Powder Diffraction Standards
K_b - Boltzmann Constant
LCA - Laboratório Central de Análises
M - Magnetization
MNPs - Magnetic Nanoparticles
M_r - Magnetic remanence
MRI - Magnetic Resonance Imaging
M_s - Saturation Magnetization
MTT - 3-(4,5-dimethylthiazol-2-yl)-2,5-diphenyl-2H-tetrazolium bromide
Na_2SO_3 - Sodium Sulphite
NPs - Nanoparticles
P_{atm} - Atmospheric Pressure
PBS - Phosphate-Buffered Saline
PC3 - Classical Prostate Cancer Cell Line

PDI - Polydispersity Index

PEG - Poly(ethylene glycol)

PVA - Polyvinyl Alcohol

PVP - Polyvinylpyrrolidone

RPM - Rotations Per Minute

RPMI - Roswell Park Memorial Institute Medium

RT - Room Temperature

SAR - Specific Absorption Rate

SPIONs - Superparamagnetic Iron Oxide Nanoparticles

SQUID - Superconducting Quantum Interference Device

T - Temperature

$\mathbf{T_1}$ - Transverse relaxation

$\mathbf{T_2}$ - Longitudinal relaxation

$\mathbf{T_b}$ - Blocking Temperature

TDOTA - 2-[4,7-bis(carboxymethyl)-10-[2-(3-sulfanylpropanoylamino)ethyl]-1,4,7,10-tetrazacyclododec1-yl]acetic acid

TEM - Transmission Electronic Microscopy

V - Volume

ZFC - Zero-Field Cooling

$\boldsymbol{\alpha}$ **-** $\mathbf{Fe_2O_3}$ - Hematite

$\boldsymbol{\alpha}$ **- FeO(OH)** – Goethite

ΔT - Temperature Variation

χ **-** Magnetic Susceptibility

γ **-** $\mathbf{Fe_2O_3}$ - Maghemite

λ - Wavelength

σ - Size Dispersion

τ_0 time period

τ_{N-} Néel relaxation time

ζ - Zeta Potential

Chapter 1

Introduction

1.1 Motivation

Cancer is a major life-threatening disease, and its incidence and mortality are growing rapidly worldwide and are the leading cause of death before the age of 70 in 112 countries. According to estimates, there were 19.3 million new cancer cases and about 10 million deaths in 2020 [1]. Current cancer treatment still relies heavily on surgical intervention, as traditional anti-cancer treatments such as chemotherapy, radiotherapy are not always efficient and often have several drawbacks related to toxicity and lack of specificity [2]. The application of a personalized therapy and the monitoring of its effectiveness usually depend on image-based diagnostics. In this context, there is currently a huge excitement about the prospects of developing specific theranostics drugs: compounds that simultaneously combine functions with potential for targeted therapy and imaging. Theranostics compounds are based on molecular or nanosized constructs. Due to their unique physical characteristics and ability to be functionalized at the cellular and molecular level [3], magnetic nanoparticles (MNPs) are an important class of nanostructured materials with potential cancer theranostic applications, such as hyperthermia treatment, and magnetic resonance imaging (MRI) of tumor cells. In addition, they have been proposed for use as a targeted drug delivery system because, since these magnetic nanoparticles are easily controlled by the application of an external magnetic field, it may allow the release of anticancer drugs at a specified rate and location [4, 5].

1.2 Topic Overview

Nanotechnology provides a flexible framework for the generation of effective therapeutic materials that can mix with a target and induce the desired response. Due to their intrinsic nanoscale features, nanoparticles have emerged as a valuable tool for a wide range of nanomedicine applications [6–8]. Iron oxide-based nanoparticles have emerged as a good possibility for cancer treatment among the nanomaterials examined. Due to their biocompatibility, these nanoparticles have gained a lot of attention. Most of their applications are come from their magnetic properties that differ greatly from those of bulk materials [9]. Figure 1 exhibits the Superparamagnetic Iron Oxide Nanoparticles (SPIONs) utilized in diverse biological applications.

Figure 1: Scheme showing some SPIONs applications. Adapted from [10].

SPIONs are nanoparticles formed by small iron oxide crystals (commonly magnetite Fe_3O_4 or maghemite $\gamma - Fe_2O_3$), whose core ranges from 10 nm to 100 nm in diameter [11]. Due to the small size, these oxides present superparamagnetic properties and consequently SPIONs are considered as a multipurpose class of medicinal agents. Among all their biomedical applications the most frequently explored for cancer therapy are hyperthermia, local chemotherapy and magnetically guided photodynamic, and in the field of diagnosis, the magnetic resonance imaging (MRI). Magnetic hyperthermia therapy consists in using an alternated magnetic field with a given frequency to induce a magnetic signal in the nanoparticles (NPs), which then release energy in the form of heat promoting temperature increase near cancerous tissues. To use this technique as an effective clinical treatment, it is mandatory to produce suitable magnetic nanoparticles that, besides releasing the necessary energy locally, should be non-toxic for the patients. Physiological instability, free radical generation, and inappropriate interface binding may limit the use of naked SPIONs in biomedicine. Therefore, for their use in the biomedical field, it is essential, to coat the NPs, since this may reduce their tendency to aggregate, and improve their colloidal stability and biocompatibility [12]. Additionally, coating allows the conjugation of inorganic components such as silica or gold that are also suitable candidates for the functionalization of the NPs, making them highly desirable for use in biomedical settings. The high versatility of gold-coated magnetic nanoparticles make them a good choice for many applications. The optical and magnetic properties of the particles can be tuned and tailored to the applications by changing their size, gold shell thickness, shape, charge, and surface modification by the attachment of various bioactive molecules such as peptides, antibodies, aptamers and (radio) metals

to further improve diagnosis and treatment efficiency. Nevertheless, depending on the gold shell thickness, charge, and surface modification, the gold coating can dramatically affect the magnetic properties of the final nanoparticles and consequently thus biomedical performance.

Nowadays, magnetic resonance imaging (MRI) is considered the main imaging modality. This technique provides anatomical and physiological images with high spatial resolution, although with relatively low sensitivity. For this reason, MRI examinations are performed with the help of contrast agents (CA) that significantly improve the contrast of images of selected tissues. CA are based on paramagnetic metal complexes, such Gd^{3+}, Mn^{2+}, Fe^{3+}, although about 40% of all MRI scans are performed with Gd^{3+}-based CA. (GBCAs). However, GBCAs have raised several toxicity concerns, including those associated with the release and accumulation of Gd^{3+} *in vivo*. The reference clinical dose for most applications when a Gd-based extracellular contrast agent is injected intravenously is 0.1 mmol/Kg body weight, but in specific applications, it may increase to values higher than 0.3 mmol/Kg body weight. Despite the high thermodynamic stability of injected GBCAs, the release of inorganic ionic Gd (III), which may precipitate in the bloodstream and other tissues [13] Since the 1990s, several iron oxides drugs have been approved as viable alternatives to clinical MRI GBCAs [14,15]. Such particles have several advantages, namely, biocompatibility, metabolizability, relatively high saturation magnetic moments, and easy surface functionalization. However, these contrast agents have not been commercially successful [15]. To our knowledge, NanoTherm® is the only clinically approved iron oxide nanoparticle drug for the treatment of glioblastoma by magnetic hyperthermia. In addition, to date, there are still no iron oxide-based nanoparticles for cancer theranostic or multimodal imaging. In fact, the unique and potentially ideal physicochemical characteristics associated with SPIONs, specifically their size and high surface area that is converted into high reactivity may also lead to high cytotoxicity *in vivo*. This cytotoxicity can be mitigated or nullified by for instance, tailoring their size and coating.

1.3 Thesis aim

This thesis aims to outline a novel and original strategy for the design and evaluation of multifunctional nanoparticles based on SPIONs covered with dextran polymer and gold coated, bearing Gd^{3+} complexes (Figure 2) that can potentially be suitable for diagnosis and therapeutic applications (theranostics). We aim to profit from the optical properties of Au and with the magnetic properties of Fe_3O_4 to obtain nanoplatforms that could potentially be suitable for diagnosis with dual-mode (T1/T2) MRI contrast agents and therapeutic applications (magnetic hyperthermia).

There are several methods and variations to synthesize SPIONs, including hydrothermal synthesis, co-precipitation, microemulsion, and thermal decomposition. In this work, the synthesis of SPIONs by using different approximation methods and their further coating and their subsequent characterization is

presented. This characterization included the use of different structural, chemical, and physical methods, such Powder X-Ray Diffraction (PXRD), Transmission Electronic Microscopy (TEM), Dynamic light Scattering (DLS), Zeta Potential, Inductively Coupled Plasma – Mass Spectrometry (ICP-MS), Mössbauer Spectroscopy, magnetization, and magnetic hyperthermia.

Furthermore, the *in vivo* cellular cytotoxic assays performed in Gastrin Releasing Peptide Receptor (GRPR) overexpressing prostate carcinoma cell lines (PC3) are also presented.

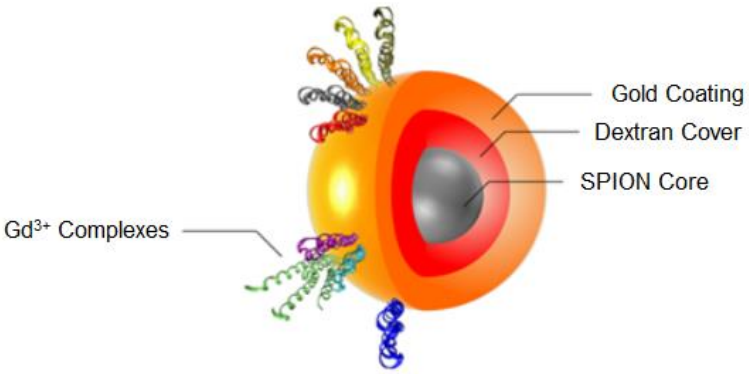

Figure 2: Scheme of the multifunctional nanoplatform designed for this work which consists in a SPION core, covered with dextran polymer, gold coated, and functionalized with Gd^{3+}.

1.4 Thesis outline

This thesis is organized in five chapters. In chapter 1, a summary of the main objective of the thesis is given. In chapter 2, the principles of magnetism and nanomagnetism are briefly reviewed. In single domain, superparamagnetism are the most promising dimension dependent effect and this will be also discussed. An overview of the suitability of SPIONS for biomedical applications is also given. Chapter 3 contains all the experimental sections including the preparation and characterization methods for both the syntheses of the SPIONs and the coatings and functionalization, as well as the procedures for the different characterization methods and the cytotoxicity tests in the prostate carcinoma cells (PC3). In chapter 4, the results of structural, morphological and magnetic data are presented putting into evidence the best results depending on the different synthetic methods, A, B or C, that conducted to the more stable and easily functionalized SPIONs. Finally, in chapter 5, the general conclusions are presented and the highlights about the future work is foreseen.

Chapter 2

Theoretical Aspects

2.1 Magnetic Properties

A magnetic field is a type of force field, similar to gravitational and electrical fields, conventionally represented by lines that create a contoured sphere and is defined by a source of potential. The density of these lines is known as the magnetic flux density (B). Under vacuum, the permeability of free space (μ_0) is related to the magnetic field (H) to B. As seen in equation below (1), a material exposed to a magnetic field can change the lines of force and consequently the flux density:

$$B = \mu_0(H + M) \quad (1)$$

The magnetization (M), of a given material is the measures of reaction of this material to an external magnetic field. M is the total magnetic moment of a given material, expressed as a fraction of its volume or mass. The direct relation of M and H defines the magnetic susceptibility (χ) as a quantitative measurement of such a response, and can be described as (2):

$$\chi = \frac{M}{H} \quad (2)$$

In general, the electrons that constitute a given system determine the magnetic susceptibility. The magnetic susceptibility can be considered, in a simple way, due to two different contributions: the first is diamagnetism, a quality that all materials have by nature and corresponds to a magnetic flux with the opposite sign of the applied magnetic field reducing the lines of force within the material. As a result, the diamagnetic susceptibility is negative and independent of temperature or field intensity. Typically, its contribution is much smaller than other magnetic contributions by several orders of magnitude.

The second contribution is due to the unpaired electrons present in the system and is known as paramagnetism. The magnetic moment results from the electrons' spinning and orbiting. Considering that these spins are not interacting and are randomly oriented, if an external magnetic field is applied the spins tend to align along the direction of the field. In this way, a paramagnet increases the magnetic flux by concentrating the lines of force. Because both diamagnetic and paramagnetic materials only exhibit magnetization in the presence of an external field, they are usually classified as nonmagnetic.

In real systems, the proximity of the atoms in the crystal lattice may induce interactions between the magnetic moments that depend on the temperature. In fact, the bulk magnetic behavior of a material

can be characterized by considering how adjacent magnetic moments could well interact with one another at temperatures close to the absolute zero because, depending on composition. At high temperatures all materials behave as paramagnets due to their effective paramagnetic behavior occurring above their critical temperatures.

Certain materials exhibit spontaneous magnetization in the absence of an external magnetic field. This is a collective phenomenon known as ferromagnetism, caused by the spontaneous ordering of the atomic magnetic moments due to the exchange interaction between the electron spins in the solid. If the spins of nearby nuclei are aligned in an antiparallel setup, there is no net magnetization due to a negative exchange interaction. This behavior is known as antiferromagnetism. Magnetization can be detected when nearby spins are aligned in an antiparallel way but have different magnitudes. The term for this phenomenon is ferrimagnetism. Figure 3 below shows different magnetic moment alignments.

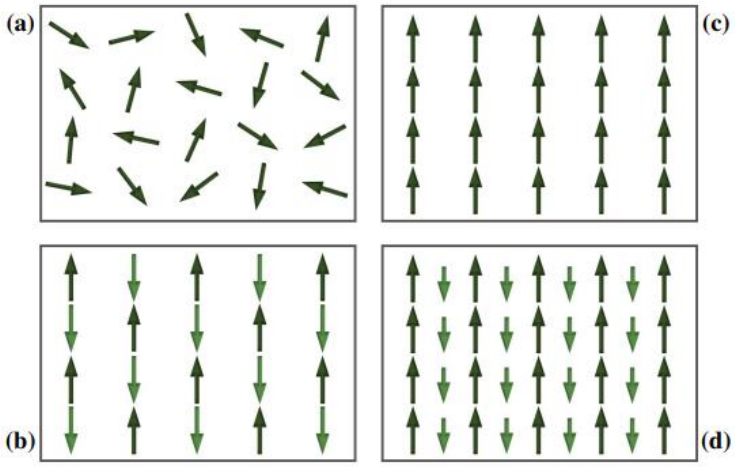

*Figure 3: Magnetic moment alignments: (**a**) paramagnetic, (**b**) antiferromagnetic, (**c**) ferromagnetic, and (**d**) ferrimagnetic. Adapted from [16].*

As shown in Figure 5a, the magnetic field dependence of the magnetization in a bulk material can exhibit a curve that is usually called hysteresis loop. As the magnetic field is increasing the magnetic moments of the unpaired electrons tend to orient in its direction, and as the field grows, so does the magnetization, until it reaches a maximum value, the magnetic saturation (M_s), which corresponds to the alignment of all the spins in the sample. As the magnetic field drops, so does the magnetization, yet the system will retain some magnetization (M_r), and hysteresis is observed. The coercive field (H_c) is the strength of the opposing field required to remove the magnetization of a sample after saturation. Below their critical temperature, ferromagnetic and ferrimagnetic materials show hysteresis. The shape of the hysteresis loop is determined by the reorganization of the domain walls and, consequently, the physical

and chemical properties of the materials. These substances, known as hard magnets (Figure 4a), also possess a high magnetic remanence, demonstrating a memory effect. On the other hand, soft magnets (Figure 4b) exhibit narrower hysteresis loops. Materials with high remanent magnetization can retain their magnetism in certain conditions as a memory effect, which favors their use in industrial applications, such as in memory devices. Materials with low remanent magnetization, on the other hand, can be used in read-write components for those magnetic memory devices.

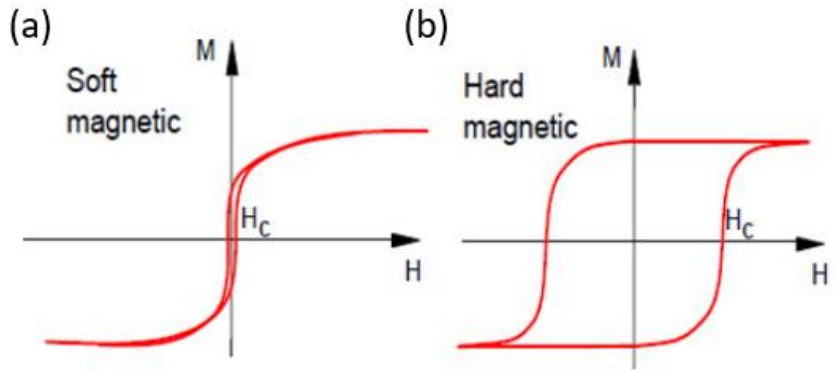

Figure 4: Left: Hysteresis loop of soft magnetic materials. Right: Hysteresis loop of hard magnetic materials [17].

In a ferromagnetic or ferrimagnetic material, the effect of the magnetic field can also influence the thermal behavior of the magnetization. In order to infer the presence of a magnetic transition, a set of measurements with the temperature dependence of the magnetization can be performed using zero-field cooling (ZFC) and field cooling (FC) processes. This consists of cooling the sample at zero field, measuring as a function of temperature on heating under field (ZFC) and then applying the same value of magnetic field and cooling again followed by the measurement of the magnetization as a function of temperature (FC). The irreversibility of both curves below a given temperature, called Curie temperature, T_C, shows that the material behaves as a ferromagnet (or ferrimagnet) below that temperature value.

Ferromagnetic or ferrimagnetic materials can change their magnetic behavior to superparamagnetic at the nanoscale. Usually, it encompasses nanoparticles with a size smaller than the critical diameter (D_c). The average magnetization value of these nanoparticles is zero in the absence of an external magnetic field, which means that they do not exhibit coercive field and remanent magnetization (Figure 5a). In the presence of an external magnetic field, unlike paramagnetic materials, they exhibit very high magnetic susceptibility due to their ferromagnetic origin. Additionally, these nanoparticles are so small (around 3 – 100 nm) that they cease to be multi-domain and become single domain. Figure 5b, below, shows a correlation between particle size, domain, and coercivity.

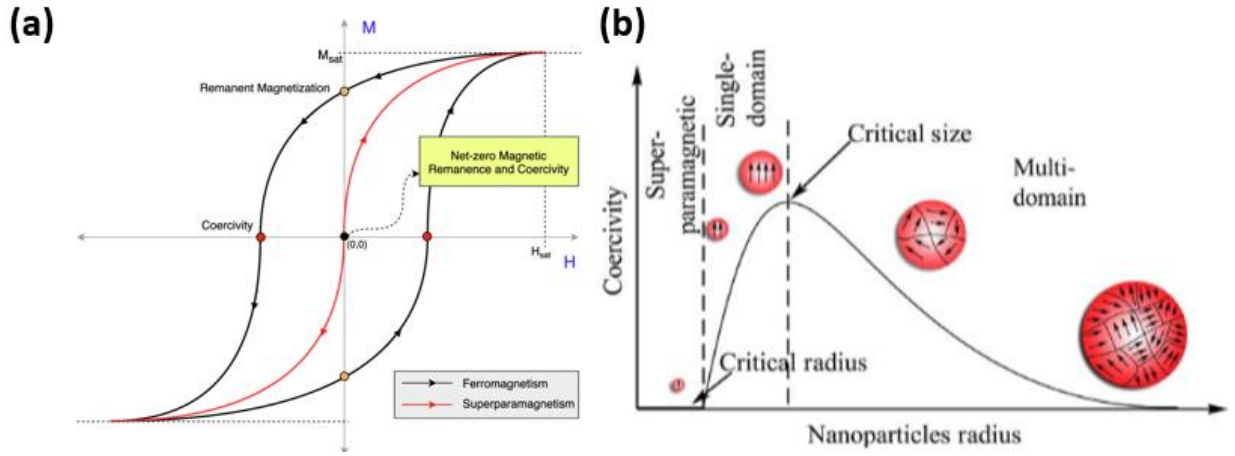

Figure 5: (a) Schematic representation of the difference between ferromagnetic or ferromagnetic and superparamagnetic behavior; (b) Correlation between particle size, domain, and coercivity.

In nanomaterials, the temperature dependence of magnetization curves shows at the point of irreversibility of both the ZFC, and FC curves a blocking temperature (T_b). Below this threshold, the magnetic moments are considered as blocked, and the material presents ferromagnetic or ferrimagnetic characteristics. Above T_b, nanoparticles have superparamagnetic behavior. The magnetic moments of each nanoparticle remain arbitrarily aligned upon the removal of the external field, resulting in a total magnetic moment of zero. These temperature and size-dependent responses of free nanoparticles are due to the competition between the energies of the system, the magnetic anisotropy and thermal energies. Hence, below a minimum size the particle remains blocked. Equation (3) represents the Néel-Arrhenius model, where τ_N, the Néel relaxation time, is the average time between two flips; τ_N can range between nanoseconds and years; τ_0 is the time period; K represents the magnetic anisotropy of the particle; V represents the volume of the particle; T represents the temperature; and K_b represents the Boltzmann constant.

$$\boldsymbol{\tau_N} = \boldsymbol{\tau_0} e^{(\frac{KV}{K_B T})} \quad (3)$$

2.2 Superparamagnetic Iron Oxide Nanoparticles (SPIONs)

The superparamagnetic iron oxide nanoparticles (SPIONs) are one of the most extensively researched targeted nanomaterials because of their exceptional superparamagnetic capabilities, which enable them to heat when submitted to an external alternated magnetic field. These nanoparticles have been studied in the past decades to be used in the biomedical field due to their theranostic properties, such as contrast agents for Magnetic Resonance Imaging (MRI), drug delivery, hyperthermia, biosensing, among others [11]. One of the factors hindering their clinical use is the tendency of the magnetic nanoparticles to aggregate and oxidize *in vivo* with concomitant loss of its magnetic performance. In the absence of an external field, they do not retain magnetization and, although it is considered that no magnetic interactions exist between superparamagnetic nanoparticles, in high-ionic-strength solutions, as the biological media, aggregation is often observed due to interactions with surrounding blood proteins or biomolecules, compromising *in vivo* efficacy. Thus, to circumvent these limitations, modulation of the nanoparticles surface with polymers (natural or synthetic) or using inorganic materials, such as silica or gold coatings are used [18]. Therefore, it is essential, for their use in the biomedical field, that they are coated, since it will reduce the aggregation, improve colloidal stability and biocompatibility, and give them hydrophilicity [12]. If not, SPIONs usually gather into bulk formations and disperse in colloidal fluids. Nevertheless, depending on their origin, quantity or length, and composition, these surface coatings can change the SPIONs' natural magnetic characteristics [19]. For instance, the SPION magnetization performance is unaffected by polyoxyethylene nonylphenylether with an OH end group, oleic acid, and Poly(ethylene glycol (PEG) and dextran polymers with shorter chains [20–22]. Coated particle magnetization values are dramatically reduced by longer chain PEGs and dextran [20]. Additionally, coating allows the conjugation of inorganic or organic components and consequently the possibility of functionalization, making them highly desirable for use in biomedical settings. The most applied coatings are polymers like the PEG, Dextran, Polyvinyl Alcohol (PVA), Polyvinylpyrrolidone (PVP), and chitosan.

Incorporating SPIONs into liposomes has been the subject of numerous studies, leading to the development of magneto-liposomes that are useful multifunctional nanoplatforms for imaging and chemotherapeutic applications, integrating their properties as a contrast agent and drug delivery [12]. Another interesting possibility would be to coat these nanoparticles with gold, which is the case in this study, because gold is very biocompatible, has low cytotoxicity, and is very easy to functionalize with other cancer therapy drugs, contrast agents, targeting agents, and others [23].

SPIONs' magnetic behavior is mostly determined by their shape, size, and size distribution. Several studies have investigated this dependence using static and dynamic magnetometry and Mössbauer spectroscopy to look to parameters such magneto-crystalline and shape anisotropy, interparticle interactions, and magnetic relaxation processes [20, 24, 25].

The three common types of iron oxides, that may be present in SPIONs cores, are magnetite (Fe_3O_4), maghemite (γ-Fe_2O_3), and hematite (α-Fe_2O_3), but only the first two of them were observed in this work. These different iron oxides can be distinguished by different characteristics, such as molecular size and their magnetic parameters [26].

2.2.1 Magnetite

Magnetite is a black iron oxide with formula unit Fe_3O_4, and inverse spinel structure. It forms a face-centered cubic (FCC) network with a lattice parameter of 8.3967 Å (JCPDS file 19–629). A unit cell of magnetite is composed of tetrahedral sites that are occupied by Fe^{3+} ions and octahedral sites that are occupied by both Fe^{2+} and Fe^{3+} ions. Each unit cell is formed by a set of eight sites as shown in Figure 6. Thus, another representation of the formula for magnetite can be written as $[Fe^{3+}]_{tetrahedral}[Fe^{2+}\ Fe^{3+}]_{octahedral}O_4$ [27].

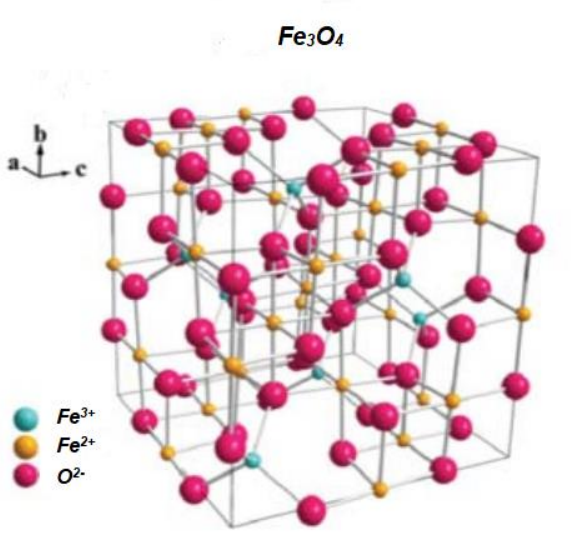

Figure 6: Three-dimensional crystal structure of Fe_3O_4 nanoparticles. Adapted from [28].

In the tetrahedral sites are located eight Fe^{3+} ions each occupying the center of a tetrahedron whose vertices are filled with oxygen ions, and in the octahedral sites are located 16 iron ions (8 Fe^{2+} and 8 Fe^{3+}), each occupying the center of an octahedron whose vertices are filled with oxygen atoms.

In its unaltered state, magnetite is considered a ferrimagnet and compared to other transition metal oxides, is the one with the strongest magnetic characteristics [29]. When a ferrimagnetic material is exposed to an external magnetic field, it retains some of its magnetization long after the field is turned off. The

magnetic moments maintain their alignment even in the absence of a magnetic field. Their magnetization moment M exhibits a hysteresis loop as a result in relation to the external magnetic field H. However, Fe_3O_4 crystals with a diameter of 20 nm or less do not retain the magnetization when the magnetic field is removed and it is denominated as superparamagnetic (there is no hysteresis after applying an external magnetic field because each crystal acts as a single magnetic domain). In other words, bulk magnetite retains its magnetic properties even in the absence of an external magnetic field, whereas SPIONs only exhibit their magnetic properties when exposed to an external magnetic field [26].

2.2.2 Maghemite

Maghemite is a red-brown iron oxide, its unit formula is γ-Fe_2O_3, and it has similar physical and structural properties to magnetite although with a lower magnetic moment. The main difference between the two crystalline phases is the presence of Fe^{3+} as the only cation in maghemite. Maghemite presents a cubic crystalline structure of the inverse spinel type with a lattice parameter of 8.3515 Å (JCPDS file 39–1346) and can be described as a result of the oxidation of magnetite. During the oxidation process one Fe^{2+} ion moves from the octahedral site leaving a vacancy (□) in the crystal lattice and another two Fe^{2+} ions oxidize into Fe^{3+}. Thus, each unit cell of maghemite contains eight Fe^{3+} cations that occupy the 27 tetrahedral sites, the remaining cations (eight located in the octahedral sites plus 5.33 ions from the oxidation of Fe^{2+} ions), and vacancies (2.67 from the oxidation of the eight Fe^{2+} ions) are randomly distributed in the octahedral sites, with conversion of the spinel crystal structure, as represented in Figure 7. Thus, maghemite can be represented by the formula $[Fe^{3+}_8]_{tetrahedral}[Fe^{3+}_{13.33}\ \square_{2.66}]_{octahedral}O_{32}$ [27,30]. Despite having distinct magnetic characteristics in bulk, maghemite and hematite (ferromagnetic and antiferromagnetic, respectively) both contain Fe^{3+} ions and become superparamagnetic below a given particle size [26].

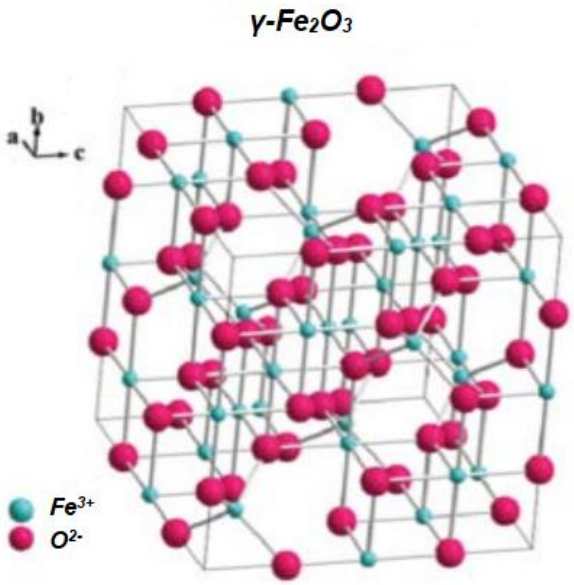

Figure 7: Three-dimensional crystal structure of $\gamma - Fe_2O_3$ nanoparticles. Adapted from [28].

Due to the crystalline similarities between magnetite and maghemite, the powder X-ray diffraction technique that allows the structural determination is not able to differentiate these two crystalline structures only by the positions of the diffraction peaks, because they are quite similar. However, the phase distinction can be determined from techniques such as Mössbauer spectroscopy that is able to estimate the distribution of cations for the spinel-like structure by distinguishing Fe^{2+} from Fe^{3+} and the correspondent surroundings, and determines the crystalline phase of the material [27].

2.3 SPIONs Biomedical Applications

Magnetic nanoparticles for biomedical applications can be divided into two classes according to a specific application: *in vitro* and *in vivo*. In *in vitro* applications, the particles are in biological media taken from living things or in media that simulate biological media. In *in vivo* applications, the nanoparticles will be in living organisms, so they must be biocompatible or present toxic action only in the tissue of interest.

For the use of SPIONs in biomedical applications, the species present on the surface of the nanoparticles play a role of equal or even greater importance than the nature of the magnetic core. These nanoparticles form stable solutions in aqueous or organic media depending on the ligands present on the surface. The ligands can be divided into two classes when it comes to the nature of the stabilization promoted. Electrostatic stabilization (Figure 8a) uses a charged compound that is usually adsorbed onto

the surface of the nanoparticles and prevents them from aggregating. Steric stabilization (Figure 8b) uses long chain organic ligands that create a mechanical barrier that prevents the nanoparticles from aggregating.

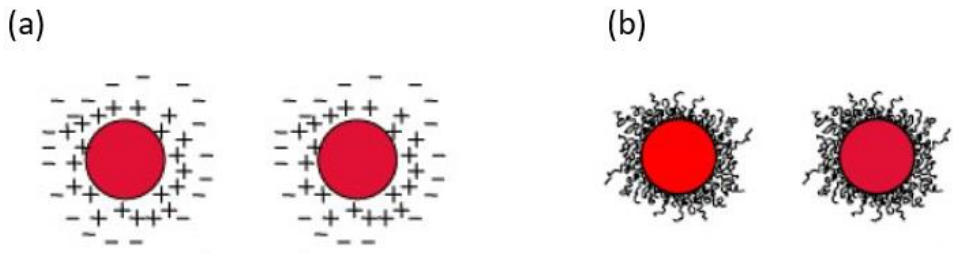

Figure 8: Scheme representing electrostatic stabilization (a) and steric stabilization (b).

Polymers such as Dx and Dx-NH2 used in this thesis are used not only to stabilize the nanoparticles but also to reduce their toxicity [31]. Gold coated structures with magnetic cores have been attracting attention for the possibility of adding magnetic properties to the protective surface, biocompatible with the properties of nanometric gold [32].

There are several biomedical applications for SPIONs, but only MRI and magnetic hyperthermia will be discussed as the nanoparticles in this work target such applications.

2.3.1 Magnetic Resonance Imaging (MRI)

Magnetic resonance imaging (MRI) has stood out among other imaging techniques because of the better quality of the images, which are obtained by the relaxation observed in the precession motion of protons in different tissues after they are excited. This technique provides images of the anatomical structures and can be further sharpened with the use of contrast agent. Magnetic nanoparticles contrast agents are extremely effective in enhancing the proton relaxation process. SPIONs are more biocompatible than gadolinium or magnesium-based contrast agents since iron is quite abundant in the human body [33]. In addition, SPIONs exhibit superparamagnetic properties and biodegradability, and their interface is easily modifiable to improve their pharmacokinetics and biocompatibility.

The fact that nanoparticles limit their size to a few nanometers allows an increase in their circulation time in the bloodstream and a more efficient control regarding contrast effects and biological functions and interactions [33], allowing them to function at the cellular and molecular level [34]. Thus, in recent years, the interest in magnetic nanoparticles has been increasing significantly due to their applicability in several areas [35], being their use as contrast agents in MRI one of the most important and fastest growing [36].

Indeed, their nanodimensions give rise to unique magnetic properties [34], and it is mainly the combination of these two characteristics that makes magnetic nanoparticles such a promising contrast agent in MRI applications [34].

There are two mechanisms to describe magnetic relaxation. In the first, the internal magnetization vector of the nanoparticle relaxes in the direction of the easy axis, known as Néel relaxation. In the second, the nanoparticles follow rotational diffusion in a carrier liquid, called Brownian relaxation [37]. The Néel and Brown relaxations can be distinguished by their different characteristic times. Moreover, Brownian relaxation can only be measured in liquids, whereas Neel relaxation does not depend on the dispersion of the nanoparticles.

Two parameters of the magnetic resonance phenomenon widely used for the study of contrast agents result from the relaxation process of the spins after the termination of the 90° excitation pulse. These parameters are the transverse relaxation time (T2) and the longitudinal relaxation time (T1). SPIONs, for example, locally increase the externally applied magnetic field, producing heterogeneity in the magnetic field which in turn enhances T1 and T2 relaxation, and in most situations has significant ability to reduce the T2 relaxation time to be used.

As in this work it was synthesized SPIONs functionalized with Gadolinium, these NPs can be used as dual mode (T1/T2) contrast agents, with gadolinium as a T1 agent and SPIONs, depending on the particle size, serving as either T2 or T1.

2.3.2 Magnetic Hyperthermia

The goal of hyperthermia therapy is to harm and kill cancer cells by heating tumor tissues about 5-6 degrees Celsius using an alternated magnetic field. Since some cancer cells are resistant to the use of radiation or medication therapies but particularly susceptible to heat, it can also make them sensitive to other treatments. There are three main types of hyperthermia treatment. Local hyperthermia is targeted at small tumors (≤3 cm to 5-6 cm) in superficial regions or in places of easy access. The regional hyperthermia has its application focused on more developed tumors, and consequently is used in more extensive areas of the body. The whole-body hyperthermia is used when the tumor is in a metastasis state [38].

In magnetic hyperthermia, SPIONs are exposed to an external magnetic field that alternates at a frequency suitable to promote the reversal of the magnetic moment of the nanoparticle. The relaxation processes result in the release of this energy in the form of heat, which causes cancer cells to die by intracellular acidosis at temperatures around 42 ºC while healthy cells are preserved because they die at temperatures between 46 and 47ºC [39,40].

Heat can be defined taking into account the mechanism of hysteresis loss and relaxation losses. Hysteresis loss occurs in multidomain particles in which their magnetic moments are oriented toward the external magnetic field, when reversing the direction of the applied field, there is an energy difference that is released in the form of heat. In the case of SPIONs, which are single-domain nanoparticles and do not exhibit hysteresis, when the external alternating magnetic field is applied, heat dissipation happens by the Néel and Brownian relaxation motion. As already referred in the above section, by the Néel motion, the magnetic moments of the nanoparticles rotate to an orientation close to the field without rotating the nanoparticles, and when they reach their equilibrium state, they relax, and the energy is converted into heat. By the Brownian motion, SPIONs rotate in the fluid of the suspension they are in, resulting in friction that releases energy in the form of heat [41].

There are numerous techniques to deliver these nanoparticles to the target, including intravascular infusion, direct injection, and antibody targeting [42]. In intravascular infusion hyperthermia, nanoparticles are introduced via a plunger inserted into the blood vessels supplying the tumor, delivering nanoparticles to the tumor tissue, and promoting intravascular heating. In direct injection hyperthermia, the nanoparticles are injected directly into the tumor promoting heating at the extracellular environment. On the other hand, in hyperthermia by antibody-targeting, SPIONs with special coatings are injected into the bloodstream, penetrating the tumor tissue, and being incorporated by its cells, which promotes intracellular heating [43,44]

The first clinical trials with magnetic nanoparticles were published were published by *Jordan et al., 1993* [45] Researchers created a unique prototype hyperthermia-producing device that was effective to treat tumors in several areas of the body by inducing alternated magnetic fields. In order to treat recurrent multiform glioblastoma [46], evaluated the efficacy and tolerance of newly developed thermotherapy with magnetic nanoparticles. In this study, they employed SPIONs coated with aminosilane that were inserted into the tumors of 14 patients. Then, to produce particle heating, patients were exposed to a changing magnetic field. Patients reported little to no side effects from this type of SPIONs therapy. Maximum measured abdomen temperatures ranged from 42.4 to 45.5 C, and local tumor regression symptoms were observed. In conclusion, individuals with multiform glioblastoma may benefit from deep cranial thermotherapy with SPIONs as a viable therapeutic option that can be administered without risk [47].

2.4 SPIONs Synthesis

Magnetic nanoparticles (MNPs) can be obtained by several physicochemical methods such as thermal decomposition, co-precipitation, hydrothermal method, and microemulsion. The synthesis by co-precipitation is the most widely used due to its versatility and simplicity. However, when size control and low size dispersion are desired, thermal decomposition is one of the best options. Microemulsion shows good control results [48–51] being an alternative route when the desired goal is low size dispersion of the nanoparticles. The hydrothermal method allows obtaining NPs with different morphologies due to the ability to control the direction of growth of these compounds. However, the size dispersion of the particles obtained by this method is relatively high. Table 1 summarizes general considerations of chemical synthesis cited above as well as the parameters of the final product.

Table 1: Comparison of chemical synthesis methods in the production of SPIONs. Adapted from [52].

Synthesis Method	Temperature (ºC)	Pressure (atm)	Synthesis period (h)	NP Average size (nm)	M_s at RT (Am^2/Kg)
Co-precipitation	25 - 70	1	0.5 - 1	3 - 15	50 - 85
Microemulsion	4 - 90	2	3 - 20	3 - 12	30 - 60
Thermal Decomposition	100 - 400	2	20 - 24	4 - 20	20 - 85
Hydrothermal	80 - 160	Up to 136	0.5 - 48	10 - 80	7 - 75

In the co-precipitation method attention should be given to parameters that affect the final size and form of the NPs [53], such the ratio of ferric to ferrous ions, the reaction temperature, the pH value, the stirring rate, the pouring speed of ammonium hydroxide (NH_4OH), and the ionic strength of the media. *Gnanaprakash et al.* [54] have observed how the digesting time and alkali addition rate affect the size and magnetic characteristics of magnetite NPs created during chemical precipitation. As the dimensions of the NPs become lower, their M_s drops. The temperature, stirring rate, time, pH, and the precursor content were all found to also show the same effect [55].

2.4.1 Dextran

Dextran is a natural polymer composed of linear α-1,6-D-glucopyranose units with a low percentage of attached side chains. This polymer can be obtained by the synthesis process by natural fermentation, through the action of the dextransucrase enzyme from the *Leuconostoc mesenteroides* bacterium in the

presence of sucrose, and synthetically through polymerization. Dextran is easily soluble, biodegradable, non-toxic, and can be obtained in a variety of molecular weights by enzymatic hydrolysis. This polysaccharide is used as an important reagent in the wide range of synthesis in the biotechnological and technological industries. The use of dextran also has the advantage that it can be used as a multifunctional vehicle for theranostic purposes, since it allows the coupling in the same chain of drugs, metal complexes, organic dyes, biomolecules, etc. [56].

In this work, two types of dextran were used to cover SPIONs, one is the regular dextran (Dx) and the other is the amino - dextran (Dx – NH_2) [56]. Both polymers were subsequently coated with gold to evaluate the effectiveness of the gold coating on the SPIONs, since the NH_2 group has an affinity for gold. Figure 9a represents the molecule of Dx while Figure 9b represents Dx - NH_2.

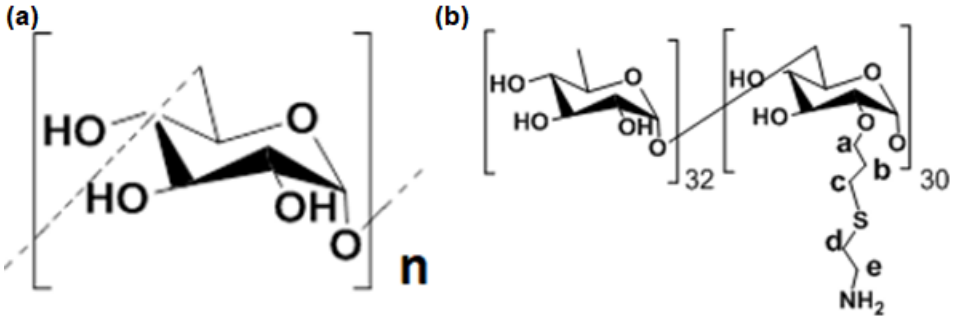

Figure 9: Molecule of Dx (a) and Dx - NH2 (b)

2.4.2 Gold Coating

Gold occupies a remarkable position in the history of science and technology. With the development of nanotechnology, the use of gold in medicine, especially in studies involving cancer diagnostics and therapy, has increased in recent years. The use of gold nanoparticles is also growing in the cosmetic sector with applications in aesthetic treatments such as facial rejuvenation and hydration due to gold being a material that presents antioxidant properties [57]. The main advantages of gold are biocompatibility, relatively simple synthesis control of the size of the nanoparticles, the easy chemical modification of its surface and easy bioconjugation with other cells when coated with specific markers [58].

As in the case of this thesis, core-shell nanoplatforms can be obtained by coating SPIONs core with a gold layer. Reduced toxicity, colloidal stability, and more versatile platform for bioconjugation are one of the benefits of the gold coating [59]. In addition, the nanoscale gold coating has a plasmonic surface, which results in significant optical absorption in the visible and near infrared region (NIR). These characteristics make gold nanoparticles potential heating-inducing agent for photothermal cancer therapy,

where heating is accomplished through the irradiation of light [60], causing an ablation of the tumor cells, destroying the cell membranes [61, 62].

2.4.3 Gadolinium in MRI

The most popular lanthanide element for use in medicinal imaging as contrast material is gadolinium. Like other lanthanides, its most frequent oxidation state is the trivalent and it is considered a hard acid and exhibits high coordination numbers between 8 and 10 [63, 64]. The development of MRI and the creation of contrast materials for this imaging modality are directly related to its usage in medicine. The choice of Gd^{3+} for MRI applications can be explained by its slow electronic relaxation and seven unpaired electrons, which make it a stable ion [65]. Small chelates represent the majority of the gadolinium-based contrast agents used as positive contrast agents [66].

Above certain amounts, gadolinium concentrations are toxic to human bodies. Therefore, gadolinium present in all contrast agents is stabilized by chelating agents, forming complexes with high thermodynamic stability. However, small amounts of free gadolinium have been found after MRI exams. Due to this drawback, efforts have been made to develop strategies to obtain this contrast agent in a less toxic way. One of the strategies is the development of new chelating agents and others are the functionalization of nanoplatforms since each nanoparticle can carry thousands of atoms of Gadolinium [67]. In this work, the chelating agent used was 2-[4,7-bis(carboxymethyl)-10-[2-(3-sulfanylpropanoylamino)ethyl]-1,4,7,10-tetrazacyclodec1-yl]acetic acid (TDOTA) that binds to the SPIONS gold coating through gold-sulfur bonds (Figure 10a) and ionic gadolinium complexation (Figure 10b).

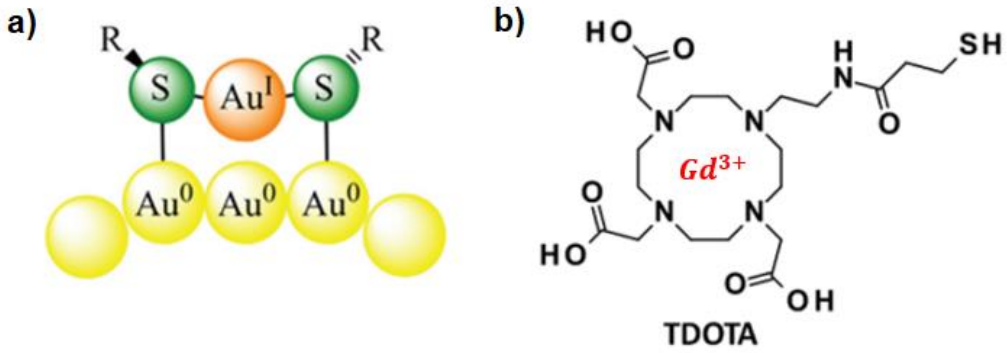

Figure 10: Scheme of gold-sulphur bonds establish at the gold coating (a) and TDOTA chelator agent for Gd^{3+} complexation (b).

Chapter 3

Experimental Procedure

3.1 Materials

All chemicals and solvents were of reagent grade and were used without additional purification, unless otherwise stated, and were commercially acquired from Aldrich Chemical. The deionized water was produced from a Millipore system Milli-Q ≥18 MΩcm (with a Millipak membrane filter 0.22µm).

The following materials were used in the preparation of the SPIONs: Iron (III) chloride hexahydrate ($FeCl_3.6H_2O$), iron (II) chloride tetrahydrate ($FeCl_2.4H_2O$), sodium sulfite ($NaSO_3$), ammonium hydroxide (NH_4OH) (25%), hydrochloric acid (HCl, 37%), dextran (Dx) from *Leuconostoc mesenteroides* (average mol wt. 9.000-11.000), amino – dextran (Dx-NH_2), sodium hydroxide in pellets (NaOH), gold (III) chloride acid trihydrate ($HAuCl_4.3H_2O$), sodium borohydride ($NaBH_4$), and gadolinium (III) chloride ($GdCl_3$) .

The polymeric precursors Dx-NH_2 [56] and the ligand 2-[4,7-bis(carboxymethyl)-10-[2-(3-sulfanylpropanoylamino)ethyl]-1,4,7,10-tetrazacyclododec1-yl]acetic acid (TDOTA) [33] were previously synthesized and characterized in the Radiopharmaceutical Sciences Group (C^2TN/IST) and kindly provided by Maria Paula Cabral Campello

The PC3 cell line was obtained from ATCC, Manassas, VA, USA.

3.2 SPIONs Synthesis

The nanoparticles investigated in this work were synthesized by the co-precipitation method but with different approaches for each process.

Co-precipitation is possibly the simplest method for creating nanoparticles of iron oxide. It is possible to employ materials and chemical agents that are harmless and biocompatible, making them suitable for biomedical applications. It is possible to create a fine suspension of NPs with diameters as small as 5 nm by carefully manipulating the reaction conditions. A strong base is added to a solution of, Fe^{2+} and, Fe^{3+} in a molar ratio of 1:2 under an inert or atmospheric environment, resulting in a precipitate Fe_3O_4. Equation (4) shows the co-precipitation reaction for obtaining SPIONs:

$$Fe^{2+}{}_{(aq)} + 2Fe^{3+}{}_{(aq)} + 8OH^{-}{}_{(aq)} \rightarrow Fe_3O_{4_{(s)}} + 4H_2O_{(l)} \quad (4)$$

3.2.1 A Samples (Iron Reduced with Na_2SO_3)

The synthesis of Naked SPIONs A (A01) was based on the method described by *Matos et al., 2019* [20], consisting of Fe^{3+} reduction with Na_2SO_3 followed by Fe_3O_4 precipitation through titration with NH_4OH. The precursor was separated by centrifugation and lyophilized.

In a representative reaction, a solution of 4.5 g (16.67 mmol) of $FeCl_3.6H_2O$ in 2.5 mL of HCl (2M) and 2.5 mL of deionized water was carefully added to a solution of 420 mg (3.33 mmol) of Na_2SO_3 in 3 mL of deionized water and stirred at a moderate level at RT and P_{atm}, for 30 minutes. A solution containing 125 mL of NH_4OH (25% w/w) was then added dropwise to the previous solution. Due to the precipitation of Fe_3O_4, the color of the solution becomes dark during this phase. The final product was magnetically stirred for approximately 24 h, centrifuged 4000 RPM for 10 min and washed twice with deionized water. After freeze-drying the reaction product, 644 mg of SPIONs Naked (A01) were obtained. Figure 11 shows SPIONs A01 before freeze-drying.

Figure 11: Washed SPIONs (A01) prepared for lyophilization/freeze-drying.

3.2.2 B Samples (Post hydrothermal treatment)

For Naked SPIONs B (B01) a method adapted from *Soares et al., 2014* [67] was followed, consisting of a standard co-precipitation process (4), using Fe^{3+} and Fe^{2+} in a 2:1 mol ratio followed by Fe_3O_4 precipitation using NH_4OH and it was subjected to a post hydrothermal treatment in an effort to control the growth of the nanoparticles size. The precursor was separated by magnetic separation and lyophilized.

In order to obtain a molar ratio of 2:1 (Fe^{3+}:Fe^{2+}), 5 mmol of $FeCl_3.6H_2O$ and 2.5 mmol of $FeCl_2.4H_2O$ were dissolved in 25 mL of deionized water. Under mechanical stirring, 10 mL of ammonium hydroxide NH_4OH (25%) was quickly added to initiate the reaction. The color change of the mixture from orange to black evidenced the formation of Fe_3O_4 (Figure 12). After 5 minutes, the reaction was stopped by adding 60 mL of deionized water. The total synthesis was performed in nitrogen atmosphere (N_2) in an effort to minimize the oxidation of the synthesized SPIONs. The SPIONs obtained were washed 5 times with deionized water using a strong magnet and then dispersed in water.

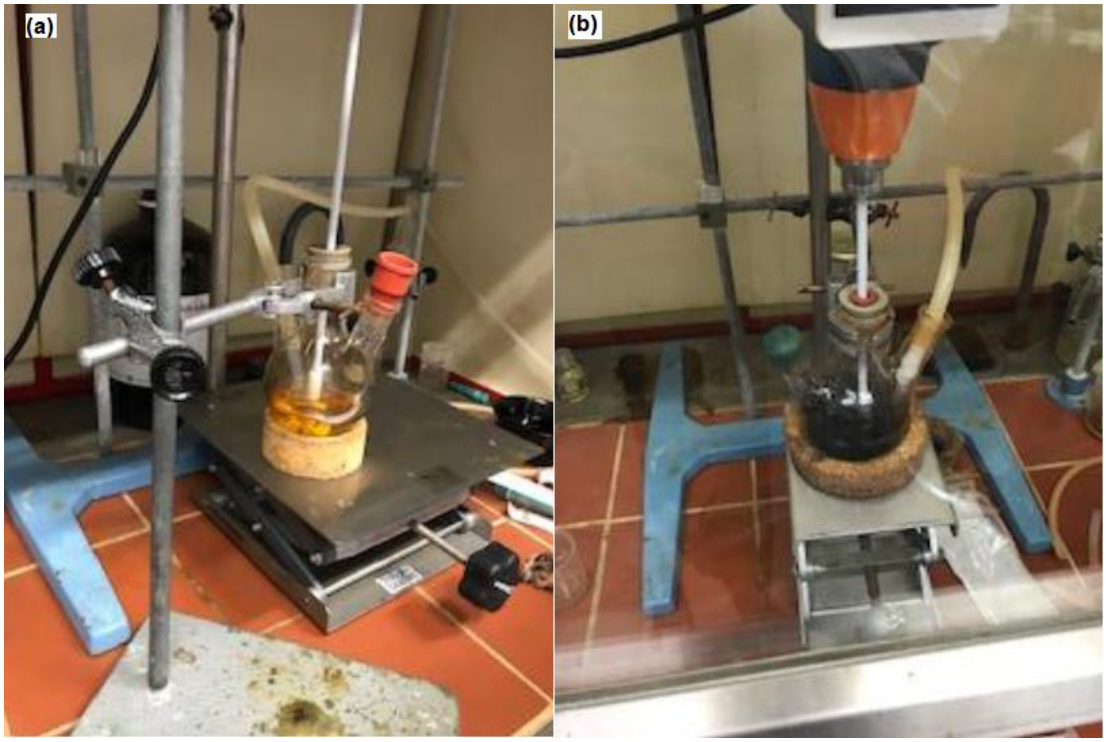

Figure 12: Dissolution of iron ions before the precipitation, presenting yellow color (a) and the Fe_3O_4 precipitate during/after addition of NH_4OH, presenting black color (b).

3.2.2.1 *Hydrothermal treatment*

75 mL of SPIONs solution was heated inside the vessel of the equipment to 160 °C and the temperature was kept constant for a reaction time of 16 hours. The container was naturally cooled to room temperature for 3 hours. The resulting precipitate was washed 4 times in deionized water, to remove the remaining impurities from the SPIONs and dispersed into deionized water for freeze-drying during 24 hours.

3.2.3 C Samples (Controlled environment at pH 9.6)

Naked SPIONs C (C01) was based on the method of *Saraiva et al., 2021* [68] which consists of a standard co-precipitation process (4) but with Fe^{3+} and Fe^{2+} in the proportion of 1:2 mol, respectively. This is an attempt to increase the number of Fe^{2+} ions in solution since the structure that we aim to obtain in larger quantities is magnetite, because it has a better magnetic behavior, and for its formation it is necessary to have a good quantity of Fe^{2+} ions in solution because these oxidize easily to Fe^{3+}. The Fe_3O_4 was precipitated using NH_4OH and the precursor was separated by decantation and lyophilized.

In a typical reaction two solutions of $FeCl_3.6H_2O$ (0.01M) and of $FeCl_2.4H_2O$ (0.02M), were prepared and then mixed. The resultant solution was taken to de-aerate with N_2 for 10 minutes to remove excess oxygen bubbles that could oxidize the iron. After deaeration, NH_4OH (25% w/w) was slowly poured into the solution to promote Fe_3O_4 precipitation. By the time the solution meets the ammonium hydroxide, it is already possible to observe the precipitation by the color change of the solution from yellow to black. Ammonium hydroxide was added until the pH of the solution reached 9.6. The solution was set aside to decant for 24 hours (Figure 13) and was non-washed. The water excess was removed, and the precipitate was lyophilized.

Figure 13: Solution decantation.

3.2.4 Dextran Coating

Two different polymeric coating based on dextran were used to cover the naked SPIONs. A01 was covered with dextran (Dx) from *Leuconostoc mesenteroides,* average mol wt. 9.000-11.000 and B01 was covered with Dextran-NH_2 (Dx-NH_2) [56]. The procedure used in both syntheses was based on the method reported by *Matos et al., 2019* [20].

3.2.4.1 Dextran SPIONs (A02)

A 50 mL solution (9.1 mg/mL) of Naked SPIONs (A01) containing 6 mL of NaOH (0.5M) was slowly added to a polymer solution of 240 mg dextran (Dx) dispersed in 6 mL of NaOH (0.5M) under intense magnetic stirring. After complete addition , the reaction was left for 24 hours under moderate magnetic stirring at RT, covered with aluminum foil. The solution was centrifuged the first time to remove its excess polymer. The Dextran SPIONs (A02) were then washed four times with deionized water for 10 minutes at 4000 RPM. The pH after washing was about 8 to 9. The A02 nanoparticles were freeze-dried for 48 hours.

3.2.4.2 Dextran - NH_2 SPIONs (B02)

An amount of 108,64 mg of Naked SPIONs B01 dispersed in 1.4 mL of NaOH (0.5M) was slowly added to the polymer solution of 56mg of Dx-NH_2 diluted in 1.4 mL of NaOH (0.5M), under intense magnetic stirring and left for 24 hours under regular magnetic stirring. The resultant Dx–NH_2 SPIONs (B02) were centrifuged during 10 minutes at 4000 RPM, to remove the excess of polymer from the solution, then washed four times with deionized water and freeze-dried for 48 hours. The pH of remaining solution was approx. 8-9.

3.2.5 Gold coating

SPIONs gold coated (A03 and B03) were made based on a mixture of methods from *Caro et al., 2021* [69] and *Elbialy et al., 2014* [70].

A solution with 48 mg of Dx SPIONs A02 in 6 mL of deionized water was added to a solution, of 32 mg (81,26 µmol) of $HAuCl_4$ in 3 mL of deionized water at 70ºC resulting in an acidic pH solution between 3 and 4. After 10 minutes, it was observed that the color changed from yellow to reddish. At this point, the solution was left under heat for another 10 minutes and the heating mantle was turned off. Then a solution of $NaBH_4$ (0.37M) was added to the previous solution with the help of a micro-pipette at intervals of 500 uL until a pH of the solution was between 8 and 9. Then it was left under magnetic stirring for 18 hours, covered with aluminum foil and capped. The resulting solution was centrifuged at 4000 RPM for 10 minutes to remove excess impurities and then the coated nanoparticles were washed by centrifugation 2 times with water at 6000 RPM for 10 minutes and were freeze-dried for 48 hours.

Sample B02 was coated with gold by the same way mentioned above resulting B03.

3.2.6 Gadolinium Functionalization

The Gadolinium functionalization was made *via* a TDOTA chelating agent, based on a previous work from the Radiopharmaceutical group of C2TN [71].

Two solutions were made, one with 140mg of A03 and 1mL of ethanol and the other with 140 mg of B03 and 1 mL of ethanol. These solutions were sonicated for 5 minutes. Meanwhile, another two solutions made of 500 µL of ethanol with 140 mg of the chelator agent TDOTA were placed under a magnetic stirring. After sonication, the solutions of SPIONs were placed in a solution of TDOTA and left capped and covered with aluminum foil for 10 hours.

After this process, two solutions consisting of 40 mg (0.108 mmol) of $GdCl_3$ and 5 mL of deionized water each were prepared. One solution was added to A03 with TDOTA and the other to B03 with TDOTA. The solutions were left on the magnetic stirring, capped and covered with aluminum foil for 16 hours. The reaction started at pH close to 6 and ended at pH between 4 and 5. Following this process, the solutions were washed twice with deionized water at 6000RPM for 10 minutes and freeze-dried for 48 hours to obtain the Dextran SPIONs@Au – Gd^{3+} (A04) and Dextran NH2 SPIONs@Au – Gd^{3+} (B04).

All samples made in this work are represented in Table 2 below with their identification and name.

Table 2: Labels for each kind of sample

Samples	Description	Labels
Naked SPIONs	Iron Reduced with Na_2SO_3	A01
Naked SPIONs	Post hydrothermal treatment	B01
Naked SPIONs	Controlled final pH 9.6	C01
Dextran SPIONs (Dx-SPIONs)	SPIONs covered with Dx	A02
Dextran – NH_2 SPIONs (Dx-NH2 SPIONs)	SPIONs covered with Dx – NH_2	B02
Dextran SPIONs@Au	SPIONs covered with Dx, and gold coated	A03
Dextran – NH_2 SPIONs@Au	SPIONs covered with Dx – NH_2 and gold coated	B03
Dextran SPIONs@Au – Gd^{3+}	SPIONs covered with Dx, gold coated functionalized with Gd^{3+} complexed TDOTA	A04
Dextran – NH_2 SPIONs@Au – Gd^{3+}	SPIONs covered with Dx – NH_2, gold coated functionalized with Gd^{3+} complexed TDOTA	B04

3.3 SPIONs Characterizations

SPIONs were characterized by dynamic light scattering and zeta potential (DLS), transmission electron microscopy (TEM), Powder X-ray diffraction (PXRD), Mössbauer spectroscopy, SQUID magnetometry, and magnetic hyperthermia. Iron, Gold and Gadolinium contents were determined by Inductively Coupled Plasma Mass Spectroscopy (ICP-MS).

3.3.1 Powder X-Ray Diffraction

Powder X-ray diffraction (PXRD) is another widely used method to characterize nanoparticles in terms of crystalline structure, crystalline grain size, and lattice parameters. It is also suitable to identify the presence of different phases. Figure 14 illustrates a schematic diagram of PXRD method. Hence, a cathode ray tube generates X-rays that are filtered to produce monochromatic radiation and oriented toward the sample. Thus, the interaction between the incident X-rays and the crystalline sample produces constructive interference and a diffracted ray, when the follow condition is satisfied, shown below (5) (Bragg's Law):

$$n\,\lambda = 2\,d\sin\theta \qquad (5)$$

Where n is a constant in which for this case is used 1, λ is the wavelength of the radiation source, d is the distance between atomic planes and θ is the incidence angle of the source in relation to the sample surface (plane reference).

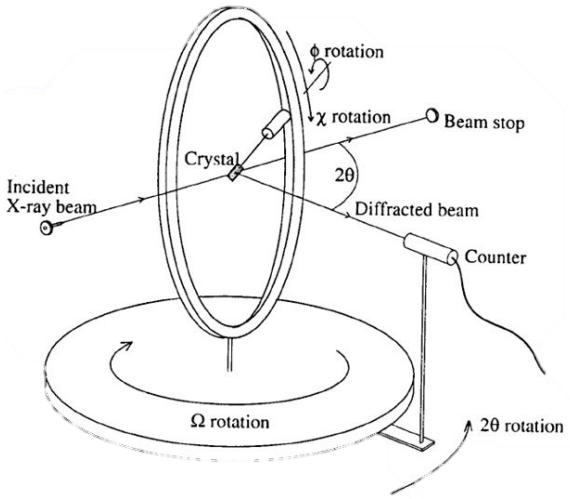

Figure 14: X-ray diffractometer mechanism.

This technique is usually performed in powder samples and the composition of these particles can be determined by comparing the position and intensity of the peaks with the reference patterns that are accessible in the literature. Nevertheless, X-ray diffraction peaks are too broad for particles with a size below 3nm and cannot be applied in amorphous materials [72].

PRXD measurements were performed at C^{2}TN/IST, in a D2 PHASER diffractometer-Bruker with a Cu source and a wavelength of λ = 1.54 Å. The spectrum was collected at room temperature between angles (2θ) of 10º and 80º with a step size of 0.01º, time per step of 10.5 s, 3 RPM, and PSD opening of 3º. For sample preparation, a small volume of sample powder was placed on a standard support used for

this technique, and ethanol was used to settle the powder on it. Figure 15 shows the A01 sample ready for Powder X-Ray Diffraction.

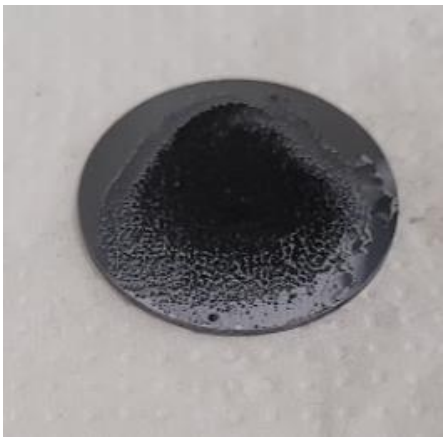

Figure 15: Sample A01 prepared to Powder X-Ray Diffraction.

3.3.2 Mössbauer Spectroscopy

Mössbauer Spectroscopy studies were performed at the Mössbauer Laboratory of the Solid State group at C^{2}TN/IST. Spectra were collected at room temperature and 4 K in transmission mode using a conventional Wissel constant-acceleration spectrometer and a 25 mCi ^{57}Co source in a Rh matrix. The velocity scale was calibrated using α-Fe foil. Isomer shifts, IS, are given relative to this standard at room temperature. The absorbers were obtained by packing the powdered samples into Perspex holders. Absorber thicknesses were calculated on the basis of the corresponding electronic mass-absorption coefficients for the 14.4 keV radiation, according to Long *et al*. 1983 [73]. Low-temperature measurements were performed with the sample immersed in liquid He in a *Janis bath cryostat, model SVT-400*. The spectra were fitted to Lorentzian lines using a non-linear least-squares method. Relative areas and line widths of both peaks in a quadrupole doublet and of peak pairs 1-6, 2-5 and 3-4 in a magnetic sextet were constrained to remain equal during the refinement procedure. Distributions of magnetic splittings were fitted according to the histogram method [74].

3.3.3 Transmission Electronic Microscopy (TEM)

The transmission electron microscopy (TEM) images were obtained on a FEI Tecnai G2 Spirit BioTWIN high resolution transmission electron microscope at the Instituto Gulbenkian de Ciência. The samples for the TEM analyses were prepared by dipping a 300-mesh carbon-coated copper grid into a

solution containing SPIONs previously sonicated. The carbon grid dried for 5 min. Software Image-J was used to process the obtained images in order to determine the average size of the SPIONs. Figure 16 below shows the grid used to store the SPIONs samples.

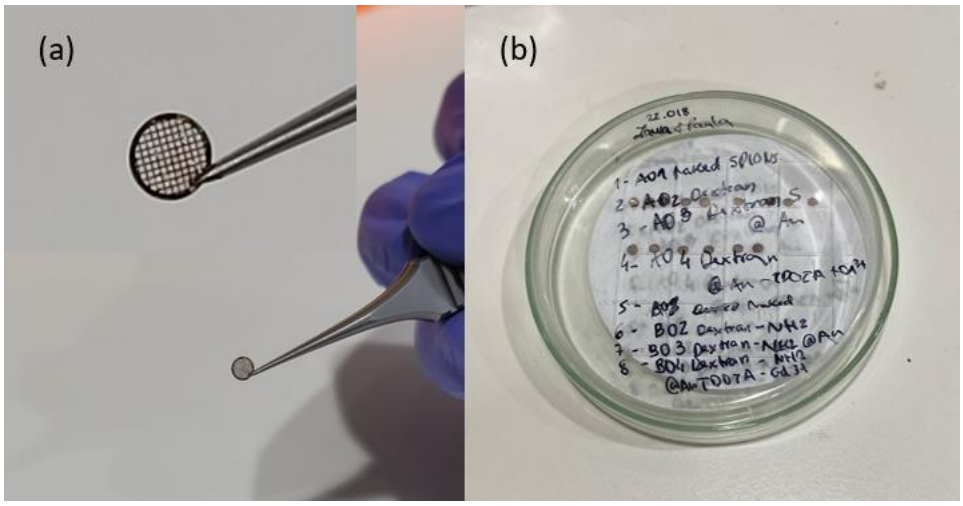

Figure 16: Left: Grid utilized for sample preparation with zoom inset (a) Right: Samples prepared organized (b).

3.3.4 Inductively Coupled Plasma Mass Spectrometry (ICP-MS)

ICP-MS measurements were performed on *Thermo X Series* equipment at the LCA (Laboratório Central de Análises) University of Aveiro. Four dry weighed samples were sent to measure the content of Fe, Au, and Gd in each one.

3.3.5 DLS and Zeta Potential

DLS measurements were performed in C^2TN with a Malvern Zetasizer Nano ZS (Malvern Instruments Ltd., Worcestershire, UK) equipped with a 633 nm He-Ne laser and operating at an angle of 173º. The software used to collect and analyze the data was the Dispersion Technology Software (DTS) version 5.10 from Malvern. 600 L of each sample was measured in low volume semi-micro disposable sizing cuvettes (Fisher Scientific, USA) with a path length of 10 mm (Figure 17). Triplicate measurements were made at a position of 4.65 mm from the cuvette wall with an automatic attenuator. For each sample, 15 runs of 10 s were performed. The hydrodynamic size and the polydispersity index (PDI) were obtained from the autocorrelation function using the “general purpose mode” for all nanoparticle samples. The default filter factor of 50% and the default lower threshold of 0.05 and upper threshold of 0.01 were used. Zeta potential measurements were performed in triplicates using water as a dispersant and the Huckel model. For each sample, 20 runs were performed in auto analysis mode.

Figure 17: Disposable Capillary Cell (DTS1070) from Malvern analytical.

3.3.6 Magnetometry (SQUID)

Static magnetic measurements were obtained using the *SQUID* (Superconducting Quantum Interference Device) magnetometer system of the Solid State group at C^2TN. The SQUID magnetometer is the most sensitive, and perhaps the most widely used technique to measure the magnetic properties of a material. In this work a S700X SQUID Magnetometer from the company Cryogenic Ltd. was used (Figure 18).

Figure 18: S700X SQUID Magnetometer.

The key cryogenic element of this magnetometer is based on a variable temperature sample space insert upon which is mounted the superconducting magnet with the SQUID and magnetic detection coils. At the top of the insert is the sample movement system, an airlock to facilitate changing the sample, and all the electrical feed-through for the device. The sample is placed on a long rod with a low magnetic moment that passes through a helium-tight sliding seal into the sample space. For SQUID to be superconducting, it must be submitted to low temperatures and is therefore immersed in liquid helium. The temperature regulation of the sample is accomplished by drawing a stream of helium gas past the sample. After liquid helium is drawn from the main helium reservoir in the cryostat, and after expansion through an impedance, the gas flows through a heat exchanger, allowing continuous variation of temperature (1.6 K to 400 K). There are two thermometers for temperature control, A and B (Figure 19); thermometer A is located on the heat exchanger and effectively measures the temperature of the gas coming from the heat exchanger to the sample space; thermometer B is positioned in the sample space above the sample position. Once equilibrium has been reached, thermometer B can be taken as the sample temperature. The space of the sample is closed at the top with a gate valve and airlock to enable the change of the sample while the system is cold, avoiding contamination of the cold environment. The cryostat has a liquid nitrogen cooled radiation shield to afford very low liquid helium consumption. The S700X is endowed with excellent immunity to vibration and RF interference due to the solid stainless-steel components of the system [75].

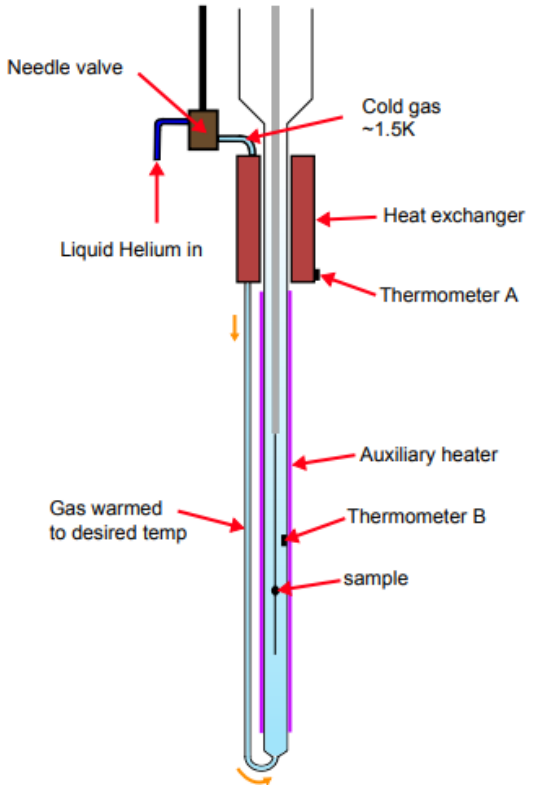

Figure 19: Schematic depiction of temperature control in the S700X [75].

Figure 20 is a detailed cross-sectional view of the whole system:

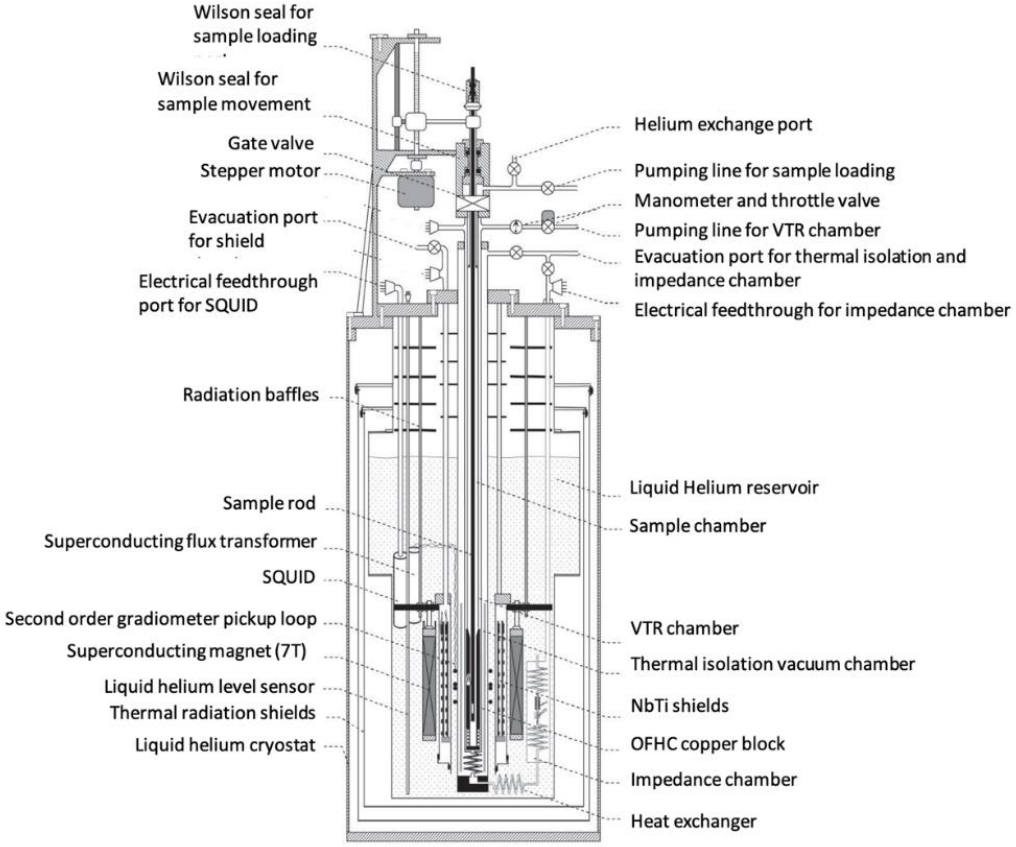

Figure 20: Detailed cross-sectional view of Cryogenic S700X SQUID Magnetometer. Adapted from [20].

Although this device has several modes of operation, the extraction method is the most commonly used. Hence, under an applied magnetic field, the sample moves vertically through the superconducting pickup coils. Consequently, this movement induces a current that is detected in the SQUID (Figure 21), producing an output voltage proportional to the magnetization of the sample. So, the signal is proportional to one magnetic flux quantum (Φ_0) (6), which is equal to 2.0678×10^{-15} T.m^2 [75].

$$\Phi_0 = \frac{2\pi\hbar}{2e} \qquad (6)$$

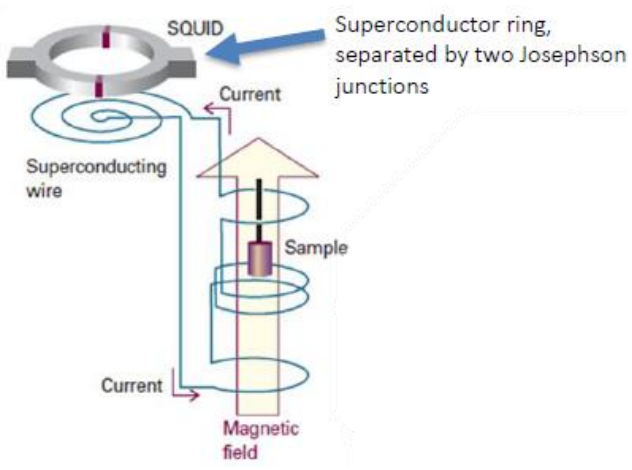

Figure 21: SQUID apparatus [75].

The SQUID device has two junctions in the superconducting ring (Figure 22), and its fundamental principle is based on the Josephson Effect. This effect consists in a supercurrent that can penetrate through a thin insulating barrier between two superconductors, called the Josephson junction. It is a quantum tunneling effect, which involves coherent tunneling of cooper pairs through the energy barrier [75].

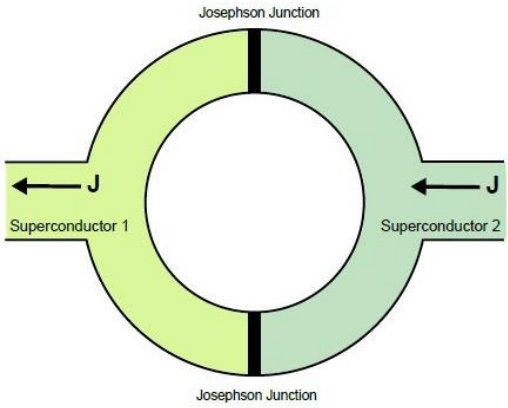

Figure 22: Josephson junction in the SQUID [75].

The S700X device has several advantages: an ultra-light design of the sample chamber that allows fast temperature changes and quick stability; any temperature within the wide range of 1.6 K to 400 K can be held continuously (assuming liquid helium remains in the main reservoir); mTesla field resolution; and fast sample change. Moreover, the sample exchange via airlock and cooling to 2K is possible in 10-15 minutes, and it has full environmental shielding (both magnetic and electromagnetic). In addition, it has

LabVIEW software that operates in an open environment, allowing the user direct control of all parts of the system with real-time graphical displays of all relevant functions [75].

To prepare a sample, each sample was weighed with approx. 10 mg in a transparent gelatin capsule to hold the sample that was placed in the SQUID to be measured. The capsule's top contains a hole to prevent it from bursting under pressure. Magnetic measurements of temperature, ZFC/FC [M(T)], and field dependence [M(H)] were taken.

3.3.6.1 Magnetization vs. Field

M(H) curves were taken at a temperature of 300 K and 10 K. These measurements were made to assess the saturation of magnetization (M_s). These measurements will allow us to analyze the variations of these properties for each SPIONs samples obtained from different synthesis processes and their further coatings and functionalization.

3.3.6.2 ZFC/FC

The samples were cooled from 300 K to 10 K in a zero magnetic field, then a static magnetic field of 2.5 mT for the Naked SPIONs and Dextran SPIONs and 50 mT for the gold coated and gadolinium functionalized ones was applied. The ZFC curve was measured while the samples were heating. The samples were once more cooled to 10 K while keeping the same field (FC procedure) after the last point was measured, and data was then measured for rising temperatures.

3.3.7 Magnetic Hyperthermia

Magnetic hyperthermia measurements were obtained using a DM100 series from *Nb Nanoscale Biomagnetics* apparatus. This apparatus allows measurements at different magnetic field intensities up to 300 Gauss with a frequency up to 418.5 kHz. These measurements were done in CENIMAT/I3N of FCT-UNL.

It was evaluated the heating ability of naked SPIONs (B01), coated with dextran (B02) and gold coated (B03) at a concentration of 1 mg/mL. Measurements were performed during 10 minutes by keeping magnetic field intensity of 300 Gauss and constant frequency of 388.15 kHz.

3.4 Cytotoxicity Assay

For the evaluation of the cytotoxic activity of the SPIONs a human prostate cancer cell line PC3 (ATCC, CRL-1435) was selected. The cell culture was prepared using RPMI-1640 (Roswell Park Memorial Institute Medium) supplemented with 10% fetal bovine serum (FBS) and 1% antibiotics. The cells were suspended in the medium, placed in culture flasks and incubated at 37ºC in the presence of CO_2 (5%). Upon confluence, the cells were removed by treatment with trypsin/EDTA solution, suspended with a complete medium and further diluted for cell counting or sub-culturing. The 3-(4,5-dimethylthiazol-2-yl)-2,5-diphenyl-2H-tetrazolium bromide (MTT) assay was used to evaluate the cellular viability. This assay is based on the reduction of the soluble yellow tetrazolium salt to insoluble purple formazan crystals by a succinate dehydrogenase enzyme, which is present in the mitochondria of metabolically active cells. For the assays, the cells were seeded into 96-cell plates at a density of 2 x 10^4 cells/200 µL (Figure 23a). After a period of 24 h for adherence, the cells were treated with 200 µL of different concentrations of A01, A04, B01 and B04 SPIONs in the range of 10 to 500 µg of Fe/mL (Figure 23b) and were incubated at 37 ºC for 24h in the presence of CO_2 (5%). After the incubation, the medium was aspirated and 200 µL MTT solution in PBS (0.5 mg/mL) was added to the cells. The latter were further incubated for another 3h under the same conditions. Finally, the formazan crystals were dissolved in 200 µL DMSO and the absorbance was measured with a microplate reader at 570 nm (Power Wave Xs, Bio-Tek, Winooski, VT, USA). The absorbance of the untreated cells was used as the control.

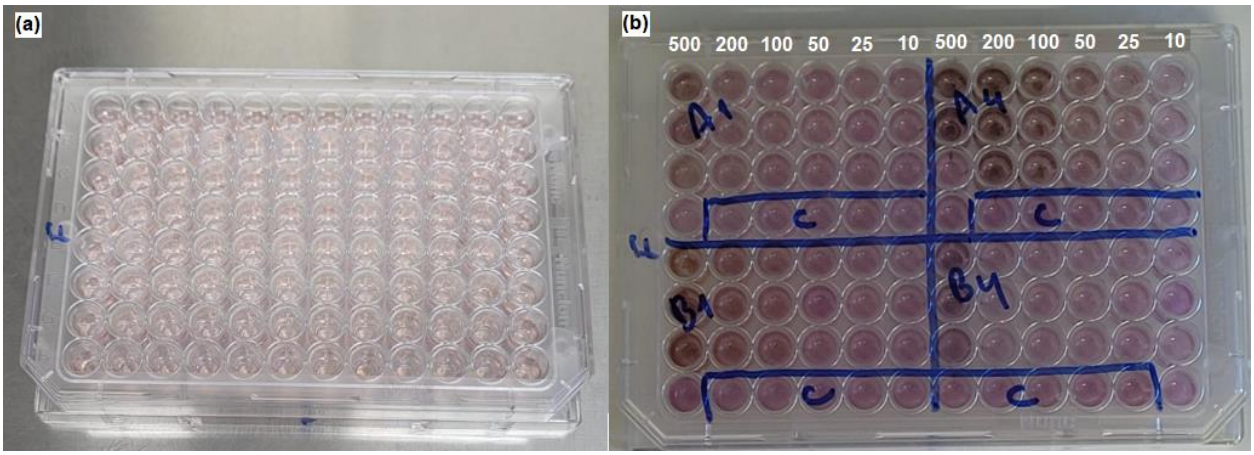

Figure 23: 96 cell plates seeded with PC3 cells (a), and cells treated with SPIONs in different concentrations in µg of Fe/mL (b). The cells designated with C letter are the control group.

Chapter 4

Results and Discussion

4.1 Structural Characterization

4.1.1 Powder X-Ray Diffraction

Powder X-ray diffraction measurements reveal structural information, phase, and approximate size of the crystalline core of the SPIONs. In the diffractograms for all A, B, and C samples, the diffraction pattern showed peaks at 2θ of approximately 18.50°, 30.31°, 35.72°, 43.40°, 53.80°, 57.35°, and 62.94°, consistent with nano-sized crystallites, allowing the identification of the main peaks of a spinel phase. The unit-cell parameters were estimated from the PowderCell program. From these parameters it was possible to infer that both magnetite, Fe_3O_4 (JCPDS file 19–629), and maghemite, $\gamma - Fe_2O_3$ (JCPDS file 39–1346), are present. Magnetite with ideal stoichiometry and maghemite. These two phases have the same crystalline planes for the main peaks but with slightly different intensity. This hinders the distinction between magnetite and maghemite with this technique. However, these two compounds can be distinguished by using another characterization technique, the Mössbauer spectroscopy, which allows to identify Fe-containing phases and their oxidation state, Fe^{2+} and Fe^{3+} (see below in this section).

The represented crystal planes are (111), (220), (311), (400), (422), (511) and (440). Figure 24 shows the comparison between the diffractograms of naked SPIONs (A01, B01).

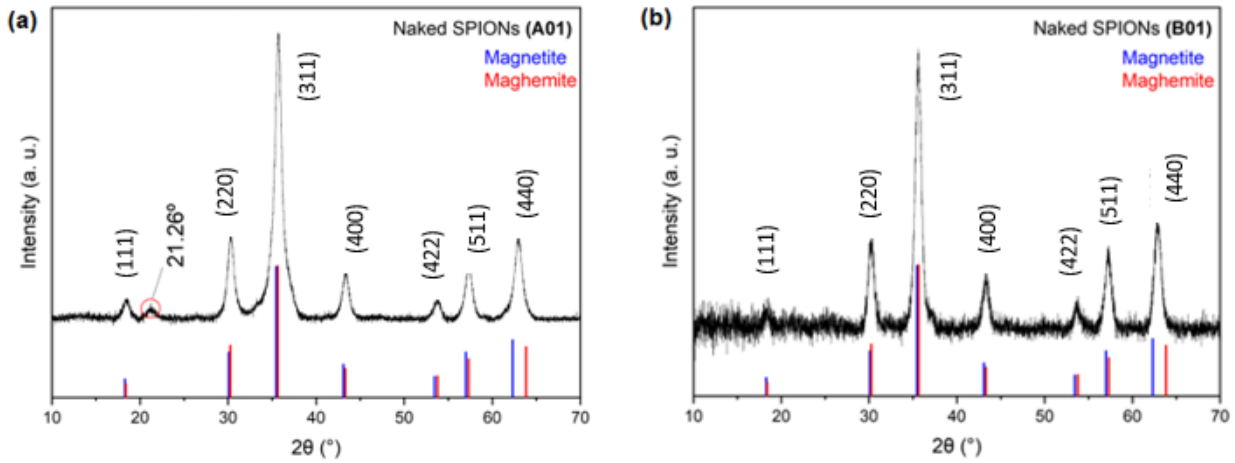

Figure 24: Left: Powder diffractogram of A01 (a). Left: Powder diffractogram of B01 (b).

For A01 it is possible to observe a peak at 21.26º (Circulated in red) that is neither part of the magnetite nor of the maghemite. Through literature searches and analysis with the software DIFRACC.EVA it is possible to attest that this peak refers to a slightly presence of goethite that is an Iron (III) oxide -

Hydroxide (α - FeO(OH)) [76]. The presence of this phase could, probably, have been avoided by a more effective washing of the samples, removing all excess hydroxides.

Figure 25 shows the diffractogram of the Naked SPIONs C01 sample. In this case, the appearance of an ammonium chloride (NH_4Cl) salt phase is present. The main peaks of this salt that are represented in the diffractogram are 23.05°, 32.76°, 40.39°, 46.94°, 52.86°, 58.31°, which are very close to those in the literature (JCPDS file 73-1491) [77]. The presence of this salt comes probably from the non-washing of SPIONs C in the synthesis step. In addition, it is possible to observe non-main peaks (circled in red) which suggest the presence of maghemite. This fact may reveal that this sample has a higher amount of maghemite when compared to the naked SPIONS A01 and B01 since the diffractograms for those samples do not show these non-main maghemite peaks.

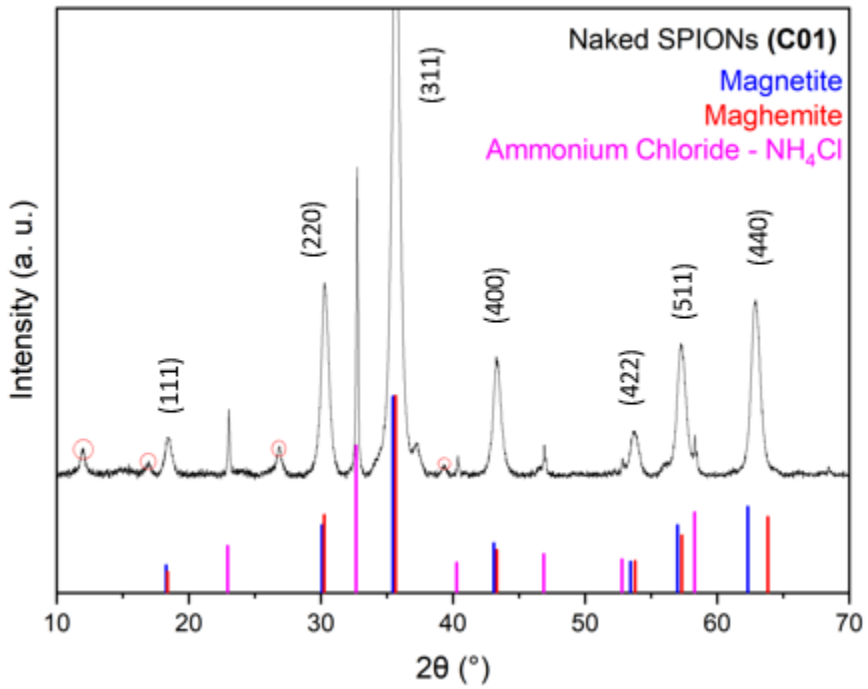

Figure 25: Powder diffractogram of C01 sample.

The powder diffractograms for A02 and B02 samples (Figure 26) show that the coating process with dextran and dextran NH_2 did not affect the crystal structure of the SPIONs core since no differences between the diffractograms were found. It is not possible to confirm the presence of dextran through this technique because it is an amorphous compound.

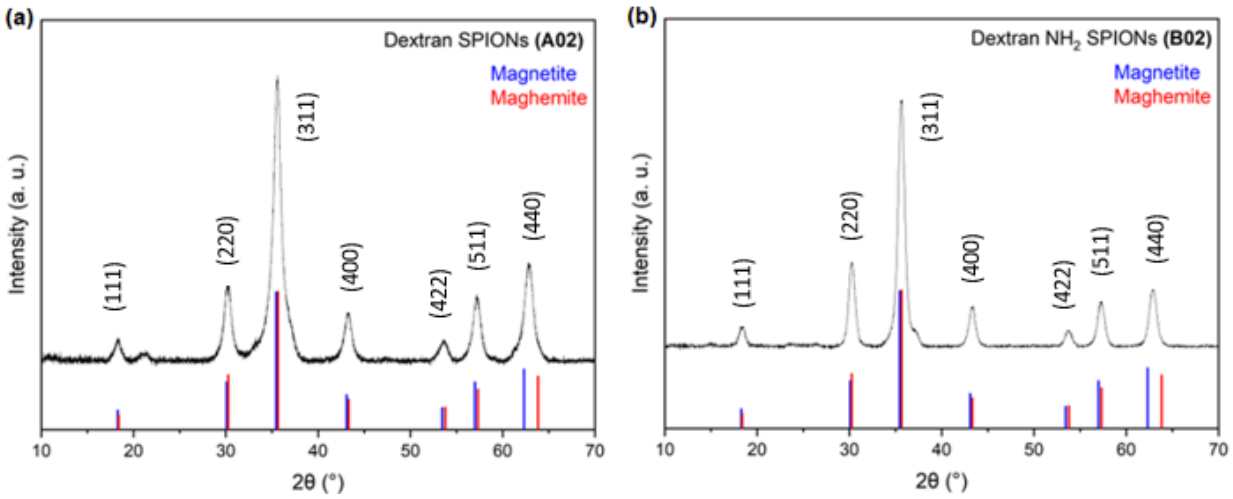

Figure 26: Left: Powder Diffractogram of A02 (a). Left: Powder Diffractogram of B02 (b).

The X-ray diffraction measurements for A04 and B04 showed peaks at 2θ for the gold phase at, approximately, 38.15º, 44.32º, 64.56º, 77.53º. Comparing with the JCPDS card for gold (Au^0) (JCPDS 04-0784), it is observed that the samples have peaks corresponding to this FCC structure, representing the crystal planes (111), (200), (220), and (311). Figure 27 shows the diffractograms of both A04 and B04 samples.

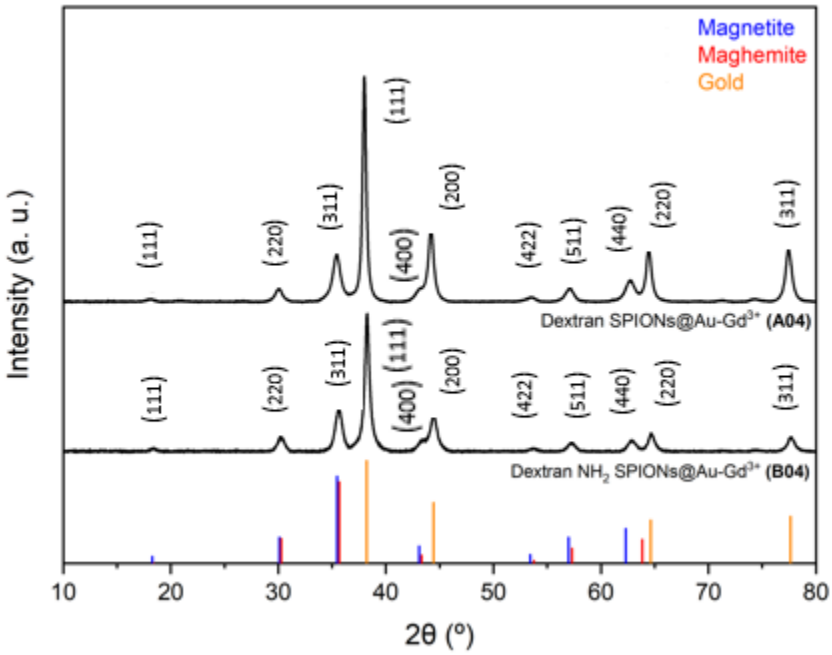

Figure 27: Comparison between diffractograms of A04 and B04 samples.

Using the 3 main peaks from the PXRD data of the samples, the crystallite size (D_{XRD}) of the iron core of each sample was evaluated by using Debye Scherrer's equation (7) [79]:

$$D_{XRD} = \frac{K\lambda}{\beta Cos(\theta)} \quad (7)$$

where K is the Scherrer constant equal to 0.9 for spherical particles, λ is the X-ray wavelength of λ=1.54Å, β is the full width at half maximum (FWHM) in radian, and θ is the Bragg angle of the peak position in radians. The crystallite sizes estimated for the different samples ranged between 7.78 and 10.55 nm and are arranged in Table 3.

Table 3: Crystallite sizes estimated by Powder X-Ray Diffraction.

Sample	Crystallite Size - D_{XRD} (nm)
A01	9.04
A02	7.38
A03	9.81
A04	9.40
B01	9.84
B02	9.60
B03	10.55
B04	9.76
C01	9.98

Even though the samples have more percentage of iron than gold, the peaks for gold are more intense due to the high absorption of radiation by the gold nanoparticles [78], causing the iron oxide peaks to be somewhat faded.

By this technique, it is not possible to confirm if gadolinium is present in samples A04 and B04, because it is in ionic form (Gd^{3+}) complexed by the chelator agent TDOTA. In order to fully identify all the metals present in these samples ICP-MS measurements were undertaken for samples A01, A04, B01 and B04. These results are shown in the Table 4 below.

Table 4: Concentration of the elements iron, gold, and gadolinium in each sample (A01, B01, A04, and B04) obtained by ICP-MS.

	Concentrations						
Samples	**Fe** $(\mu mol/mg)$	**Fe (%)**	**Au** $(\mu mol/mg)$	**Au (%)**	**Gd** $(\mu mol/mg)$	**Gd (%)**	**Others (%)**
A01	16.1160	90.000	-	-	-	-	10.000
B01	14.4510	80.769	-	-	-	-	19.231
A04	9.4798	52.941	2.2400	44.118	0.0262	0.410	2.531
B04	9.5502	53.333	2.2000	43.333	0.0110	0.173	3.160

With these results, one can confirm that gadolinium is present in samples A04 and B04 in amounts of 0.410 and 0.173% of these samples, respectively. In addition, with the amount of gold and iron also obtained, it was possible to evaluate the proportion between these two elements in mol obtained after synthesis. These results suggest that samples A03 and B03 were coated with gold in a mol ratio of approximately 4Fe:1Au as shown in Table 5

Table 5: Molar ratio between Fe and Au for A04 and B04.

Samples	Fe:Au (mol)
A04	4.23 : 1
B04	4.34 : 1

4.1.2 Mössbauer Spectroscopy

As confirmed by the Mössbauer spectroscopy technique performed for samples A01, A02, A03, B01, and B03, the magnetite present in those samples is partially oxidized. There is no reason to believe that all the spinel grains have exactly the same oxidation degree. Most probably magnetite grains with different oxidation degrees up to the maghemite limit where all the Fe cations are in the 3+ oxidation state, are present in the studied samples leading to a mixture of spinel grains with different unit-cell parameters. This further broadens the PXRD peaks, in addition to the small grain size effect.

The Mössbauer spectra at RT, showing sextets with very broad peaks, as well as an additional doublet, are consistent with superparamagnetic iron oxides. These spectral features arise when crystallites are nanosized and consist of single magnetic domain particles. They are so small (less than 13 nm or 10 nm, for interacting γ – Fe_2O_3 and Fe_3O_4 NPs) that thermally induced energy fluctuations change the direction of the magnetization of the NPs from one easy axis to another with a frequency higher than the Larmor precession frequency of the nuclear magnetic moment in the local field [80]. If NPs with a finite range of volumes are present, they will give rise to a superposition of spectra with different relaxation times.

Decreasing the temperature to 4K slows down the relaxation of the direction of the magnetic moments and allows the observation of sharp peaks (Figure 28 and Figure 29). The 4 K spectra, nevertheless, cannot be fitted by a single magnetic sextet. Three sextets are necessary to analyze adequately the spectra. The estimated parameters (Table 6 and Table 7) suggest that two sextets are due to tetrahedrally and octahedrally coordinated Fe^{3+} in maghemite and magnetite [20,81] and the third sextet with higher isomer shift is consistent with Fe^{2+} in magnetite [20, 83].

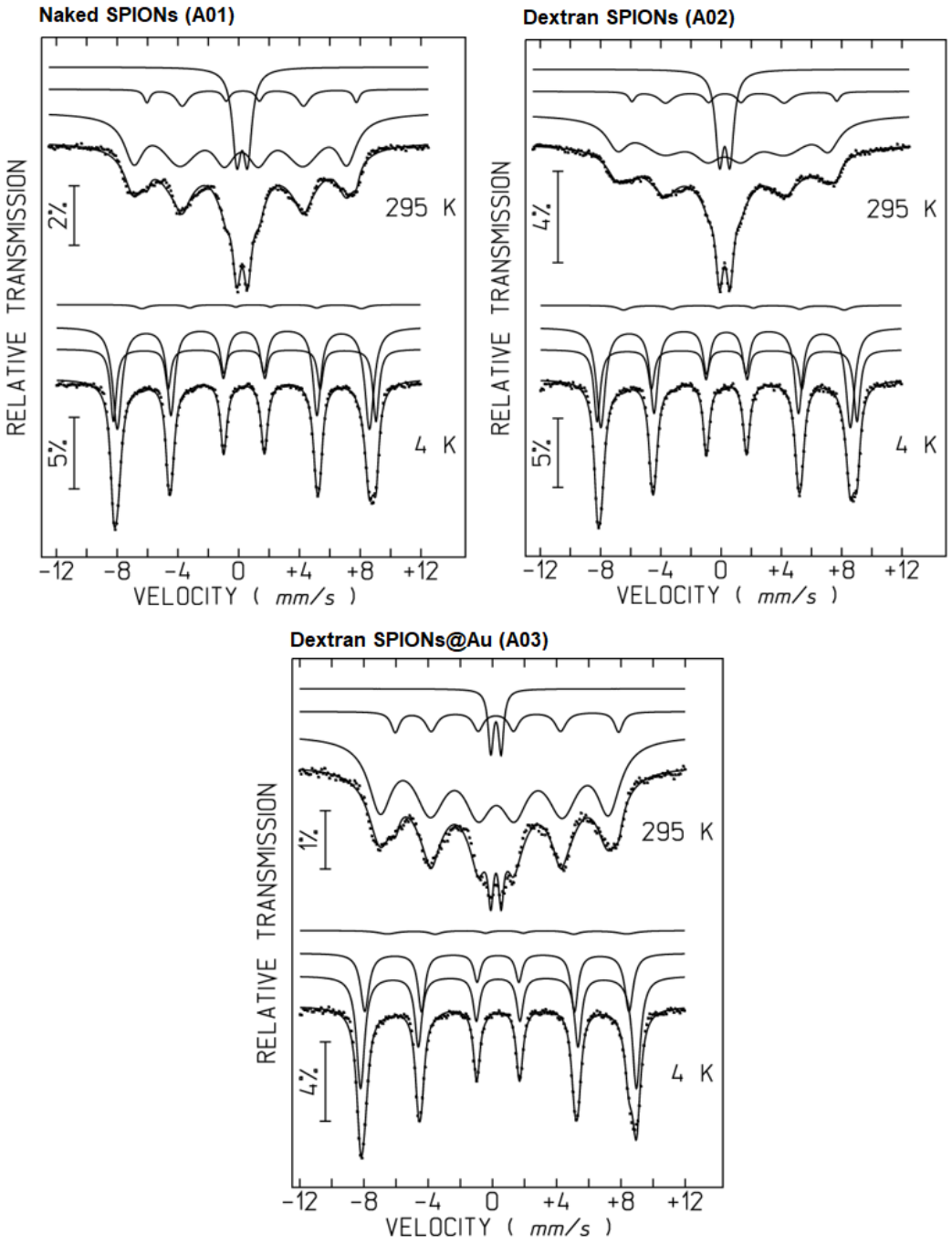

Figure 28: Mössbauer spectra of A01, A02, and A03 samples taken at different temperatures. The lines over the experimental points on the spectra taken at 295 K are the sum of a magnetic field distribution and a quadrupole doublet and on the spectra taken at 4 K the sum of three sextets, shown slightly shifted for clarity. The estimated parameters for these sextets are collected in Table 6.

Table 6: Estimated parameters from the Mössbauer spectra taken at 295 K and 4 K for A01, A02, and A03 samples.

Samples	Oxidation state - Site	IS	QS	B_{hf}	I (%)	
A01						
295 K	Fe^{3+}	0.30	-0.12	43.5	76%	
	Fe^{3+}	0.35	0.65	-	16%	
	$Fe^{2.5+}$	0.69	0.66	42.7	8%	
4 K	Fe^{3+} octahedral	0.48	0.02	53.1	57%	**11% Fe in magnetite**
	Fe^{3+} tetrahedral	0.43	-0.07	50.9	39%	
	Fe^{2+} octahedral	0.93	-0.10	46.4	3.8%	
A02						
295 K	Fe^{3+}	0.29	-0.09	43.4	75%	
	Fe^{3+}	0.35	0.69	-	17%	
	$Fe^{2.5+}$	0.68	0.63	42.1	8%	
4 K	Fe^{3+} octahedral	0.48	0.01	53.0	58%	**11% Fe in magnetite**
	Fe^{3+} tetrahedral	0.42	-0.08	50.9	38%	
	Fe^{2+} octahedral	0.93	-0.45	46.8	3.8%	
A03						
295 K	Fe^{3+}	0.29	-0.12	44.1	86%	
	Fe^{3+}	0.33	0.64	-	5%	
	$Fe^{2.5+}$	0.67	0.69	43.1	9%	
4 K	Fe^{3+} octahedral	0.48	0.02	53.3	58%	**13% Fe in magnetite**
	Fe^{3+} tetrahedral	0.43	-0.07	51.0	38%	
	Fe^{2+} octahedral	0.94	0.23	46.5	4.4%	

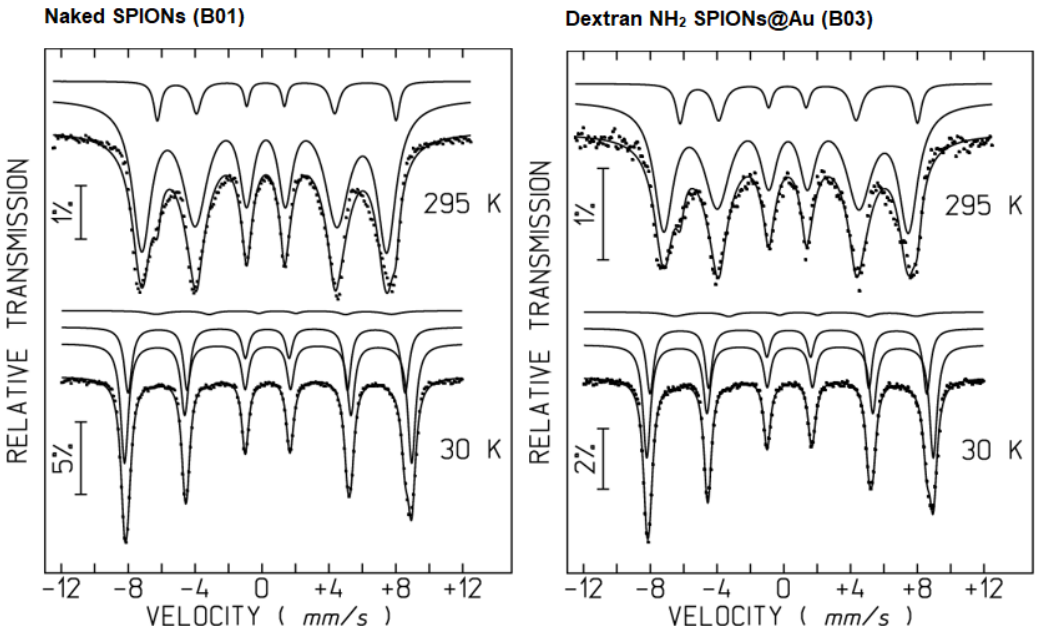

Figure 29: Mössbauer spectra of B01 and B03 samples taken at different temperatures. The lines over the experimental points on the spectra taken at 295 K are the sum of a magnetic field distribution and a quadrupole doublet and on the spectra taken at 4 K the sum of three sextets, shown slightly shifted for clarity. The estimated parameters for these sextets, are collected in Table 7.

Table 7: Estimated parameters from the Mössbauer spectra taken at 295 K and 4 K for B01 and B03 samples.

Samples	Oxidation state - Site	IS	QS	B_{hf}	I (%)	
B01						
295 K	Fe^{3+}	0.30	-0.11	45.4	91%	
	Fe^{3+}	0.66	0.66	44.2	9%	
4 K	Fe^{3+} octahedral	0.47	0.02	53.2	58%	**13% Fe in magnetite**
	Fe^{3+} tetrahedral	0.41	-0.04	51.4	38%	
	Fe^{2+} octahedral	0.93	-0.21	43.7	4.5%	
B03						
295 K	Fe^{3+}	0.30	-0.12	45.4	89%	
	Fe^{3+}	0.68	0.66	44.1	11%	
4 K	Fe^{3+} octahedral	0.49	0.01	53.2	57%	**17% Fe in magnetite**
	Fe^{3+} tetrahedral	0.40	-0.02	51.4	37%	
	Fe^{2+} octahedral	0.92	-0.17	44.6	5.6%	

The room temperature spectra may be fitted with distributions of magnetic hyperfine fields (B_{hf}), in order to simulate the magnetic relaxation signals, and a quadrupole doublet which corresponds to the particles with the fastest magnetic relaxation [20, 84].

No structural information may be obtained in addition to that deduced from the 4 K spectra. A reasonable fit may be obtained assuming isomer shifts (IS) consistent with high-spin Fe^{3+} and $Fe^{2.5+}$ and leading to results consistent with those obtained for the 4 K spectrum.

Comparing the 295 K spectra one concludes that A01 and A02 samples have a higher fraction of particles with faster relaxation than A03 which may be due in the latter sample to lower interparticle magnetic interactions or to a lower fraction of smaller nanoparticles.

Assuming the unlikely scenario where there are only particles of maghemite and of magnetite with the ideal stoichiometry in the sample, the fraction of Fe in magnetite could be deduced from the relative areas of Fe^{2+} at 4 K. For instance in B03 approximately 17% of Fe is present in magnetite: 5.6% Fe^{2+} (Table 7), plus 5.6% Fe^{3+} on the octahedral sites, plus 5.6% Fe^{3+} on the tetrahedral sites. For A01 and A02 approximately 11% of Fe is present in magnetite: 3.8% Fe^{2+} (Table 6), plus 3.8% Fe^{3+} on the octahedral sites, plus 3.8% Fe^{3+} on the tetrahedral sites. The difference between the estimated relative areas of Fe^{2+} at 4 K for this last example is within experimental error but it points to a slightly higher magnetite content in A03. However it is more realistic to consider that the sample consists of particles with different oxidation degrees [84] and the estimated fractions of Fe^{2+} and Fe^{3+} are the average values over all the nanosized particles in the sample.

4.1.3 Transmission Electronic Microscopy (TEM)

The transmission electron microscopy (TEM) technique was used to evaluate the size, shape, and size dispersion (σ) of the produced SPIONs, with this last obtained through the equation (8) shown below.

$$\sigma\ (\%) = \frac{Standard\ Deviation}{Average\ NPs\ size} \times 100 \qquad (8)$$

The average nanoparticle size (D_{TEM}) was calculated from the TEM images shown in this section, using the Image-J program. From the obtained values, the histograms presented were constructed using sample sizes (N) of 100 and 200.

It was possible to obtain images for all samples during the development of the work. For A01 (Figure 30a) nanoparticles have a D_{TEM} of 10.02 ± 2.10 nm, a mixture of spherical and cubic shapes and some

undefined shapes and a σ of 20,94%. As shown in the image, the nanoparticles may remain close to each other, but without showing aggregation. For the sample with Dx (A02) (Figure 30b), this is even more clear due to the stabilization that the polymer provides when surrounded on the nanoparticles. These nanoparticles have a mixed shape, between spherical and undefined, and have a lower D_{TEM} of 6.60 ± 1.82 nm with σ = 27.58%.

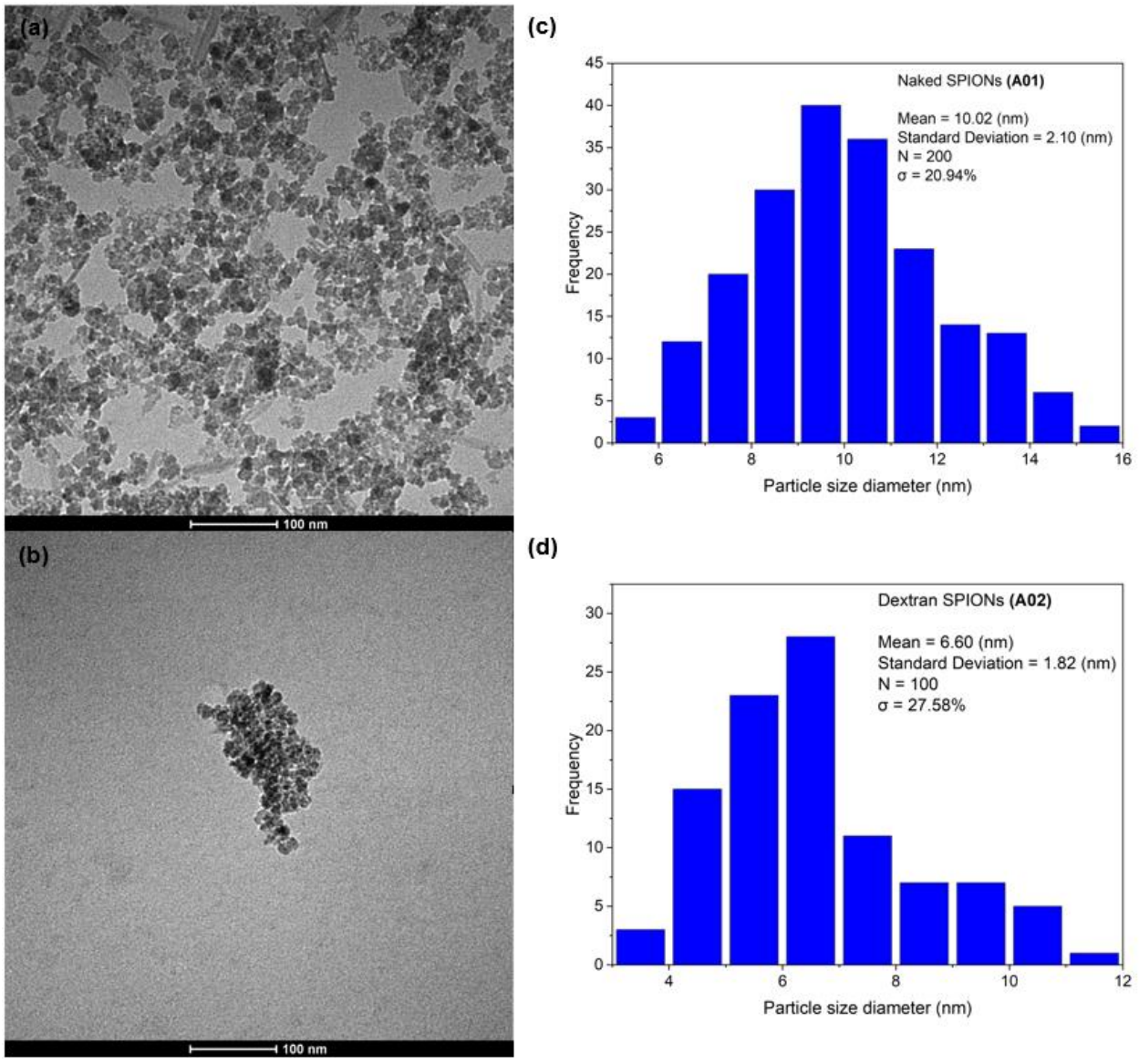

Figure 30: Left: TEM images at 100 nm scale for A01 (a) and A02 (b) samples. Right: nanoparticle´s size histograms obtained by TEM for A01 (c) and A02 (d).

The gold coated A03 sample (Figure 31a) show dimensions of D_{TEM} = 10.91 ± 2.71 nm and σ = 24.84%. Functionalized SPIONs A04 (Figure 31b), shows a slight increase on their size but the way that

they are arranged are pretty much the same as on A03 sample. A04 presented D_{TEM} = 11.34 ± 2.75 nm and σ = 24.22%.

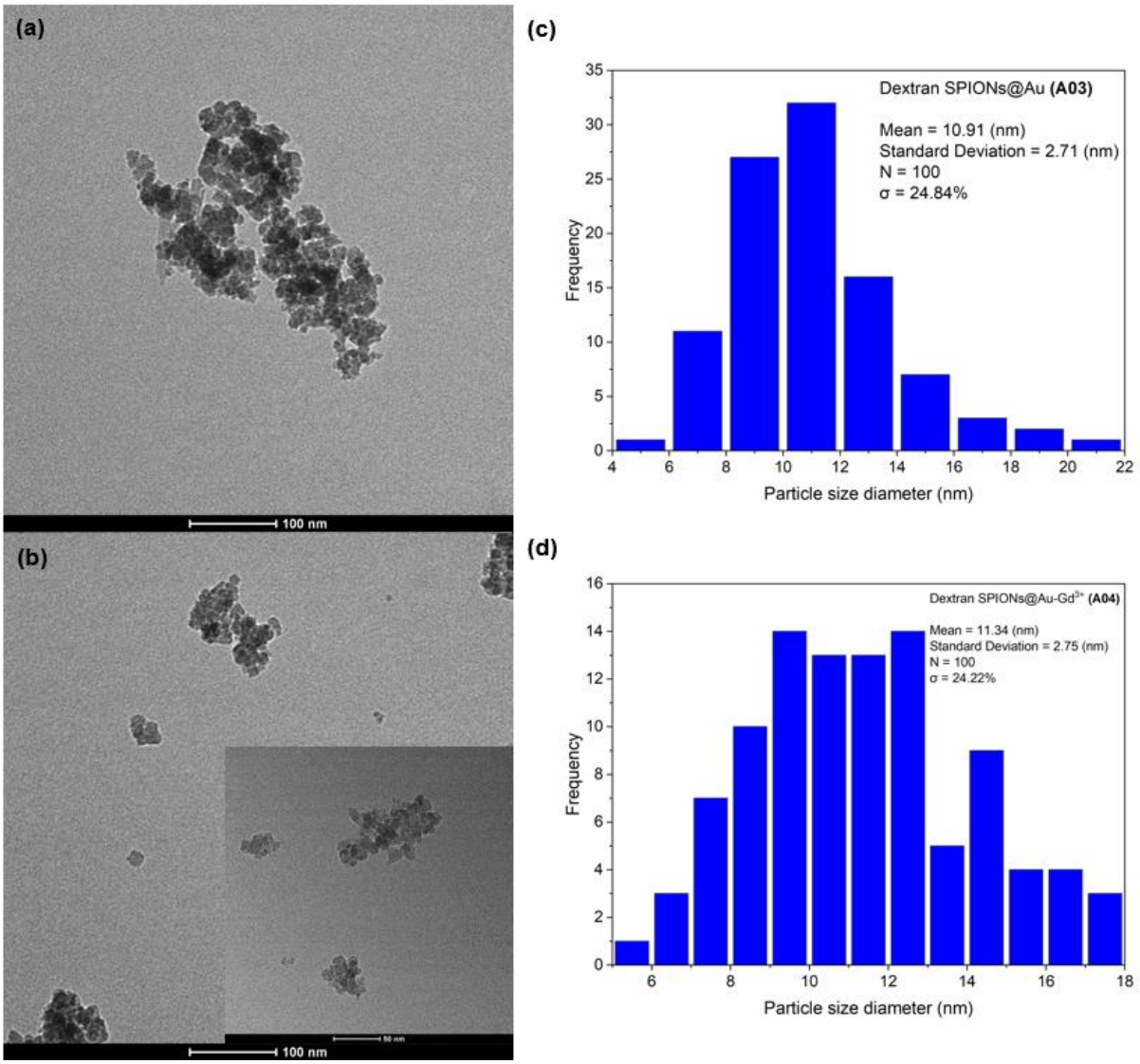

Figure 31: Left: TEM images at 100 nm scale for A03 (a) and A04 (b) samples. Inset detail with scale of 50nm. Right: nanoparticle´s size histograms obtained by TEM for A03 (c) and A04 (d).

As attested by the PXRD technique, sample A01 has a peak related to goethite, an iron oxide-hydroxide. Through TEM images, it was possible to confirm its presence as shown by the long crystals next to the nanoparticles, which are goethite as shown in Figure 32. The presence of goethite is a problem when it is predominant in the sample, because it has a shape that is not favorable for biomedical applications, since the hydroxide groups are non-biocompatible. In addition, it has a lower magnetization degree than magnetite or maghemite.

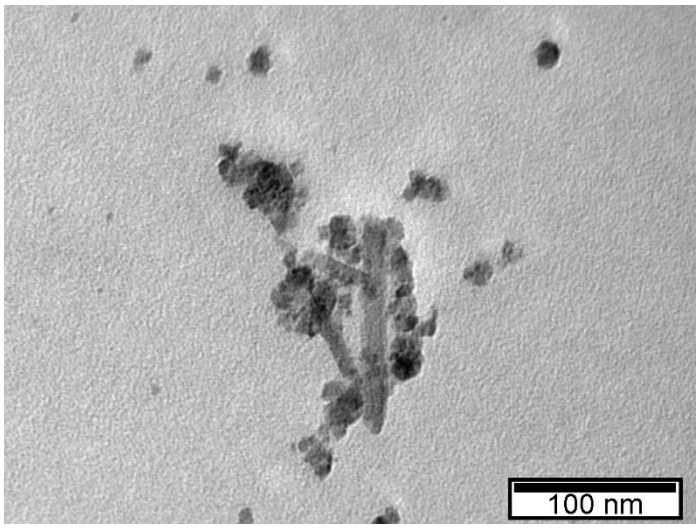

Figure 32: TEM image of A01 sample showing some needles that can be presence of goethite phase in the sample.

For B01 (Figure 33a) nanoparticles have a D_{TEM} of 9.85 ± 1.97 nm, with predominantly spherical morphology and a σ of 19,98% and quite separated since their edge can be distinguished. For B02 (Figure 33b), and in contrast to A02, the nanoparticles are not reduced in diameter. These nanoparticles have a spherical-like shape with a D_{TEM} of 9.76 ± 2.12 nm and σ = 21.74%.

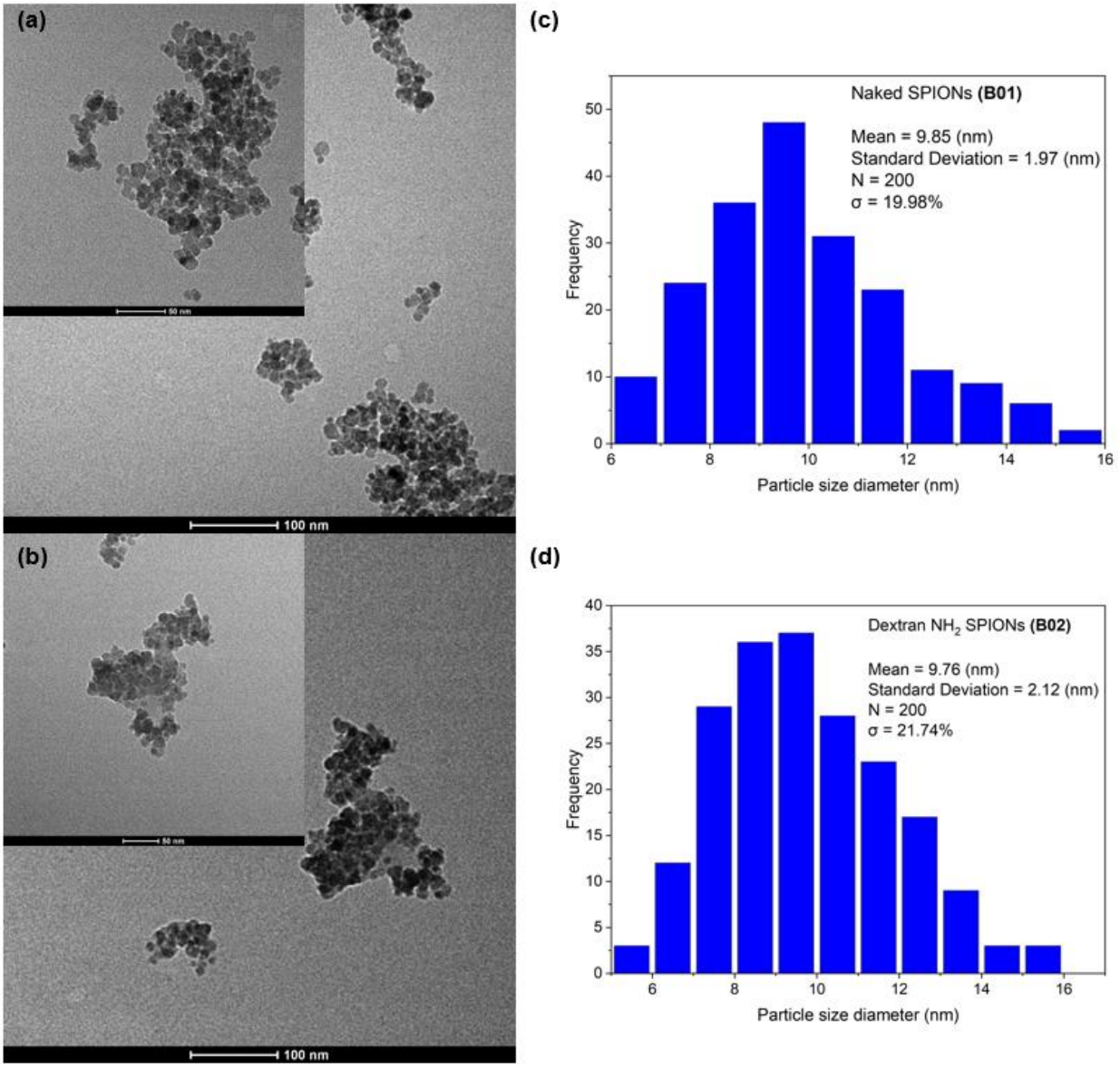

Figure 33: Left: TEM images at 100 nm scale for B01 (a) and B02 (b) samples. Inset detail with scale of 50nm. Right: nanoparticle´s size histograms obtained by TEM for B01 (c) and B02 (d).

The gold coated B03 sample (Figure 34a) show dimensions of D_{TEM} = 10.00 ± 2.27 nm and σ = 22.66%. In functionalized SPIONs B04 (Figure 34b) there are some spots with large clumps, but this is probably due to precipitation that occurred during the sample preparation stage, because it is noticeable that in other regions NPs are very well dispersed, unlike A04 sample. In the inset of the figure, one can observe how clearly separated from each other they are. This result is very promising for this work since the better dispersed they are, the better for biomedical applications we are targeting. A04 presented D_{TEM} = 11.02 ± 2.21 nm and σ = 20.03%.

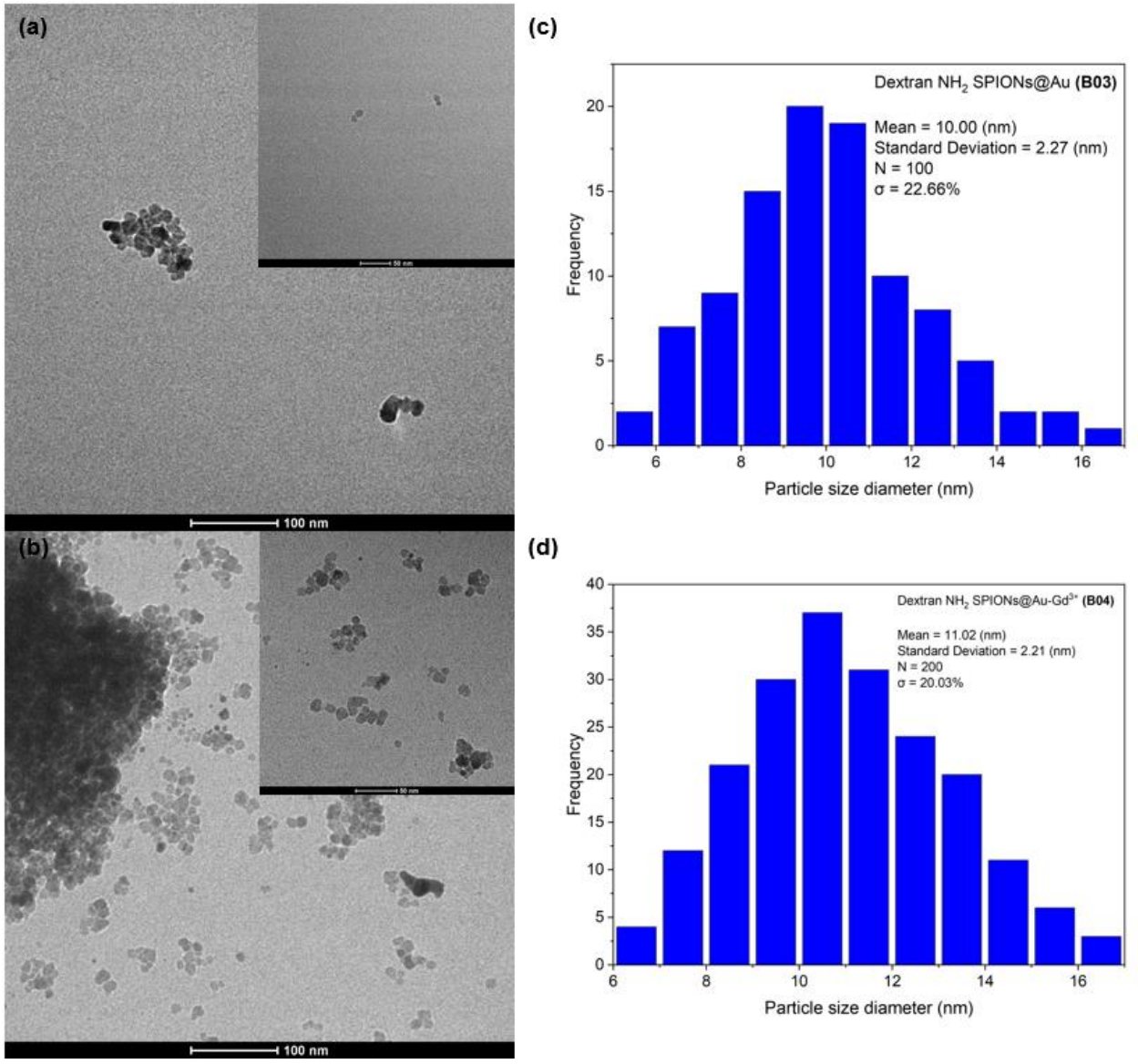

Figure 34: Left: TEM images at 100 nm scale for B03 (a) and B04 (b) samples. Inset detail with scale of 50nm. Right: nanoparticle´s size histograms obtained by TEM for B03 (c) and B04 (d).

The TEM images for SPIONs C01 (Figure 35) showed good results with a size dispersion of 20.8%, a well-defined spherical shape with a few variations, and a D_{TEM} of 8.30 ± 1.73 nm. In addition, they are well dispersed better than A or B samples. Larger nanoparticles are found to closer but not aggregated, which may be due to long range magnetic dipole-dipole interaction between the nanoparticles [85]. As attested by the powder PXRD technique, some peaks are related to the structure of ammonium chloride, which cannot be seen in this image.

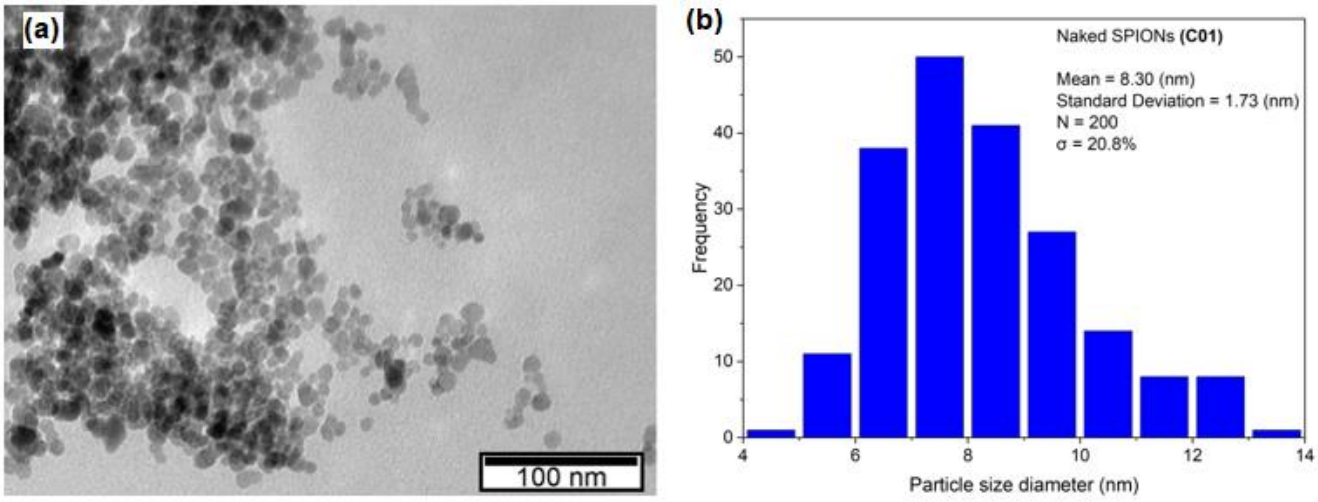

Figure 35: Left: TEM image at 100 nm scale for C01 (a) sample. Right: nanoparticle´s size histogram obtained by TEM for C01 (b).

The average size values calculated by TEM corroborate the calculations performed previously using PXRD (D_{XRD}), indicating that the nanoparticles are mainly single crystallites [85], and are shown in Table 8. Furthermore, all values of sizes are consistent with those found in others researches that SPIONs are being used for MRI and magnetic hyperthermia [86–89]

Table 8: Crystallite size obtained by PXRD and particle size obtained by TEM images for each sample.

Sample	Crystallite Size - D_{XRD} (nm)	Particle size - D_{TEM} (nm)
A01	9.04	10.02 ± 2.10
A02	7.38	6.60 ± 1.82
A03	9.81	10.91 ± 2.71
A04	9.40	11.34 ± 2.75
B01	9.84	9.85 ± 1.97
B02	9.60	9.76 ± 2.12
B03	10.55	10.00 ± 2.27
B04	9.76	11.02 ± 2.21
C01	9.98	8.30 ± 1.73

4.1.4 Zeta Potential

When particles interact, two forces must be considered, van der Waals and electrostatic repulsion. Based on these interactions, the zeta potential (ζ) is calculated as the ratio between the speed at which the particles move in suspension and the electric field applied at the time of measurement. This technique measures the electrostatic potential at the boundary of the compact layer and the diffuse layer of the colloidal particles, demonstrating the degree of stability of the suspension [90]. In absolute value, the higher the zeta potential, the greater the repulsion between the particles, so they tend to become dispersed. If the zeta potential is close to 0 mV they tend to agglomerate [91].

As reported in the literature, it is a general rule that good particle stability has zeta potential values above 30mV or below -30mV. Values around 5mV indicate a fast aggregation of the particles [92].

Zeta values determined for all samples are presented in Table 9. Naked samples A01 and C01 obtained ζ of 40.3 ± 8.1 and 43.80 ± 9.7 mV, respectively. This indicates good stability and dispersion of the particles as also confirmed from the TEM analyses. For C01 the ζ value is due to the fact that sample was not washed, causing a large amount of NH_4^+ and Cl^- ions from the synthesis to be adsorbed on the surface of the SPIONs. As shown by PXRD, C01 has peaks related to ammonium chloride NH_4Cl. The high positive value of the zeta potential of A01 can also be attributed to the adsorption of Na^+ and NH_4^+ ions on the surface of the SPIONs aggregates due to an inefficient washing. For sample B01, a zeta potential of -13.13 ± 6.1 mV was determined, which reveals a low stability and less dispersion. This may be due to a more efficient washing process by magnetic separation in removing adsorbed positive ions from the SPIONs, possibly leaving only adsorbed Cl^- ions, and consequently making this potential to be negative.

The addition of Dx and Dx-NH2 in A02 and B02, respectively, implies a change of the ζ. Negative OH^- groups from the dextran and sodium hydroxide OH^- groups that replaces the other adsorbed ions at the SPIONs surface, cause the ζ in A01 to decrease to a value of -6.21 ± 7.6 mV, indicating instability and lower dispersion of the suspension. On the contrary, for B02, where Dx - NH2 was used, which has a much more positive character due to the amino group present in it, the zeta potential increased and became positive (47.83 ± 8.1 mV), indicating good stability and dispersion. The addition of the gold layer seems to have no effect on the ζ values.

The functionalization with TDOTA complexed Gd^{3+} increased the zeta potential from A03 to A04 (35.35 ± 8.5 mV), which may indicate a stabilization of the nanoparticles at lower pH [93]. The values of zeta potential for B04 (44.80 ± 9.1 mV) are in agreement with the TEM analysis of this sample (Figure 34b), showing good dispersion of the nanoparticles.

4.1.5 Dynamic Light Scattering (DLS)

The DLS technique correlates the Brownian motion of the particles in a colloidal suspension with the hydrodynamic size (D_H) of the analyzed material. Therefore, to obtain the size it is necessary to analyze the motion of these particles over a certain time. Particles with smaller hydrodynamic sizes diffuse rapidly due to the rapid Brownian motion in solution. However, when the hydrodynamic sizes are larger, the movements are slower, leading to a decrease in Brownian motion [94].

The difference in the size determination of nanoparticles by PXRD (D_{XRD}) and TEM (D_{TEM}), and the mean hydrodynamic size obtained by DLS (D_H), is due to the hydrodynamic radius, a hydration layer related to the electrical double layer of the nanoparticles. The presence of dextran in A02 can be attested due to the large increase in D_H from A01 (108.95 nm) to A02 (352.40 nm). As A02 is composed of small clusters this hydrodynamic size may refer to the whole cluster and not just to a single nanoparticle as shown in Figure 36. In addition, since SPIONs are magnetic, they were attracted by the electrode of the cuvette during the tests, which may have provided inaccurate measurements using this technique.

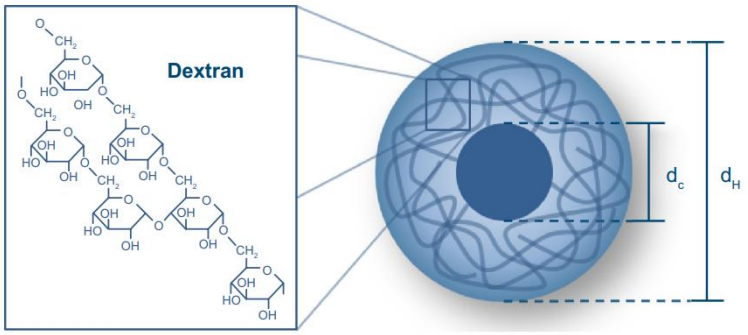

Figure 36: Diameter of magnetic core (d_c) is surrounded by a magnetically neutral coating (Dextran) (with hydrodynamic diameter d_H). Adapted from [95].

The decrease of D_H when samples are coated with gold nanoparticles (A03 and B03) is due to a compression of the gold against the D_H direction. For nanoparticles functionalized with TDOTA complexed Gd^{3+} (A04 and B04), the $-NH_2$ and $-(OH_2)^+$ groups from TDOTA complex the gadolinium inside and outside making a shell around the nanoparticles or nanoparticles aggregates, also reducing its D_H. The Table 9 below shows a comparison of the diameters obtained by PXRD, TEM and DLS analyses, as well as the values obtained for the zeta potential of each sample.

Table 9: Measurements of sizes obtained by PXRD, TEM and DLS and zeta potential of all samples.

Sample	Crystallite Size D_{XRD} (nm)	Particle size D_{TEM} (nm)	Hydrodynamic Size D_H (nm) (PDI)	Zeta Potential (mV)
A01	9.04	10.02 ± 2.1	108.95 (0.482)	40.30 ± 8.1
A02	7.79	6.60 ± 1.8	352.40 (0.373)	-6.21 ± 7.6
A03	9.81	10.91 ± 2.7	223.64 (0.536)	-1.91 ± 6.0
A04	9.40	11.34 ± 2.8	133.80 (0.490)	35.35 ± 8.5
B01	9.84	9.85 ± 1.9	84.02 (0.357)	-13.13 ± 6.1
B02	9.60	9.76 ± 2.1	118.80 (0.484)	47.83 ± 8.1
B03	10.55	10.00 ± 2.2	87.80 (0.731)	47.01 ± 7.0
B04	9.76	11.02 ± 2.2	44.70 (0.511)	44.80 ± 9.1
C01	9.98	8.30 ± 1.7	19.00 (0.537)	43.80 ± 9.7

4.2 Magnetic Characterizations

The magnetic properties of all the nanoparticles samples were performed by means of static (DC) magnetization measuring the hysteresis loops and the thermal dependence of the magnetization after field-cooling (FC) and zero-field-cooling (ZFC). In general, the field dependence of the magnetization curves taken at room temperature, 300 K, showed no hysteresis, with coercivity (Hc) approximately 0, which is indicative of the superparamagnetic behavior required. Moreover, upon removal of the applied magnetic field, the SPIONs retain no residual magnetism at room temperature, which is a good advantage for their use in theranostic, since they do not have tendency to agglomerate, thus enabling the uptake by the tumor cells. The saturation magnetization (M_s) values varied between 51,00 and 66.60 Am^2/Kg for the naked samples (A01, B01, and C01), which are in agreement with other reported works of synthesized SPIONs through co-precipitation method [96–98]. B01 achieved the highest M_s value of 66 Am^2/Kg, validating the synthesis method B as the one that provided SPIONs with the best magnetic performance so far. This fact can be due to a slightly larger amount of magnetite in B01 has when compared to A01, which also increase its saturation magnetization value. At lower temperatures, i.e., 10 K, the nanoparticles present a higher value of saturation magnetization, and it is necessary to apply a coercive field to reach a magnetization of zero, meaning that at this temperature the nanoparticles exhibit hysteresis and behave as ferromagnets.

Figure 37a shows the M(B) curves obtained for A01, B01 and C01 at 300 K while Figure 37b shows the superparamagnetic behavior at 300K and the ferromagnetic behavior at 10 K for each sample.

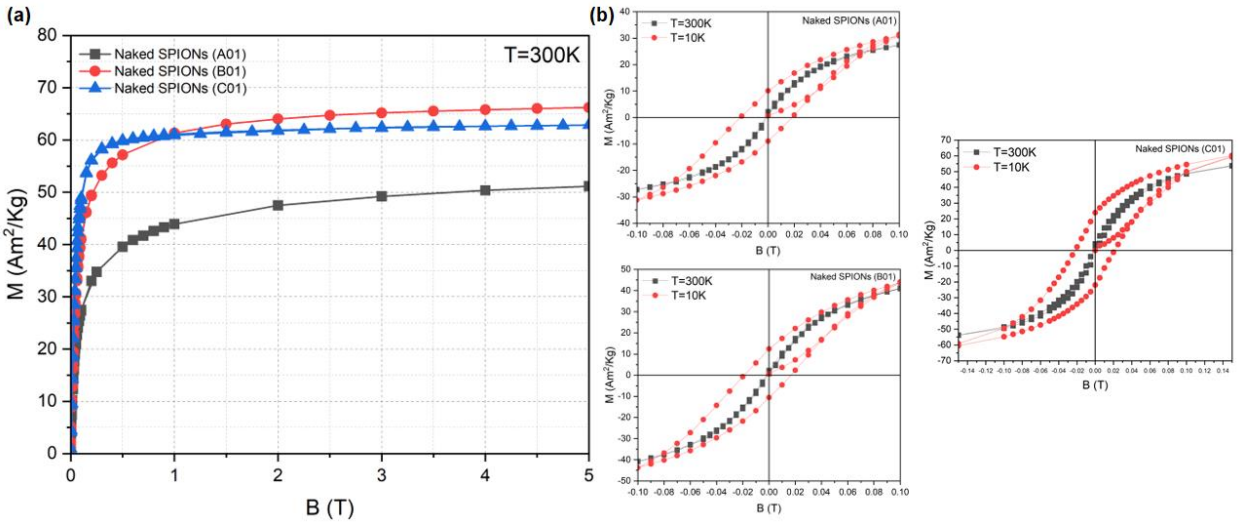

Figure 37: (a) Field dependence of the magnetization for A01, B01, and C01. (b) Hysteresis curves showing superparamagnetic behavior at 300K and ferromagnetic behavior at 10K for samples A01, B01, and C01.

Figure 38 shows on the left side all the M(B) curves for A samples and on the right side for B samples. While A01 and B01 show the highest M_s values, the coated samples have lower values due to the coating shell. This makes sense since the more compounds are added around the SPIONs core the more the magnetic behavior of the SPIONs is suppressed.

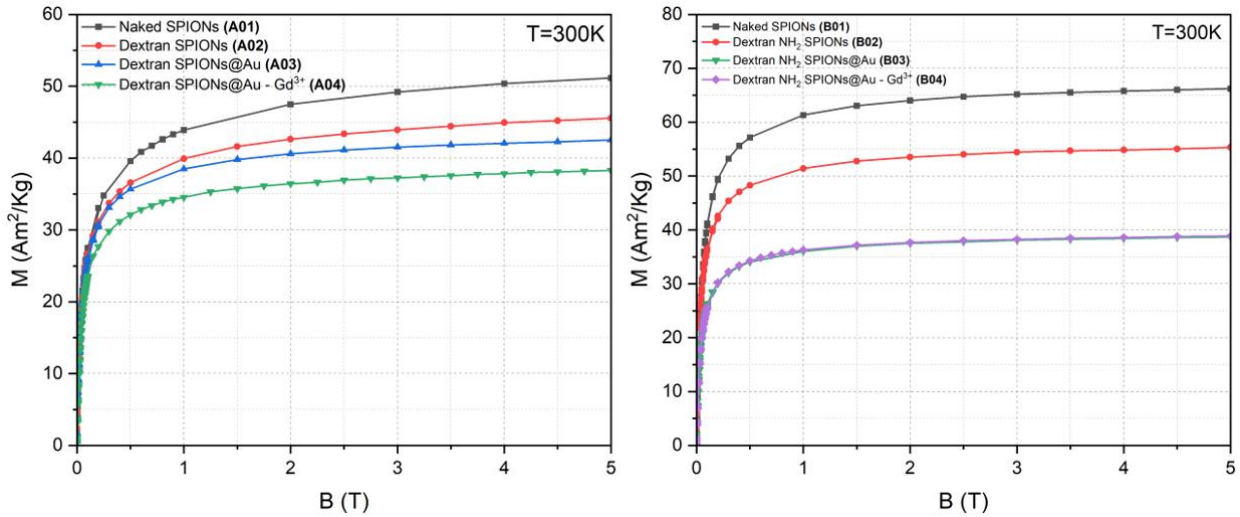

Figure 38: Magnetization curves for A samples (left) and B samples (right).

Figure 39 compares the M(B) curves at 300K for the coated samples A02 and B02 on the left side and A03 and B03, on the right side. The dextran coating decreases the M_s of A02 by 17.3% and B02 by

16.2% when compared to the correspondent naked samples. Concerning the dextran coating with the Au shell, sample A03 has a 16.6% reduction in M_s when compared to its naked version while sample B03 decreased by 41.4%. This significant reduction may be due to a more efficient coverage with the gold nanoparticles that mask the magnetic characteristics of iron oxide core. This best result may have been achieved by the use of Dx-NH_2 in these nanoparticles, which was chosen just to check it effect due to higher affinity with the NH_2 group.

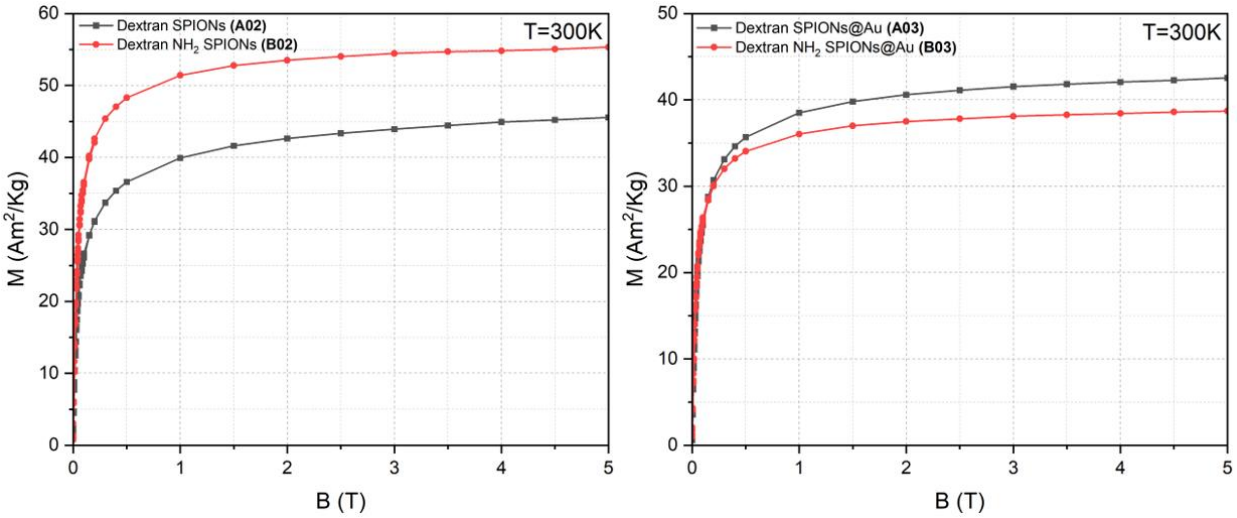

Figure 39: Field dependence of the magnetization curves for A02 and B02 (left) and A03 and B03 (right).

As the SPION cores gradually become more covered, the M_s values tend to decrease, as it happens to samples A04 and B04 (Figure 40a). For sample B04 this decrease reaches approximately 41% which suggest that from B03 to B04 there has been no change in the behavior of the M(B) curve. The M_s value of A04 decreased by 24.9% relative to its naked version. However, although this decrease is detected, they remain superparamagnetic at 300 K (Figure 40b) and present good values of saturation magnetization. This decrease on M_s is very low when compared to other values reported in the literature. In a study by *Stein et al., 2020* [99] SPIONs after gold coating lost 40% of their M_s while in a study by *Elbialy et al., 2014* [70], they lost 32.8%. Therefore, our results seem to indicate a breakthrough in this research. Overall, these magnetic results ensure that the use of such nanoparticles in biomedical is feasible and can be tested in further *in vitro* and *in vivo* assays.

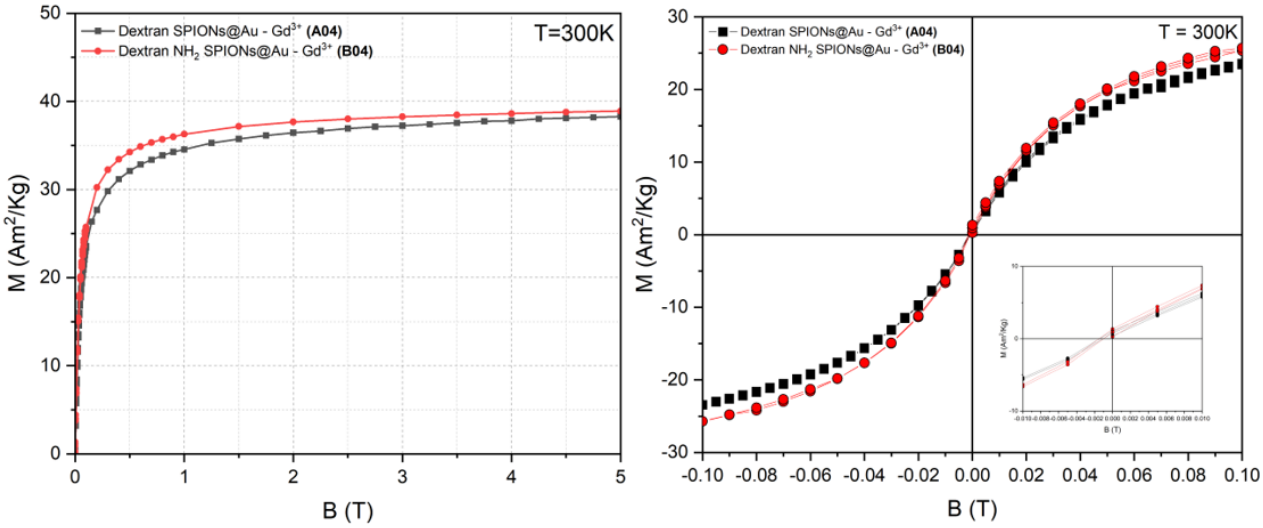

Figure 40: Field dependence of the magnetization curves for A04 and B04 samples (left) and hysteresis curves showing the superparamagnetic behavior of A04 and B04 at 300K (right).

Table 10 below shows all the magnetic measurements of M(B) obtained with the SQUID at temperatures of 10 K and 300 K.

Table 10: Magnetic parameters obtained by the magnetization measurements for all the studied samples.

	T=300K	T=10K		
Samples	M_s (Am^2/Kg)	M_s (Am^2/Kg)	M_r (Am^2/Kg)	H_C (T)
A01	51.00	60.59	10.12	0.018
A02	45.50	53.60	10.90	0.018
A03	42.54	48.32	8.83	0.017
A04	38.30	45.20	7.76	0.016
B01	66.00	78.00	12.43	0.017
B02	55.32	61.00	13.23	0.017
B03	38.70	43.80	9.29	0.016
B04	38.90	45.10	8.78	0.015
C01	62.80	74.00	24.00	0.021

Figure 41 shows the temperature dependence of the ZFC/FC magnetization curves of Naked SPIONs (A01, B01, and C01) measured by SQUID under an applied filed of 2.5 mT. The blocking temperature (T_b) was determined as the maximum value of ZFC curve. Larger nanoparticles require a higher temperature for the thermal energy to exceed the energy barrier, and thus be unlocked, and behave as superparamagnets. At this point there is a guarantee that all nanoparticles in the system are unblocked [100]. Samples A01, B01 and, C01 exhibit a T_b of 283.7, 284.7, and 299.9 K, respectively, which indicates that at RT they have superparamagnetic behavior, confirmed by the absence, at 300 K of coercivity and magnetic remanence, as showed on Figure 37b.

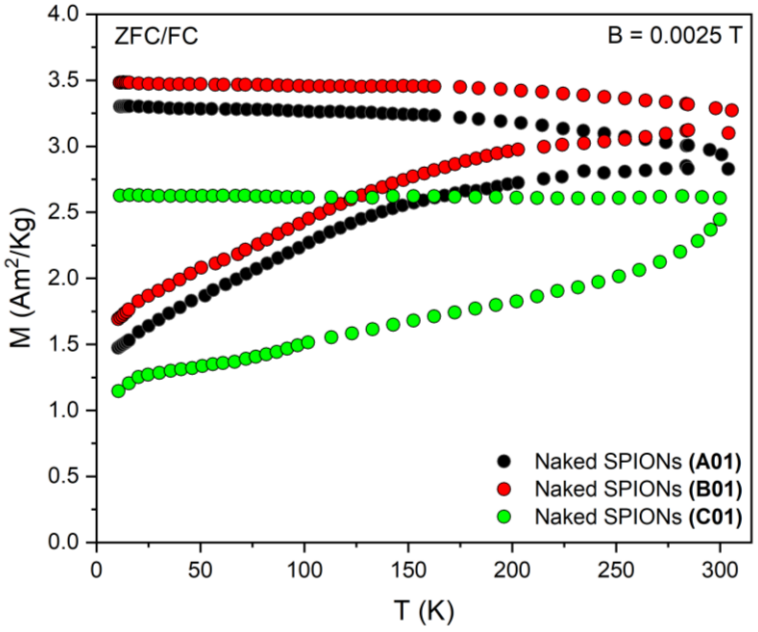

Figure 41: ZFC/FC curves for Naked SPIONs (A01, B01, and C01) under a magnetic field of 2.5 mT.

Figure 42 shows the ZFC/FC curves obtained under an applied field of 2.5 mT for A02 and of 50 mT for B02. The difference in the blocking temperatures observed for A02 T_b = 204.15 K and B02, T_b = 102.24 K are due to the different applied magnetic fields. In both cases, the superparamagnetic behavior above T_b remains constant.

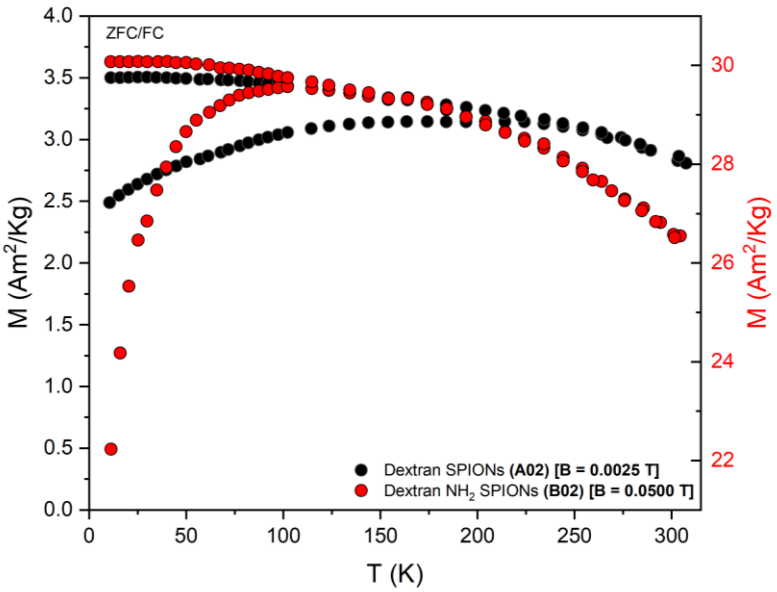

Figure 42: ZFC/FC curves under a magnetic field of 2.5 mT for A02, and under 50 mT for B02.

Figure 43 shows the ZFC/FC curves obtained under an applied field of 50 mT for SPIONs covered with dextran and coated with gold (A03 and B03). Gold coating reduced the blocking temperature in A03 more significantly, as these temperatures are now close together. A03 and B03 exhibits, quite similar T_b values, of 87.4 K and 92.3 K, respectively since the nanoparticles size is also similar (Table 9). In both cases, the superparamagnetic behavior above T_b remains constant.

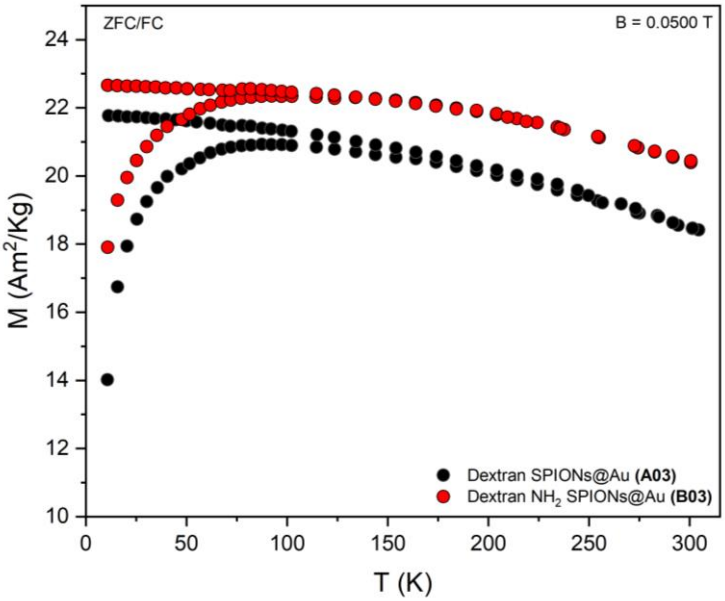

Figure 43: ZFC/FC curve for A03 and B03 under 50mT

In the Table 11 below T_b values obtained through the ZFC/FC curves for each sample are presented.

Table 11: Blocking temperature obtained by the highest value of the ZFC curve for each sample.

Samples	Blocking Temperature - $T_b(K)$
A01	283.68
A02	204.15
A03	87.38
A04	92.10
B01	284.69
B02	102.24
B03	92.27
B04	-
C01	299.92

Knowing that all the samples exhibit superparamagnetic behavior at RT, it is possible to determine the mean magnetic diameter (D_{MAG}) of the nanoparticles considering the M(B) curve obtained at 300 K through the Langevin model shown below (9) [50]:

$$D_{MAG} = \left(\frac{18 K_b T \left(\frac{dM}{dB}\right)_{(B \to 0)}}{\pi \rho {M_s}^2} \right)^{\frac{1}{3}} \quad (9)$$

where K_b is the Boltzmann constant which is equal to 1.381 x 10^{-23} m^2Kg/s^2K, T is the temperature in Kelvin, $\left(\frac{dM}{dB}\right)_{(B \to 0)}$ is the derivative of first order of the curve M(B) at the point B = 0, M_s is the saturation magnetization, and ρ is the mass density of the iron oxide structure. Although it is known by Mössbauer spectroscopy that the samples contain between 11 to 17% in magnetite, in order to simplify these calculations, it was assumed for that all samples have 100% in maghemite, which gives ρ = 4900 Kg/m^3. These calculations are presented in Table 12. By comparing these results with the ones already determined by PXRD and TEM characterization, one can verify a good agreement between all of them.

Table 12: Comparison between nanoparticles diameter determined by PXRD, TEM, and SQUID.

Sample	Crystallite Size D_{XRD} (nm)	Particle Size D_{TEM} (nm)	Magnetic Diameter D_{MAG} (nm)
A01	9.04	10.02 ± 2.10	10.51
A02	7.79	6.60 ± 1.82	11.00
A03	9.81	10.91 ± 2.71	11.68
A04	9.40	11.34 ± 2.75	12.28
B01	9.84	9.85 ± 1.97	9.55
B02	9.60	9.76 ± 2.12	11.72
B03	10.55	10.00 ± 2.27	11.85
B04	9.76	11.02 ± 2.21	13.13
C01	9.98	8.30 ± 1.73	9.84

4.3 Magnetic Hyperthermia

Due to several constraints, magnetic hyperthermia tests were only possible for samples B01, B02, and B03. This study showed that the highest temperature variation [ΔT (ºC)] as a function of time (s) occurred for the sample B01, which reached a variation of 8 °C. Coated samples B02 and B03 have shown practically the same variation, 3.7 ºC for B02 and 3.5 ºC for B03 (Figure 44). B01 sample reaches a temperature higher than 40 °C in approximately 200 s inside a human body in these conditions, whereas B02 and B03 achieves the same temperature only after approximately 500 s. This difference could be attributed to the organic covering of Dx – NH_2 that behave as an insulating shell around the SPION's surface [101].

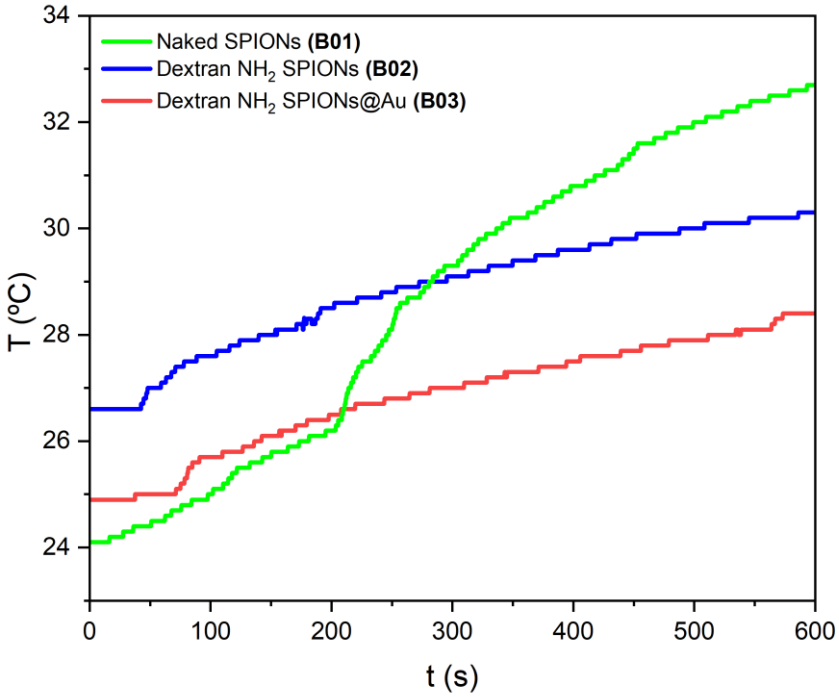

Figure 44: Hyperthermia curves of temperature (ºC) vs. time (s) for B samples.

The parameter known as Specific Absorption Rate (SAR) is used to characterize the heating efficiency of a magnetic material by measuring its energy absorption when exposed to an AC magnetic field. This value is calculated by using the equation (10) and is defined as the amount of power absorbed by the sample per mass unit (W/g):

$$SAR = \frac{C_S m_{Fe} + C_w m_w}{m_{Fe}} \left(\frac{dT}{dt}\right)_{(Max)} \quad (10)$$

Where $\left(\frac{dT}{dt}\right)_{(Max)}$ is the maximum gradient of the temperature curve of the SPIONs in water submitted to the hyperthermia test, C_S is the specific heat of the nanoparticles, C_W is the specific heat of the liquid, m_w is the water mass, and m_{Fe} is the iron mass in the sample. Figure 45 shows the SAR values calculated for B01, B02, and B03.

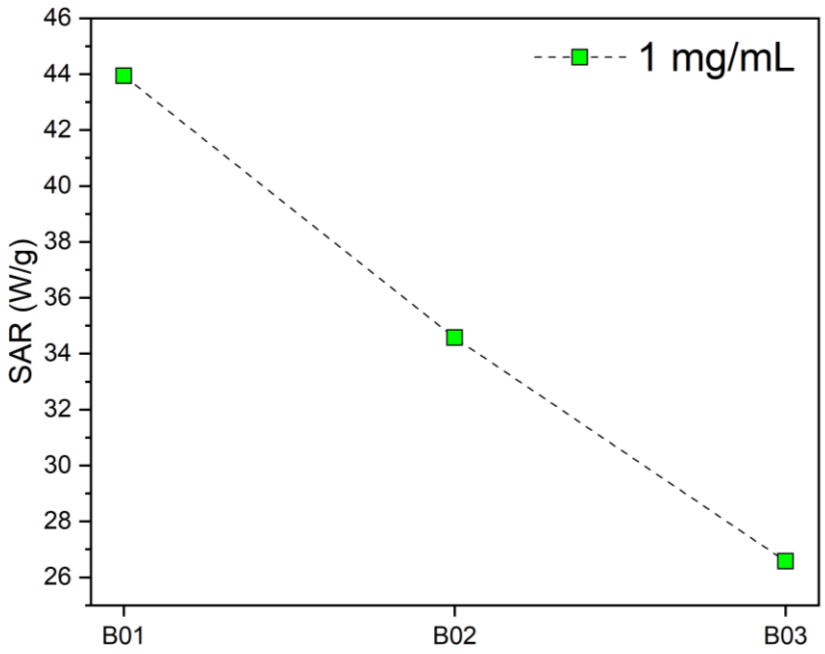

Figure 45: SAR values obtained for B01, B01, and B03.

B samples are promising option for inducing apoptosis in cancer cells at temperatures between 40 and 45 degrees Celsius [39,40]. In addition, the SAR values for B01, B02, and B03 correspond to those reported in the literature [102].

Table 13 shows the values of ΔT (ºC) and SAR through magnetic hyperthermia for B samples.

Table 13: Values of temperature variation (ºC) and SAR (W/g) obtained for B01, B02, and B03.

Sample	ΔT (ºC)	SAR (W/g)
B01	8.7	43.94
B02	3.7	34.57
B03	3.5	26.57

4.4 Cytotoxicity Assay

Although at a preliminary stage, it was still possible in this work to perform cytotoxicity tests in samples A04 and B04. The cytotoxicity of SPIONs has been attributed to both structural factors related to their size, shape, charge as well as their coatings. Therefore, the cytotoxic effect of SPIONs A04 and B04 was studied using the PC3 cells (prostate cancer) in order to obtain information regarding the selection of the most suitable concentrations to use in future studies on the evaluation of these platforms as theranostic agents. The MTT assay, a metabolic assay considered the "gold standard" for cytotoxicity, was selected for the evaluation of the cell viability of these SPIONs.

The results obtained by the MTT assay on the PC3 cells treated for 24h with serial dilutions of SPIONs A04 and B04 (10 to 50 µg Fe/mL) and their respective precursors A01 and B01 are presented in Figure 46. Dilutions in concentration of 100, 200, and 500 µg Fe/mL were removed because they presented a stronger coloration, which interfered with the spectrophotometric measurement. These results show that for concentrations up to 50 µg Fe/mL it is feasible to proceed with tests in PC3 cells, with the worst-case scenario killing approximately 25% of cells at 25 and 50 µg Fe/mL for sample B04.

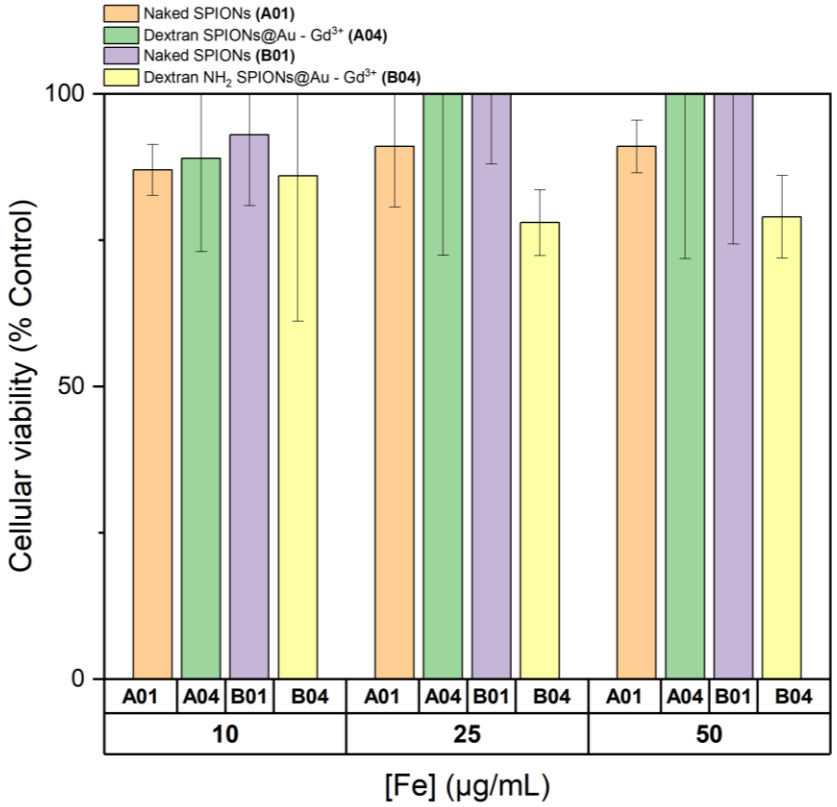

Figure 46: Graphical diagram showing the cellular viability for A01, A04, B01 and B04 samples at different concentrations of Iron.

Chapter 5

Conclusion and Future Work

5.1 Conclusion

The work developed in this thesis had as main objective the synthesis of iron oxide nanoparticles able to be used as a nanoplatform for drug delivery for therapy and imaging. The advantage of such nanosystems is the combination of diagnostics and therapy allowing the possibility to acquire real-time information about the delivery and eventually the effects of therapeutic agents when administered to patients.

These nanoparticles were produced by the chemical precipitation, which provided SPIONs with diameters smaller than 11nm and with magnetizations greater than 50 Am2/Kg. Three different approaches were elaborated. In the first one (A samples) the reduction of Fe was used to obtain the amount of iron ions necessary for precipitation, in the second method (B samples) a hydrothermal post treatment was used and in the third one (C samples) a fine monitoring of the pH to reach 9.5 was made during the precipitation phase of Fe3O4. Method B provided a smaller size dispersion of the nanoparticles, with 19% and samples with the best saturation magnetization of 66 Am^2/Kg while method C showed to be more efficient to obtain samples with smaller particle size of 8.3 ± 1.73 nm through TEM with spherical shape. With method A the shape of the nanoparticles varied greatly, and they also have a goethite phase, which although in low percentage is considered a non-desirable phase for further biomedical applications.

Since iron oxides nanoparticles have a natural tendency to aggregate, surface modification and stabilization of SPIONs A and B was performed by adding Dx and Dx-NH2, respectively. The SPIONs were further covered with a gold shell with the goal to obtain a uniform and continuous coating with a thickness that does not lead to substantial loss of the magnetic performance of the nanoparticles and functionalized with TDOTA complexed gadolinium (III). All the prepared samples were characterized in terms of size, phases, morphology, and stability by a combination of techniques such as, DLS, PXRD, TEM, Zeta Potential, and Mössbauer spectroscopy. The content of metals Fe, Au and Gd have been determined by ICP-MS. A detailed magnetic study by static magnetization to assess their magnetic performance, namely in terms of superparamagnetic (single domain) and blocking behavior was also performed.

ICP-MS analyses reveal that Gadolinium and Gold are present in samples A04 and B04. TEM images show that the final product B04 has a good dispersion of the nanoparticles in the medium, being crucial for theranostic applications.

Magnetization studies have shown that SPIONs core of these samples keep their superparamagnetic behavior assuring the maintenance of the magnetic properties in A04 and B04. Particle size determined by PXRD, TEM and SQUID is about 10.19 nm which is a considerable good size for *in vivo* applications, and it is consistent with other reported studies [87-90].

Analysis by Mössbauer spectroscopy revealed that SPIONs are mainly composed by maghemite with approximate 13% of magnetite, which improve the magnetic character of the samples

Regarding the magnetic hyperthermia tests, due to several constraints it was not possible to perform those measurements for all samples. However, preliminary tests on samples B01, B02 and B03 have shown that sample B01 present a quite significant temperature variation, of 8.7 ºC, and may be efficient to generate the apoptosis of cancer cells that occurs between 40-45ºC [39, 40].

Cytotoxicity assay *in vitro* allowed us to know that concentrations of these samples up to 50 ug Fe/mL do not generate significant damage to PC3 cells, so at these concentrations it is possible to continue with future MRI and Magnetic Hyperthermia tests *in vitro* and later *in vivo*.

The strategy to undertake a systematic study of preparation of SPIONs has proved to be innovative and the results found encouraging providing a clear indication on the potential application of these SPIONs-nanoplatforms as bimodal probes in cancer diagnosis.

5.2 Future Work

Despite the large volume of work done in this thesis there are some loose ends concerning different characterization studies, namely:

- The magnetic hyperthermia measurements of all the samples under different conditions of sample concentrations, and operational parameters, such frequency and alternate magnetic field.
- The DLS and zeta potential analysis at different pH values in order to obtain information concerning the stability of such nanoparticles in the physiologic medium (human body). These results could be advantageous to understand and improve further surface modifications of SPIONs.

After all the characterization studies and once cell viability assays are concluded the decision to proceed to *in vitro* and *in vivo* tests on PC3 cells, should be done in order to perform MRI and magnetic hyperthermia assays in those cells.

References

[1] H.-L. Rao *et al.*, “Increased Intratumoral Neutrophil in Colorectal Carcinomas Correlates Closely with Malignant Phenotype and Predicts Patients’ Adverse Prognosis,” *PLoS ONE*, vol. 7, no. 1, p. e30806, Jan. 2012, doi: 10.1371/journal.pone.0030806.

[2] Z. Defu, Y. Ting, Y. Jian, F. Shuang, and Z. Shubiao, “Targeting strategies for superparamagnetic iron oxide nanoparticles in cancer therapy,” *Acta Mater. Inc*, vol. 102, pp. 13–34, 2020, doi: 10.1016/j.actbio.2019.11.027.

[3] C. Sun, J. S. H. Lee, and M. Zhang, “Magnetic nanoparticles in MR imaging and drug delivery,” *Adv. Drug Deliv. Rev.*, vol. 60, no. 11, pp. 1252–1265, Aug. 2008, doi: 10.1016/j.addr.2008.03.018.

[4] J. Chomoucka, J. Drbohlavova, D. Huska, V. Adam, R. Kizek, and J. Hubalek, “Magnetic nanoparticles and targeted drug delivering,” *Pharmacol. Res.*, vol. 62, no. 2, pp. 144–149, Aug. 2010, doi: 10.1016/j.phrs.2010.01.014.

[5] M. K. Lima-Tenório, E. A. Gómez Pineda, N. M. Ahmad, H. Fessi, and A. Elaissari, “Magnetic nanoparticles: In vivo cancer diagnosis and therapy,” *Int. J. Pharm.*, vol. 493, no. 1–2, pp. 313–327, Sep. 2015, doi: 10.1016/j.ijpharm.2015.07.059.

[6] Z. Qiao and X. Shi, “Dendrimer-based molecular imaging contrast agents,” *Prog. Polym. Sci.*, vol. 44, pp. 1–27, May 2015, doi: 10.1016/j.progpolymsci.2014.08.002.

[7] J. Gao, H. Gu, and B. Xu, “Multifunctional Magnetic Nanoparticles: Design, Synthesis, and Biomedical Applications,” *Acc. Chem. Res.*, vol. 42, no. 8, pp. 1097–1107, Aug. 2009, doi: 10.1021/ar9000026.

[8] S. Palanisamy and Y.-M. Wang, “Superparamagnetic iron oxide nanoparticulate system: synthesis, targeting, drug delivery and therapy in cancer,” *Dalton Trans.*, vol. 48, no. 26, pp. 9490–9515, 2019, doi: 10.1039/C9DT00459A.

[9] J. Conde, J. T. Dias, V. GrazÃº, M. Moros, P. V. Baptista, and J. M. de la Fuente, “Revisiting 30 years of biofunctionalization and surface chemistry of inorganic nanoparticles for nanomedicine,” *Front. Chem.*, vol. 2, Jul. 2014, doi: 10.3389/fchem.2014.00048.

[10] O. A. A. Aziz, K. Arafa, A. S. A. Dena, and I. M. El-Sherbiny, “Superparamagnetic Iron Oxide Nanoparticles (SPIONs): Preparation and Recent Applications,” no. 1, p. 10, 2020.

[11] S. Laurent *et al.*, “Magnetic Iron Oxide Nanoparticles: Synthesis, Stabilization, Vectorization, Physicochemical Characterizations, and Biological Applications,” *Chem. Rev.*, vol. 108, no. 6, pp. 2064–2110, Jun. 2008, doi: 10.1021/cr068445e.

[12] M. R. Faria, M. M. Cruz, M. C. Gonçalves, A. Carvalho, G. Feio, and M. B. F. Martins, “Synthesis and characterization of magnetoliposomes for MRI contrast enhancement,” *Int. J. Pharm.*, vol. 446, no. 1–2, pp. 183–190, Mar. 2013, doi: 10.1016/j.ijpharm.2013.02.025.

[13] L. Blomqvist, G. F. Nordberg, V. M. Nurchi, and J. O. Aaseth, “Gadolinium in Medical Imaging—Usefulness, Toxic Reactions and Possible Countermeasures—A Review,” *Biomolecules*, vol. 12, no. 6, p. 742, May 2022, doi: 10.3390/biom12060742.

[14] J. Wahsner, E. M. Gale, A. Rodríguez-Rodríguez, and P. Caravan, “Chemistry of MRI Contrast Agents: Current Challenges and New Frontiers,” *Chem. Rev.*, vol. 119, no. 2, pp. 957–1057, Jan. 2019, doi: 10.1021/acs.chemrev.8b00363.

[15] S. Caspani, R. Magalhães, J. P. Araújo, and C. T. Sousa, “Magnetic nanomaterials as contrast agents for MRI,” p. 37, 2020.

[16] N. A. Spaldin and N. D. Mathur, “Magnetic materials: fundamentals and device applications,” *Phys. Today*, vol. 56, no. 12, pp. 62–63, 2003.

[17] Muljadi, P. Sardjono, and Suprapedi, “Preparation and Characterization of 5wt.% Epoxy Resin Bonded Magnet NdFeB for Micro Generator Application,” *Energy Procedia*, vol. 68, pp. 282–287, Apr. 2015, doi: 10.1016/j.egypro.2015.03.257.

[18] V. Manescu (Paltanea), G. Paltanea, I. Antoniac, and M. Vasilescu, “Magnetic Nanoparticles Used in Oncology,” *Materials*, vol. 14, no. 20, p. 5948, Oct. 2021, doi: 10.3390/ma14205948.

[19] G. Kandasamy and D. Maity, “Recent advances in superparamagnetic iron oxide nanoparticles (SPIONs) for in vitro and in vivo cancer nanotheranostics,” *Int. J. Pharm.*, vol. 496, no. 2, pp. 191–218, Dec. 2015, doi: 10.1016/j.ijpharm.2015.10.058.

[20] J. C. Matos, M. C. Gonçalves, L. C. Pereira, B. J. Vieira, and J. C. Waerenborgh, “SPIONs prepared in air through improved synthesis methodology: the influence of γ-Fe2O3/Fe3O4 ratio and coating composition on magnetic properties,” *Nanomaterials*, vol. 9, no. 7, p. 943, 2019, doi: 10.3390/nano9070943.
[21] C. de Montferrand *et al.*, “SiO2 versus chelating agent@ iron oxide nanoparticles: interactions effect in nanoparticles assemblies at low magnetic field,” *J. Sol-Gel Sci. Technol.*, vol. 73, no. 3, pp. 572–579, Mar. 2015, doi: 10.1007/s10971-014-3526-y.
[22] M. Darbandi *et al.*, “Nanoscale size effect on surface spin canting in iron oxide nanoparticles synthesized by the microemulsion method,” *J. Phys. Appl. Phys.*, vol. 45, no. 19, p. 195001, May 2012, doi: 10.1088/0022-3727/45/19/195001.
[23] M. A. Al-Kinani, A. J. Haider, and S. Al-Musawi, “Design, Construction and Characterization of Intelligence Polymer Coated Core–Shell Nanocarrier for Curcumin Drug Encapsulation and Delivery in Lung Cancer Therapy Purposes,” *J. Inorg. Organomet. Polym. Mater.*, vol. 31, no. 1, pp. 70–79, Jan. 2021, doi: 10.1007/s10904-020-01672-w.
[24] K. M. Krishnan, “Biomedical Nanomagnetics: A Spin Through Possibilities in Imaging, Diagnostics, and Therapy,” *IEEE Trans. Magn.*, vol. 46, no. 7, pp. 2523–2558, Jul. 2010, doi: 10.1109/TMAG.2010.2046907.
[25] E. Tombácz, R. Turcu, V. Socoliuc, and L. Vékás, “Magnetic iron oxide nanoparticles: Recent trends in design and synthesis of magnetoresponsive nanosystems,” *Biochem. Biophys. Res. Commun.*, vol. 468, no. 3, pp. 442–453, Dec. 2015, doi: 10.1016/j.bbrc.2015.08.030.
[26] J. Dulińska-Litewka, A. Łazarczyk, P. Hałubiec, O. Szafrański, K. Karnas, and A. Karewicz, “Superparamagnetic Iron Oxide Nanoparticles—Current and Prospective Medical Applications,” *Materials*, vol. 12, no. 4, p. 617, Feb. 2019, doi: 10.3390/ma12040617.
[27] M. D. Carvalho, F. Henriques, L. P. Ferreira, M. Godinho, and M. M. Cruz, “Iron oxide nanoparticles: the Influence of synthesis method and size on composition and magnetic properties,” *J. Solid State Chem.*, vol. 201, pp. 144–152, May 2013, doi: 10.1016/j.jssc.2013.02.024.
[28] X. Zhang, Y. Niu, X. Meng, Y. Li, and J. Zhao, “Structural evolution and characteristics of the phase transformations between α-Fe2O3, Fe3O4 and γ-Fe2O3 nanoparticles under reducing and oxidizing atmospheres,” *CrystEngComm*, vol. 15, no. 40, p. 8166, 2013, doi: 10.1039/c3ce41269e.
[29] A. S. Teja and P.-Y. Koh, “Synthesis, properties, and applications of magnetic iron oxide nanoparticles,” *Prog. Cryst. Growth Charact. Mater.*, vol. 55, no. 1–2, pp. 22–45, Mar. 2009, doi: 10.1016/j.pcrysgrow.2008.08.003.
[30] C. Yang, J. Wu, and Y. Hou, “Fe3O4 nanostructures: synthesis, growth mechanism, properties and applications,” *Chem. Commun.*, vol. 47, no. 18, p. 5130, 2011, doi: 10.1039/c0cc05862a.
[31] Y. Cheng, L. Yin, S. Lin, M. Wiesner, E. Bernhardt, and J. Liu, “Toxicity Reduction of Polymer-Stabilized Silver Nanoparticles by Sunlight,” *J. Phys. Chem. C*, vol. 115, no. 11, pp. 4425–4432, Mar. 2011, doi: 10.1021/jp109789j.
[32] Z. Xu, Y. Hou, and S. Sun, “Magnetic Core/Shell Fe_3O_4/Au and Fe_3O_4/Au/Ag Nanoparticles with Tunable Plasmonic Properties,” *J. Am. Chem. Soc.*, vol. 129, no. 28, pp. 8698–8699, Jul. 2007, doi: 10.1021/ja073057v.
[33] S. H. Lee, B. H. Kim, H. B. Na, and T. Hyeon, “Paramagnetic inorganic nanoparticles as T_1 MRI contrast agents,” *WIREs Nanomedicine Nanobiotechnology*, vol. 6, no. 2, pp. 196–209, Mar. 2014, doi: 10.1002/wnan.1243.
[34] Z. R. Stephen, F. M. Kievit, and M. Zhang, “Magnetite nanoparticles for medical MR imaging,” *Mater. Today*, vol. 14, no. 7–8, pp. 330–338, Jul. 2011, doi: 10.1016/S1369-7021(11)70163-8.
[35] A. Carvalho, M. B. F. Martins, M. L. Corvo, and G. Feio, “Enhanced contrast efficiency in MRI by PEGylated magnetoliposomes loaded with PEGylated SPION: Effect of SPION coating and micro-environment,” *Mater. Sci. Eng. C*, vol. 43, pp. 521–526, Oct. 2014, doi: 10.1016/j.msec.2014.07.055.
[36] S. Xie *et al.*, “Superparamagnetic iron oxide nanoparticles coated with different polymers and their MRI contrast effects in the mouse brains,” *Appl. Surf. Sci.*, vol. 326, pp. 32–38, Jan. 2015, doi: 10.1016/j.apsusc.2014.11.099.
[37] T. Rheinla and W. Semmler, “Magnetic fractionation of magnetic #uids,” *J. Magn. Magn. Mater.*, p. 10, 2000.

[38] A. Chicheł, J. Skowronek, M. Kubaszewska, and M. Kanikowski, “Hyperthermia – description of a method and a review of clinical applications,” *Rep. Pract. Oncol. Radiother.*, vol. 12, no. 5, pp. 267–275, Sep. 2007, doi: 10.1016/S1507-1367(10)60065-X.
[39] K. Mahmoudi, A. Bouras, D. Bozec, R. Ivkov, and C. Hadjipanayis, “Magnetic hyperthermia therapy for the treatment of glioblastoma: a review of the therapy’s history, efficacy and application in humans,” *Int. J. Hyperthermia*, vol. 34, no. 8, pp. 1316–1328, Nov. 2018, doi: 10.1080/02656736.2018.1430867.
[40] O. L. Lanier *et al.*, “Evaluation of magnetic nanoparticles for magnetic fluid hyperthermia,” *Int. J. Hyperthermia*, vol. 36, no. 1, pp. 686–700, Jan. 2019, doi: 10.1080/02656736.2019.1628313.
[41] N. M. dos Santos, “Nanopartículas magnéticas biocompatíveis e funcionalizadas com ácido fólico como potencial agente teranóstico no tratamento de câncer via magnetohipertermia,” Mestrado em Físico-Química, Universidade de São Paulo, São Carlos, 2021. doi: 10.11606/D.75.2021.tde-10112021-165537.
[42] P. I. P. Soares, I. M. M. Ferreira, and P. M. R. Borges, “Application of Hyperthermia for Cancer Treatment: Recent Patents Review,” p. 10.
[43] D. Chang *et al.*, “Biologically Targeted Magnetic Hyperthermia: Potential and Limitations,” *Front. Pharmacol.*, vol. 9, p. 831, Aug. 2018, doi: 10.3389/fphar.2018.00831.
[44] P. Moroz, S. K. Jones, and B. N. Gray, “Magnetically mediated hyperthermia: current status and future directions,” *Int. J. Hyperthermia*, vol. 18, no. 4, pp. 267–284, Jan. 2002, doi: 10.1080/02656730110108785.
[45] A. Jordan, P. Wust, H. Fähling, W. John, A. Hinz, and R. Felix, “Inductive heating of ferrimagnetic particles and magnetic fluids: Physical evaluation of their potential for hyperthermia,” p. 18.
[46] K. Maier-Hauff *et al.*, “Intracranial Thermotherapy using Magnetic Nanoparticles Combined with External Beam Radiotherapy: Results of a Feasibility Study on Patients with Glioblastoma Multiforme,” *J. Neurooncol.*, vol. 81, no. 1, pp. 53–60, Jan. 2007, doi: 10.1007/s11060-006-9195-0.
[47] M. Musielak, I. Piotrowski, and W. M. Suchorska, “Superparamagnetic iron oxide nanoparticles (SPIONs) as a multifunctional tool in various cancer therapies,” *Rep. Pract. Oncol. Radiother.*, vol. 24, no. 4, pp. 307–314, Jul. 2019, doi: 10.1016/j.rpor.2019.04.002.
[48] Y. Sun *et al.*, “An improved way to prepare superparamagnetic magnetite-silica core-shell nanoparticles for possible biological application,” *J. Magn. Magn. Mater.*, vol. 285, no. 1–2, pp. 65–70, Jan. 2005, doi: 10.1016/j.jmmm.2004.07.016.
[49] A. Z. Md. Badruddoza *et al.*, “β-Cyclodextrin conjugated magnetic, fluorescent silica core–shell nanoparticles for biomedical applications,” *Carbohydr. Polym.*, vol. 95, no. 1, pp. 449–457, Jun. 2013, doi: 10.1016/j.carbpol.2013.02.046.
[50] M. Anwar *et al.*, “AQUEOUS PHASE TRANSFER OF OLEIC ACID COATED IRON OXIDE NANOPARTICLES: INFLUENCE OF SOLVENTS AND SURFACTANTS ON STABILITY AND PHARMACEUTICAL APPLICATIONS OF FERROFLUID,” p. 6.
[51] Y. Zhang *et al.*, “Synthesis of PVP-coated ultra-small Fe3O4 nanoparticles as a MRI contrast agent,” *J. Mater. Sci. Mater. Med.*, vol. 21, no. 4, pp. 1205–1210, Apr. 2010, doi: 10.1007/s10856-009-3881-3.
[52] S. Yoffe, T. Leshuk, P. Everett, and F. Gu, “Superparamagnetic Iron Oxide Nanoparticles (SPIONs): Synthesis and Surface Modification Techniques for use with MRI and Other Biomedical Applications,” p. 17.
[53] W. Wu, Q. He, and C. Jiang, “Magnetic Iron Oxide Nanoparticles: Synthesis and Surface Functionalization Strategies,” *Nanoscale Res. Lett.*, vol. 3, no. 11, p. 397, Nov. 2008, doi: 10.1007/s11671-008-9174-9.
[54] G. Gnanaprakash, J. Philip, T. Jayakumar, and B. Raj, “Effect of digestion time and alkali addition rate on physical properties of magnetite nanoparticles,” *J. Phys. Chem. B*, vol. 111, no. 28, pp. 7978–7986, Jul. 2007, doi: 10.1021/jp071299b.
[55] U. S. Khan, N. S. Khattak, A. Manan, A. Rahman, F. Khan, and A. Rahim, “Some Properties of Magnetite Nanoparticles Produced Under Different Conditions,” *J. Electron. Mater.*, vol. 44, no. 1, pp. 303–312, Jan. 2015, doi: 10.1007/s11664-014-3467-9.
[56] M. Morais *et al.*, “Radiolabeled Mannosylated Dextran Derivatives Bearing an NIR-Fluorophore for Sentinel Lymph Node Imaging,” *Bioconjug. Chem.*, vol. 25, no. 11, pp. 1963–1970, Nov. 2014, doi: 10.1021/bc500336a.

[57] J. Djajadisastra, P. Purnamasari, and A. Pujiyanto, “ANTIOXIDANT ACTIVITY OF GOLD NANOPARTICLES USING GUM ARABIC AS A STABILIZING,” vol. 6, no. 7, p. 5.
[58] J. Lin *et al.*, “Gold-coated iron (Fe@Au) nanoparticles: Synthesis, characterization, and magnetic field-induced self-assembly,” *J. Solid State Chem.*, vol. 159, no. 1, pp. 26–31, 2001, doi: 10.1006/jssc.2001.9117.
[59] O. Chen *et al.*, “Magneto-fluorescent core-shell supernanoparticles,” *Nat. Commun.*, vol. 5, no. 1, p. 5093, Dec. 2014, doi: 10.1038/ncomms6093.
[60] J. C. O. Silva, M. H. Sousa, F. A. Tourinho, and J. C. Rubim, “Raman Spectroscopic Investigation of Maghemite Ferrofluids Modified by the Adsorption of Zinc Tetrasulfonated Phthalocyanine,” *Langmuir*, vol. 18, no. 14, pp. 5511–5515, Jul. 2002, doi: 10.1021/la020078o.
[61] E. R. L. Siqueira, “Nanoestruturas magnéticas revestidas com ouro como agente indutor de magneto-hipertermia para tratamento de câncer de mama,” Universidade de Brasília - UnB, Brasília.
[62] L. C. Kennedy *et al.*, “A new era for cancer treatment: gold-nanoparticle-mediated thermal therapies,” *Small*, vol. 7, no. 2, pp. 169–183, 2011.
[63] F. Lux, L. Sancey, A. Bianchi, Y. Crémillieux, S. Roux, and O. Tillement, “Gadolinium-based nanoparticles for theranostic MRI-radiosensitization,” *Nanomed.*, vol. 10, no. 11, pp. 1801–1815, Jun. 2015, doi: 10.2217/nnm.15.30.
[64] A. D. Sherry, P. Caravan, and R. E. Lenkinski, “Primer on gadolinium chemistry,” *J. Magn. Reson. Imaging*, vol. 30, no. 6, pp. 1240–1248, Dec. 2009, doi: 10.1002/jmri.21966.
[65] A. S. Merbach, L. Helm, and E. Toth, *The chemistry of contrast agents in medical magnetic resonance imaging*. John Wiley & Sons, 2013.
[66] C. F. G. C. Geraldes and S. Laurent, “Classification and basic properties of contrast agents for magnetic resonance imaging,” *Contrast Media Mol. Imaging*, vol. 4, no. 1, pp. 1–23, Jan. 2009, doi: 10.1002/cmmi.265.
[67] P. I. P. Soares *et al.*, “Effects of surfactants on the magnetic properties of iron oxide colloids,” *J. Colloid Interface Sci.*, vol. 419, pp. 46–51, Apr. 2014, doi: 10.1016/j.jcis.2013.12.045.
[68] A. S. Saraiva *et al.*, “3D-printed platform multi-loaded with bioactive, magnetic nanoparticles and an antibiotic for re-growing bone tissue,” *Int. J. Pharm.*, vol. 593, p. 120097, Jan. 2021, doi: 10.1016/j.ijpharm.2020.120097.
[69] C. Caro *et al.*, “Fe3O4-Au core-shell nanoparticles as a multimodal platform for in vivo imaging and focused photothermal therapy,” *Pharmaceutics*, vol. 13, no. 3, Mar. 2021, doi: 10.3390/pharmaceutics13030416.
[70] N. S. Elbialy, M. M. Fathy, and W. M. Khalil, “Preparation and characterization of magnetic gold nanoparticles to be used as doxorubicin nanocarriers,” *Phys. Med.*, vol. 30, no. 7, pp. 843–848, Nov. 2014, doi: 10.1016/j.ejmp.2014.05.012.
[71] F. Silva *et al.*, “Interrogating the Role of Receptor-Mediated Mechanisms: Biological Fate of Peptide-Functionalized Radiolabeled Gold Nanoparticles in Tumor Mice,” *Bioconjug. Chem.*, vol. 27, no. 4, pp. 1153–1164, Apr. 2016, doi: 10.1021/acs.bioconjchem.6b00102.
[72] S. Mourdikoudis, R. M. Pallares, and N. T. K. Thanh, “Characterization techniques for nanoparticles: comparison and complementarity upon studying nanoparticle properties,” *Nanoscale*, vol. 10, no. 27, pp. 12871–12934, 2018, doi: 10.1039/C8NR02278J.
[73] G. J. Long, T. Cranshaw, and G. Longworth, “The ideal Mössbauer effect absorber thickness,” *Mössbauer Eff. Ref. Data J.*, vol. 6, no. 2, pp. 42–49, 1983.
[74] J. Hesse and A. Rubartsch, “Model independent evaluation of overlapped Mossbauer spectra,” *J. Phys. [E]*, vol. 7, no. 7, p. 526, 1974.
[75] Cryogenic Ltd, “S700X SQUID Magnetometer USER MANUAL Version 0.9”.
[76] S. Mahadevan, G. Gnanaprakash, J. Philip, B. P. C. Rao, and T. Jayakumar, “X-ray diffraction-based characterization of magnetite nanoparticles in presence of goethite and correlation with magnetic properties,” *Phys. E Low-Dimens. Syst. Nanostructures*, vol. 39, no. 1, pp. 20–25, Jul. 2007, doi: 10.1016/j.physe.2006.12.041.
[77] Hari-Bala *et al.*, “Controlling the particle size of nanocrystalline titania via a thermal dissociation of substrates with ammonium chloride,” *Mater. Lett.*, vol. 60, no. 4, pp. 494–498, Feb. 2006, doi: 10.1016/j.matlet.2005.09.030.
[78] J. F. Dorsey *et al.*, “Gold nanoparticles in radiation research: potential applications for imaging and radiosensitization,” *Transl. Cancer Res.*, vol. 2, no. 4, p. 12, 2013.

[79] S. Fatimah, R. Ragadhita, D. Fitria, A. Husaeni, A. Bayu, and D. Nandiyanto, “How to Calculate Crystallite Size from X-Ray Diffraction (XRD) using Scherrer Method,” *ASEAN J. Sci. Eng.*, pp. 65–76, 2021, doi: 10.17509/ijost.v6ix.
[80] S. Mornp, “Mössbauer effect studies of microcrystalline materials,” *Plenum Press Mossbauer Spectrosc. Appl. Inorg. Chem.*, vol. 2, pp. 89–123, 1987.
[81] E. Murad, “Clays and clay minerals: what can Mössbauer spectroscopy do to help understand them?,” *Hyperfine Interact.*, vol. 117, no. 1, pp. 39–70, 1998, doi: 10.1023/A:101263512.
[82] A. G. Roca, J. F. Marco, and M. del Puerto, “Effect of Nature and Particle Size on Properties of Uniform Magnetite and Maghemite Nanoparticles.,” *J Serna J Phys Chem C*, vol. 111, p. 18577, 2007, doi: 10.1021/jp075133m.
[83] D. Pedroi *et al.*, “Magnetic relaxation phenomena and inter-particle interactions in nanosized γ-Fe2O3 systems,” *J Phys Condens Matter*, vol. 15, pp. 1797–1811, 2003, doi: 10.1088/0953-8984/15/40/C01.
[84] W. Baaziz *et al.*, “Magnetic Iron Oxide Nanoparticles: Reproducible Tuning of the Size and Nanosized-Dependent Composition, Defects, and Spin Canting,” *J. Phys. Chem. C*, vol. 118, no. 7, pp. 3795–3810, Feb. 2014, doi: 10.1021/jp411481p.
[85] I. Nurdin, M. R. Johan, I. I. Yaacob, and B. C. Ang, “Effect of Nitric Acid Concentrations on Synthesis and Stability of Maghemite Nanoparticles Suspension,” *Sci. World J.*, vol. 2014, pp. 1–6, 2014, doi: 10.1155/2014/589479.
[86] A. Szpak *et al.*, “T1–T2 Dual-modal MRI contrast agents based on superparamagnetic iron oxide nanoparticles with surface attached gadolinium complexes,” *J. Nanoparticle Res.*, vol. 16, no. 11, p. 2678, Nov. 2014, doi: 10.1007/s11051-014-2678-6.
[87] A. Szpak, G. Kania, T. Skórka, W. Tokarz, S. Zapotoczny, and M. Nowakowska, “Stable aqueous dispersion of superparamagnetic iron oxide nanoparticles protected by charged chitosan derivatives,” *J. Nanoparticle Res.*, vol. 15, no. 1, p. 1372, Jan. 2013, doi: 10.1007/s11051-012-1372-9.
[88] A. Sudame, G. Kandasamy, and D. Maity, “Single and Dual Surfactants Coated Hydrophilic Superparamagnetic Iron Oxide Nanoparticles for Magnetic Fluid Hyperthermia Applications,” *J. Nanosci. Nanotechnol.*, vol. 19, no. 7, pp. 3991–3999, Jul. 2019, doi: 10.1166/jnn.2019.16326.
[89] M. Di Marco, M. Port, P. Couvreur, C. Dubernet, P. Ballirano, and C. Sadun, “Structural Characterization of Ultrasmall Superparamagnetic Iron Oxide (USPIO) Particles in Aqueous Suspension by Energy Dispersive X-ray Diffraction (EDXD),” *J. Am. Chem. Soc.*, vol. 128, no. 31, pp. 10054–10059, Aug. 2006, doi: 10.1021/ja061674y.
[90] I. Ostolska and M. Wiśniewska, “Application of the zeta potential measurements to explanation of colloidal Cr2O3 stability mechanism in the presence of the ionic polyamino acids,” *Colloid Polym. Sci.*, vol. 292, no. 10, pp. 2453–2464, Oct. 2014, doi: 10.1007/s00396-014-3276-y.
[91] J. J. Carlson and S. K. Kawatra, “Factors Affecting Zeta Potential of Iron Oxides,” *Miner. Process. Extr. Metall. Rev.*, vol. 34, no. 5, pp. 269–303, Aug. 2013, doi: 10.1080/08827508.2011.604697.
[92] S. Honary and F. Zahir, “Effect of Zeta Potential on the Properties of Nano-Drug Delivery Systems - A Review (Part 1),” *Trop. J. Pharm. Res.*, vol. 12, no. 2, pp. 255–264, May 2013, doi: 10.4314/tjpr.v12i2.19.
[93] G. da Silva *et al.*, “Studies of the Colloidal Properties of Superparamagnetic Iron Oxide Nanoparticles Functionalized with Platinum Complexes in Aqueous and PBS Buffer Media,” *J. Braz. Chem. Soc.*, 2016, doi: 10.21577/0103-5053.20160221.
[94] J. Stetefeld, S. A. McKenna, and T. R. Patel, “Dynamic light scattering: a practical guide and applications in biomedical sciences,” *Biophys. Rev.*, vol. 8, no. 4, pp. 409–427, Dec. 2016, doi: 10.1007/s12551-016-0218-6.
[95] N. Panagiotopoulos *et al.*, “Magnetic particle imaging: current developments and future directions,” *Int. J. Nanomedicine*, p. 3097, Apr. 2015, doi: 10.2147/IJN.S70488.
[96] O. Karaagac, H. Kockar, S. Beyaz, and T. Tanrisever, “A Simple Way to Synthesize Superparamagnetic Iron Oxide Nanoparticles in Air Atmosphere: Iron Ion Concentration Effect,” *IEEE Trans. Magn.*, vol. 46, no. 12, pp. 3978–3983, Dec. 2010, doi: 10.1109/TMAG.2010.2076824.
[97] L. Gholami, R. Kazemi Oskuee, M. Tafaghodi, A. Ramezani Farkhani, and M. Darroudi, “Green facile synthesis of low-toxic superparamagnetic iron oxide nanoparticles (SPIONs) and their cytotoxicity effects toward Neuro2A and HUVEC cell lines,” *Ceram. Int.*, vol. 44, no. 8, pp. 9263–9268, Jun. 2018, doi: 10.1016/j.ceramint.2018.02.137.

[98] M. Barrow *et al.*, “Co-precipitation of DEAE-dextran coated SPIONs: how synthesis conditions affect particle properties, stem cell labelling and MR contrast,” *Contrast Media Mol. Imaging*, vol. 11, no. 5, pp. 362–370, 2016.
[99] R. Stein *et al.*, “Synthesis and Characterization of Citrate-Stabilized Gold-Coated Superparamagnetic Iron Oxide Nanoparticles for Biomedical Applications,” *Molecules*, vol. 25, no. 19, p. 4425, Sep. 2020, doi: 10.3390/molecules25194425.
[100] G. F. Goya, T. S. Berquó, F. C. Fonseca, and M. P. Morales, “Static and dynamic magnetic properties of spherical magnetite nanoparticles,” *J. Appl. Phys.*, vol. 94, no. 5, pp. 3520–3528, Sep. 2003, doi: 10.1063/1.1599959.
[101] M. A. Gonzalez-Fernandez *et al.*, “Magnetic nanoparticles for power absorption: Optimizing size, shape and magnetic properties,” *J. Solid State Chem.*, vol. 182, no. 10, pp. 2779–2784, Oct. 2009, doi: 10.1016/j.jssc.2009.07.047.
[102] R. D. Piazza *et al.*, “PEGlatyon-SPION surface functionalization with folic acid for magnetic hyperthermia applications,” *Mater. Res. Express*, vol. 7, no. 1, p. 015078, Jan. 2020, doi: 10.1088/2053-1591/ab6700.